Development and Validation of a Computational Approach to Predicting the Synthesis of Inorganic Materials

by

Daniil A. Kitchaev

B.S., Chemical Engineering, California Institute of Technology (2012)
B.S., Computer Science, California Institute of Technology (2012)

Submitted to the Department of Materials Science and Engineering
in partial fulfillment of the requirements for the degree of

Doctor of Philosophy in Materials Science and Engineering

at the

MASSACHUSETTS INSTITUTE OF TECHNOLOGY

February 2018

Author . . . .
Department of Materials Science and Engineering
December 5, 2017

Certified by . . . .
Gerbrand Ceder
Visiting Professor of Materials Science and Engineering
Thesis Supervisor

Accepted by . . . .
Donald R. Sadoway
Chairman, Departmental Committee on Graduate Students

Development and Validation of a Computational Approach to Predicting the Synthesis of Inorganic Materials

by

Daniil A. Kitchaev

Submitted to the Department of Materials Science and Engineering
on December 5, 2017, in partial fulfillment of the
requirements for the degree of
Doctor of Philosophy in Materials Science and Engineering

Abstract

The concept of computational materials design envisions the identification of chemistries and structures with desirable properties through first–principles calculations, and the downselection of these candidates to those experimentally accessible using available synthesis methods. While first–principles property screening has become routine, the present lack of a robust method for the identification of synthetically accessible materials is an obstacle to true materials design. In this thesis, I develop a general approach for evaluating synthesizeability, and where possible, identifying synthesis routes towards the realization of target materials. This approach is based on a quasi–thermodynamic analysis of synthesis methods, relying on the assumption that phase selection is guided by transient thermodynamic stability under the conditions relevant to phase formation. By selecting the thermodynamic handles relevant to a growth procedure and evaluating the evolution of thermodynamic boundary conditions throughout the reaction, I identify potential metastable end–products as the set of ground state phases stabilized at various stages of the synthesis. To validate this approach, I derive the quasi–thermodynamic influence of adsorption–controlled finite–size stability and bulk off–stoichiometry on phase selection in the aqueous synthesis of polymorphic FeS_2 and MnO_2 systems, rationalizing the results of a range of synthesis experiments. To enable this analysis, I develop and benchmark the methodology necessary for the reliable first–principles evaluation of structure–sensitive bulk and interfacial stability in aqueous media. Finally, I describe a manganese oxide oxygen evolution catalyst, whose high activity is controlled by metastable, tetrahedrally–coordinated Mn^{3+} ions as an example of materials functionality enabled by structural metastability. The framework for the first–principles analysis of synthesis proposed and validated in this thesis lays the groundwork for the development of computational synthesis prediction and holds the potential to greatly accelerate the design and realization of new functional materials.

Thesis Supervisor: Gerbrand Ceder
Title: Visiting Professor of Materials Science and Engineering

Acknowledgments

I thank my parents, Natalia Dmitrieva and Andrei Kichaev, for teaching me how to be a functional, thought-filled human, and my family – Pavel Dmitriev, Renata Dmitrieva, Galina Kichaeva, Fljura Timasheva, and Igor Dmitriev – for helping them in this endeavour.

I am grateful to my graduate advisor, Gerbrand Ceder, as well as my undergraduate scientific advisor, Sossina Haile, for the countless hours they have dedicated to mentoring me, despite busy schedules, teleconferencing connection issues, and scientific frustrations.

I thank Stephen Dacek, William Richards and Aziz Abdellahi for teaching me how to be a theorist through our numerous office discussions and debates, and for guiding me through the vast array of computational tools necessary for this research.

This thesis would not have been possible without the insights, guidance, and data my collaborators and coauthors have shared with me. In particular, I thank Stephan Lany, Pieremanuele Canepa, John Perdew, Dane Morgan and Dan Nocera for their insights which were critical to much of the work in this thesis.

During my time in graduate school, I have had the pleasure of working on several projects outside of this thesis. I am grateful to Wenxuan Huang, Jinhyuk Lee, Riley Brandt, Rachel Kurchin, Julia Yang, Tina Chen, Zhengyan Lun, Raphaele Clement, Huiwen Ji and Alexander Urban for inviting me to work with them and exposing me to scientific topics I would not have encountered otherwise.

Finally, I thank Joanna Robaszewski for supporting me during my time in graduate school, at home and otherwise, tolerating the odd work hours and the frequent stress that were an unfortunate component of preparing this thesis.

Contents

List of Figures

List of Tables

Chapter 1

Introduction

In this chapter, I review the concept of first–principles computational materials design and identify the problem of materials synthesis prediction as a critical obstacle to the practical and wide–spread realization of this vision. I begin by reviewing the general structure of density functional theory (DFT) as it is the dominant method for computing the thermochemical and electronic properties of inorganic materials. I then briefly discuss the now–established process of first–principles materials property computation, and motivate the development of a general scheme for evaluating materials synthesizeability. I conclude by proposing a quasi–thermodynamic approach to understanding synthesizeability based on the behavior of several well–known polymorphic systems. The implementation and validation of this scheme is the subject of chapters 2, 3, and 4 of this thesis.

1.1 Thermodynamics from first principles

The cornerstone of computational materials analysis from first–principles is density functional theory (DFT), which is a robust, scalable approach to evaluating the zero–temperature internal energy of many–electron systems at the level of quantum mechanics. On the basis of these ground state energies, computed for a range of specially designed model systems and perturbations, it is possible to approximate the complete free energy of a many–body system and its thermodynamic properties. Thus, the development of DFT, taken together with statistical mechanics, yields a practical model of first–principles materials thermodynamics, allowing for the predictive analysis of materials properties.

While the formulation of DFT is exact, its practical application involves numerous assumptions and approximations. Obtaining reliable energies from DFT calculations still relies on the careful construction of model systems and reference states which maximize the cancellation of systematic errors. The development and benchmarking of a number of these methods is the subject of chapter 2. In this section I present a brief overview of the formal structure of DFT, and review the common approximations introduced in its practical application. This overview is largely based on the excellent tutorials published by K. Capelle[1] and K. Burke[2].

The foundation of quantum mechanics is the postulate that all properties of a system are encoded in its wavefunction $\Psi(\mathbf{r})$, that is a solution to the Schrödinger equation

$$\left[\frac{-\hbar^2}{2m}\nabla^2 + v(\mathbf{r})\right]\Psi(\mathbf{r}) = E\Psi(\mathbf{r})$$

for some potential $v(\mathbf{r})$. While this equation is solvable for a single particle, it quickly becomes intractable for systems involving many interacting particles, such as any many–electron model of a solid material. One source of this intractability is that for a system of M particles, the wavefunction becomes a function of 3M coordinates, while the potential term becomes a sum of multi–particle interactions. For a Coulombic system, the Schrödinger Equation becomes

$$\left[\left(\sum_i^N \frac{-\hbar^2}{2m}\nabla_i^2 + v(\mathbf{r})\right) + \sum_{i<j}\frac{q^2}{|\mathbf{r_i} - \mathbf{r_j}|}\right]\Psi(\mathbf{r_1}, \mathbf{r_2}, ..., \mathbf{r_N}) = E\Psi(\mathbf{r_1}, \mathbf{r_2}, ..., \mathbf{r_N}).$$

where the potential $v(\mathbf{r})$ is in turn generated by a number of nuclei at positions $\mathbf{R_k}$

with charge Q_k

$$\sum_i v(\mathbf{r}) = \sum_{i,k} \frac{Q_k q}{|\mathbf{r_i} - \mathbf{R_k}|}$$

Typically, one would approach this problem by diagonalizing the Hamiltonian, solving for a wavefunction in an appropriate basis, and then calculating observables. While this approach can be applied to the many–body problem, for exact or even approximate algorithms, the computational cost of such direct calculation is too high for general use. Nonetheless, direct solutions of relatively small many–body systems through coupled–cluster, configuration–interaction, and quantum monte carlo methods provide valuable benchmarking data for validating more approximate solutions.

A significant simplification of this problem is afforded by the Hohenberg-Kohn theorems[3], which state that all information pertaining to the ground–state of a system encoded in $\Psi(\mathbf{r_1}, \mathbf{r_2}, ..., \mathbf{r_N})$ can be exactly obtained from a simpler functional of only the electron density $n(\mathbf{r})$. Specifically, the Hohenberg-Kohn theorems reveal that a ground state electron density $n_0(\mathbf{r})$ corresponds uniquely to a ground state wavefunction $\Psi_0(\mathbf{r_1}, \mathbf{r_2}, ..., \mathbf{r_N})$ and at most one potential $v(\mathbf{r})$. Consequently, all ground state observables can also be calculated from the ground state electron density. Conveniently, the variational principle also holds for this electron density formulation

$$E[n_0(\mathbf{r})] \leq E[n'(\mathbf{r})]$$

where E_0 is the ground state energy corresponding to a ground state density n_0, and $E[n']$ is the energy of some other electron density. Thus, we can proceed from a trial electron density to a wavefunction to a potential, which we can use to create a new electron density, iterating until we achieve self-consistency and a minimum in energy:

$$n^{(1)}(\mathbf{r}) \rightarrow \Psi^{(1)}(\mathbf{r_1}, \mathbf{r_2}, ..., \mathbf{r_N}) \rightarrow v^{(1)}(\mathbf{r}) \rightarrow n^{(2)}(\mathbf{r}) \rightarrow ...$$

The density functional $E[n] = T[n] + U[n] + V[n]$, where $T[n]$ is the kinetic energy, $U[n]$ is the electronic interaction energy, and $V[n]$ is the potential, is typically solved using the Kohn–Sham approach[4]. We split the non–homogeneous, multiple–interacting–body problem into two simpler problems: one that is non–homogeneous, but also non–interacting, and one that is homogeneous, but interacting. Correspondingly, we split the total energy into non–interacting and interacting terms. The non–interacting terms are a sum of single–particle orbitals, while the interacting terms are captured by more complex exchange–correlation functionals. Mathematically, we split the kinetic energy $T[n]$ into a sum of non-interacting "single-particle" kinetic energies $T_s[n]$ and a remainder $T_c[n]$. Given a set of single particle orbital basis functions $\phi_i(\mathbf{r})$ that yield a density n,

$$T_s[n] = \frac{-\hbar^2}{2m} \sum_i^N \int d^3r \phi_i^*(\mathbf{r}) \nabla^2 \phi_i(\mathbf{r}) = T_s[\{\phi_i[n]\}]$$

Similarly, we split the interaction energy into an electrostatic Hartree term (purely electrostatic energy of a charge density $n(\mathbf{r})$):

$$U_H[n] = \frac{q^2}{2} \int d^3r \int d^3r' \frac{n(\mathbf{r})n(\mathbf{r}')}{|\mathbf{r} - \mathbf{r}'|}$$

and a remainder $U_{xc}[n]$, which we group with $T_c[n]$ into a term called the *exchange-correlation energy* $E_{xc}[n]$:

$$\begin{aligned} E[n] &= T[n] + U[n] + V[n] \\ &= T_s[\{\phi_i[n]\}] + U_H[n] + (T[n] - T_s[n] + U[n] - U_H[n]) + V[n] \\ &= T_s[\{\phi_i[n]\}] + U_H[n] + E_{xc}[n] + V[n] \end{aligned}$$

The exchange correlation energy E_{xc} captures the energy associated with *electron exchange* E_x and *electron correlation* E_c. Exchange energy originates from the fermionic repulsion between electrons, constraining the electronic wavefunction to be antisymmetric with respect to electron exchange. While this energy can be written explicitly in terms of orbitals ("Fock term" in the classical Hartree–Fock formulation), there is no known way to write this term directly in terms of electron density. Correlation energy arises from the error associated with the fact that looking at electron density inherently considers only spatial averages and ignores the fact that individual electrons do interact with each other and are thus correlated.

Up to this point, DFT has been an exact reformulation of the Schrödinger equation, and is generally no easier to solve than the direct minimization of the energy functional. The key element of DFT calculations is the observation that in practice, $E_{xc}[n]$ is small compared to $T_s[n]$ and $U_H[n]$, and many relatively simple approximations can be used to compute it to acceptable accuracy. Assuming that we can approximate $E_{xc}[n]$ with something not too complicated, we can solve the remaining system using the Kohn–Sham equation, which rewrites the multi-body problem discussed earlier as a system of non–interacting single–orbital problems with an effective potential. Briefly summarizing the derivation, the minimization of the energy functional requires that:

$$\frac{\delta E[n]}{\delta n(\mathbf{r})} = \frac{\delta}{\delta n(\mathbf{r})}(T_s[n] + V[n] + U_H[n] + E_{xc}[n]) = \frac{\delta T_s[n]}{\delta n(\mathbf{r})} + v(\mathbf{r}) + v_H(\mathbf{r}) + v_{xc}(\mathbf{r}) = 0$$

Thus, we choose an effective potential $v_s(\mathbf{r}) = v(\mathbf{r}) + v_H(\mathbf{r}) + v_{xc}(\mathbf{r})$, such that the energy is now only a function of a single–particle kinetic energy and a potential v_s. Thus, we can solve the single-body Schrödinger Equation:

$$[\frac{-\hbar^2}{2m}\nabla^2 + v_s(\mathbf{r})]\phi_i(\mathbf{r}) = E_i\phi_i$$

Given the complex nature of $v_s(\mathbf{r})$, this equation is non–linear and must be solved iteratively, where each iteration involves calculating the electron density corresponding to the current solution, and obtaining a new potential until self–consistency is obtained. The resulting solutions yield the total energy of the system, as well as the electron density. The eigenvalues E_i of the Kohn–Sham system are not generally meaningful, with the exception of the eigenvalues corresponding to the highest occupied energy level and the lowest unoccupied energy level, as they correspond exactly to the ionization energy and electron affinity of the system.

Two important details in Kohn–Sham DFT calculations are (1) the choice of basis functions ϕ_i and (2) the use of pseudopotentials. Basis functions vary from plane waves to more physical combinations of orbitals; in particular, the Vienna Ab-initio Simulation Package (VASP)[5, 6] used throughout this thesis relies on a plane-wave basis set. Pseudopotentials are precomputed modifications to the $v(\mathbf{r})$ component of the $v_s(\mathbf{r})$ Kohn–Sham potential that encapsulate the behavior of nuclear electrons, such that the full Kohn–Sham equation is only solved for the valence electrons, which are both more relevant, and tend to have a smoother wavefunction, reducing the number of basis vectors needed for convergence. Common pseudopotentials are the Vanderbilt pseudopotentials [7], and a more general form of pseudopotentials with plane waves called the Projector Augmented Wave (PAW) method [8]. A significant advantage of the PAW method is that unlike pseudopotentials, which lose all wavefunction information near the nuclei except the energy landscape, PAW calculations construct atom–like wavefunctions near the nuclei, and envelope functions beyond a certain radius, preserving nuclear wavefunction information.

The remaining difficulty in the Kohn–Sham scheme is the approximation to the exchange correlation energy E_{xc}. A number of functionals exist to approximate this energy, which can be derived from first principles, semi-empirical considerations, or fits to experimental data. Typically, each functional has a limited scope of chemical reactions for which it can yield reliable energies, and understanding this scope for each functional is critical to the practical use of DFT for materials simulations.

The simplest exchange–correlation functional is the local density approximation (LDA), which is based on the homogeneous electron gas. For this gas, the exchange energy is known analytically and can be applied to a non–homogeneous system by substituting $n(\mathbf{r})$ for n, while the correlation energy has been tabulated from quantum monte carlo calculations. Thus, the total functional becomes

$$E_{xc}^{LDA}[n] = \int d^3r(e_x + e_c)^{homogeneous}|_{n \to n(\mathbf{r})}$$

where e_x and e_c are the analytical and tabulated expressions for the exchange and correlation energy of a homogeneous electron liquid, respectively [1]. Despite this very rough approximation, E_{xc}^{LDA} achieves surprisingly good results due to a systemic cancellation of error between the exchange and correlation parts of the energy – LDA underestimates the correlation energy, but overestimates the exchange energy in a systemic way.

The Generalized Gradient Approximation (GGA) improves on LDA by taking into account the gradient of the electron density:

$$E_{xc}^{GGA}[n] = \int d^3r f(n(\mathbf{r}), \nabla n(\mathbf{r}))$$

where the functional f can be chosen by satifying various limiting behaviors, or through empirical fitting. The most common GGA variants are the PBE (Perdew, Burke, Ernzerhof)[9] and LYP (Lee, Yang, Parr)[10] functionals. Both GGA variants significantly improve upon LDA in the representation of covalent, ionic, metallic, and hydrogen–bonded system, although further corrections are necessary to account for medium and long–range van-der-Waals forces. The two main sources of error in a GGA are self–interaction and a necessary compromise between reproducing the limiting behavior of homogeneous electronic systems and that of sharp gradients, corresponding to surfaces. Self–interaction arises from the fact that in a density representation, an electron is able to interact with itself, which destabilizes occupied states and reduces oxidation potentials and band gaps. Removal of self–interaction however is difficult and is currently achieved only with the use of empirical corrections. One such correction is the Hubbard U model, which penalizes partially occupied states and thus counteracts the extra electronic repulsion from self–interaction. An alternative method is the use of "hybrid functionals", which introduce a contribution of the exact–exchange Fock term into the Hamiltonian. Empirically, both methods can alleviate errors in oxidation potential and band gap, which are the most obvious consequences of self–interaction, but at the cost of significant computational expense, and larger errors in other material properties.

The issue of simultaneously reproducing the features of homogeneous densities and electronic surfaces can be resolved in a more first–principles fashion by introducing the kinetic energy of the system $\nabla^2 n(\mathbf{r})$ into the functional to form a meta-GGA. These functionals can satisfy all known constraints on an exchange–correlation functional and thus accurately reproduce the characteristics of all types of bonding [11, 12]. I will address one such functional in detail in chapter 2 of this thesis.

1.2 Computational materials design and the problem of synthesis

With the development of reliable, first–principles models of materials with DFT, it has become possible to theorize a material with a particular crystal structure and composition and evaluate many of its chemical and physical properties, without requiring any new experimental data. Moreover, this analysis can be automated and repeated in a high–throughput fashion with minimal human interaction[13, 14, 15, 16]. This process is transformative for the design and optimization of materials for various functionalities, as time and resource–consuming laboratory testing can be limited to only those candidate materials which are likely to exhibit superior properties. Furthermore, systematic screening of poorly–explored chemical spaces can quickly and cheaply identify new materials which may be worth exploring experimentally, giving direction to the exploration of a generally combinatorially–large space of elemental compositions[15, 17, 18].

A significant obstacle to the full realization of this concept of computational materials design is the question of synthetic accessibility. To experimentally realize a theorized material with favorable properties, it must be synthesized in the lab, which is often the most difficult and restrictive step in materials development. Early work in computational materials screening circumvented this problem by only analyzing previously synthesized materials, searching for new high–performance materials among those tabulated in the Inorganic Crystal Structure Database (ICSD) [19] and other sources. The development of truly new materials from first principles has been restricted to materials computed to be thermodynamically stable, based on the assumption that thermodynamically stable materials are likely to be synthetically accessible by some process[17, 18, 20]. However, this approach suffers from two major drawbacks. First, it neglects the vast space of metastable materials, which make up approximately half of known materials based on those documented in the ICSD and computed within the Materials Project[14], as can be seen in Figure 1-1. Second, this approach does not give any insight into the processes that may be used to synthesize the target material. The resolution of these two challenges in a scalable, first–principles fashion is necessary for the practical implementation of computational design for the identification and development of new functional materials[18].

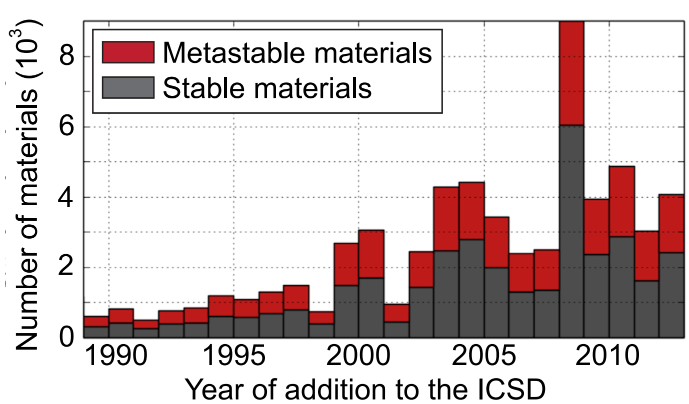

Figure 1-1: Fraction of stable and metastable materials in the Inorganic Crystal Structure Database (ICSD) [19], grouped by the year these materials were added to the database. Energies used here are taken from the Materials Project[14].

1.3 A quasi–thermodynamic approach to synthesis

The objective of this thesis is to identify and benchmark a computational scheme for the scalable prediction of synthesizeability and the identification of synthesis pathways for inorganic, ionic materials. The question of which materials are synthetically accessible, and how they may be synthesized is a broad problem that in the most general sense requires a case–by–case analysis for each synthesis technique, taking into account features of each chemical system, thermodynamic driving forces and kinetic pathways. Such an analysis is intractable at an atomistic scale, and would be difficult to automate for high–throughput materials design. Instead of a direct simulation approach, I describe a quasi–thermodynamic framework which can be used to eliminate materials unlikely to be synthesizeable, as well as identify the conditions under which synthesizeable materials would be likely to form. I will note that this question has been explored in parallel to myself by other authors, with similar conclusions to those I describe in this section[21, 22].

An initial insight into the origin of metastability can be obtained from known synthesis routes to common metastable materials. Some of the best known metastable materials are crystals formed geologically at high–pressure, such as diamond. These materials are thermodynamically stable under high–pressure and form deep in the Earth's crust where such high–pressure conditions are available. After the crystals grow to macroscopic sizes however, they can be extracted from these high–pressure conditions while retaining their structure, persisting as macroscopic metastable materials. Similar behavior can be seen in the formation of metastable nanocrystallites of TiO_2, ZrO_2 and other ceramics, where the combination of bulk and surface energies stabilizes a bulk–metastable phase in a nanocrystalline size–regime, promoting its formation preferentially to that of the bulk–stable phase[23, 24, 25]. These examples suggest a more general hypothesis, which may serve as an initial approach to the computational analysis of synthesis: phase formation occurs under conditions where the phase in question is instantaneously stable within the thermodynamic boundary conditions relevant to the synthesis environment.

An alternative approach to understanding synthesis is to analyze potential intermediate phases and transition states along a reaction pathway corresponding to the formation of a solid product. As the process evolves along its reaction coordinate, we can expect the system to choose locally low–energy configurations so as to avoid high kinetic barriers and highly unstable states. Thus, within some measure of configurational locality, the system minimizes its free energy, achieving a local equilibrium. The evolution of this local equilibrium along the reaction coordinate yields the same principle of quasi–thermodynamic stability: the formation of a product phase requires that this phase be related to an instantaneous equilibrium state at some point during the synthesis reaction.

This quasi–thermodynamic formulation of synthetic accessibility implies that at a minimum, a synthetically accessible phase must be stable under some conditions which can be expected during a synthesis reaction. Mathematically, there must exist a set of thermodynamic boundary conditions, and thus a thermodynamic potential, for which the target phase is a ground state. For example, high–pressure metastable materials are ground states of the Gibbs free energy $G(T, P)$, at high pressure. Nanoscale–stabilized phases such as TiO_2 anatase are ground states of a thermodynamic potential ψ which accounts for surface energy, constrained to small particle size: $\psi(P, T, A) = g_b V + \gamma A$, where g_b is the volumetric Gibbs free energy, P is pressure, T is temperature, V is the particle volume, γ is surface energy, and A is particle surface area[23, 24]. Thus, to identify synthesizable materials, it is necessary to search for the ground states of thermodynamic potentials across possible boundary conditions.

The correspondence between the evolving quasi–thermodynamic boundary conditions and the features of a real synthetic process relates the transient conditions necessary to form a target phase to practical choices in synthesis design. While high–pressure stabilization is a relatively straightforward thermodynamic handle to implement, it is much more difficult to, for example, constrain particle size for finite size stabilization. Instead, nano–scale stabilization may be controllable by engineering nucleation and growth–rates, which are strongly dependent on supersaturation, temperature, the presence of heterogeneous nucleation centers. Some thermodynamic handles may simply be too difficult to control with the precision necessary to target a desired phase, in which case a phase predicted to be synthesizeable would not be accessible in practice. Thus, clearly identifying the relationship between synthetic processes and thermodynamic handles, is critical to the practical implementation of quasi–thermodynamic synthesis planning.

1.4 Thesis summary

In this thesis, I evaluate the ability of the quasi–thermodynamic framework described in section 1.3 to rationalize synthesis outcomes in several polymorphic systems, and provide an example of unique materials behavior enabled by metastability. In chapter 2, I develop and benchmark a number of computational methodologies well–suited to simultaneously capture the fine energetics of structure–selection, and the larger scale energetics of formation reactions. In chapters 3 and 4, I rationalize phase selection in the aqueous growth of FeS_2 and MnO_2 polymorphic systems through finite–size stabilization and off-stoichiometry, explaining how the choice of synthesis medium drives the formation of an array of metastable products. Finally, in chapter 5, I present a new manganese oxide oxygen evolution catalyst as an example of unique materials functionality enabled by metastability. Throughout this thesis, I demonstrate the ability of the quasi–thermodynamic framework described here to reproduce synthesis results, identifying conditions necessary to synthesize metastable products in close agreement with experiment. These results lend significant support to the predictive power of the analysis presented here, and motivate further development of this theory, as well as its application to the realization of new materials.

Chapter 2

First-principles methods for structure-sensitive thermodynamics

A key prerequisite to the first–principles analysis of structure selection during synthesis is a reliable method for computing the relative energies of structures and identifying ground–state phases. In the first half of this chapter I identify the new Strongly Constrained and Appropriately Normed (SCAN) [11] meta-GGA exchange–correlation functional for DFT as uniquely well suited for evaluating ground state selection among chemically similar structures. I demonstrate the superior performance of this functional with the particular example of MnO_2 polymorphs, as well as with broad statistics across polymorphs of ionic binary compounds. However, as synthesis involves the formation of a product from precursors which generally significantly differ in composition, it is also necessary that we have a method which yields reliable results for total formation energies, including redox reactions. While SCAN improves upon previous non–empirical methods in reproducing total formation energies, alone it is insufficient to predict synthesis conditions. In the second half of this chapter, I develop and benchmark a thermodynamic referencing scheme for SCAN which reduces the error in total formation energy to a level appropriate for analyzing materials synthesis.

The content of this chapter is based, often verbatim, on three manuscripts which are published or in preparation for publication:

- D. A. Kitchaev, H. Peng, Y. Liu, J. Sun, J. P. Perdew, G. Ceder. "The energetics of MnO_2 polymorphs in density functional theory." *Phys. Rev. B*, 93, 045132 (2016)

- Y. Zhang†, D. A. Kitchaev†, J. Yang, T. Chen, S. T. Dacek, R. Sarmiento-Perez, M. A. L. Marques, H. Peng, G. Ceder, J. P. Perdew, J. Sun. "Efficient first-principles prediction of solid stability: Towards chemical accuracy." [submitted] (2017) (†equal contribution)

- D. A. Kitchaev, G. Ceder. "Eliminating oxidation potential error in semi–local density functional theory through thermodynamic referencing." [in preparation] (2017)

2.1 Features of exchange-correlation functionals

First-principles thermodynamics has over the last decades matured into a reliable method for accessing the energetics of phase transitions and reactions in condensed matter systems. At the heart of this method lies Kohn-Sham density functional theory (DFT)[4], with its standard approximations to the exchange-correlation energy providing a reasonably accurate picture of electronic structure. One of the most basic results that can be derived from a set of DFT calculations is the ground-state structure of a given compound under some set of conditions, usually set as zero temperature and pressure. However, despite the importance of accurate first-principles structure determination for both materials and property analysis[26, 27, 28, 29] this determination is often extremely difficult as the total energy differences between competing phases can be on the order of only a few meV per formula unit[30]. As a result, ground state structure selection is an attractive benchmark for verifying the adequacy of the physical model underlying a given approximation to the exchange-correlation energy.

A common feature of exchange-correlation functionals is the selective improvement of a target property at the expense of errors elsewhere. To study the accuracy of common DFT methods for structure selection and other key properties in comparison to SCAN[11], we consider the GGAs PBE[9] and PBEsol[31], the Hubbard-U-corrected PBE+U and PBEsol+U[32, 33], and the hybrid of PBE with exact exchange HSE06[34, 35] functionals. This set of functionals provides a representative sample of common approaches to improving the accuracy of DFT. PBE is the base workhorse non-empirical functional most commonly used in the literature[36]. While PBE provides reasonably accurate results for total energies across a wide range of chemistries, it suffers from significant electronic structure errors arising from self-interaction, as well as a tendency to disfavor density overlap between atoms (making lattice constants too long, especially in van der Waals bonded systems), originating from a compromise in the representation of the exchange energy of solids and molecules[9, 37, 38]. A common solution to the self-interaction problem is the empirically-fitted Hubbard U correction in PBE+U and PBEsol+U[33, 38]. The downsides of the +U approach are that it usually requires fitting to experimental data, and that it gives rise to errors in orbital hybridization, leading to further reduction of density overlap between atoms and errors in magnetism[39]. The density overlap problem in PBE can be resolved by restoring the second-order gradient coefficient for exchange, as is done in the PBEsol functional[31]. PBEsol improves the general energetic representation of solids and surfaces, but typically underestimates lattice parameters and overly stabilizes molecules[40] and solids with respect to atomization. Finally, hybrid functionals such as HSE06 attempt to improve upon the performance of PBE by introducing a fraction of exact exchange into the calculation[34, 35], which cancels some of the self-interaction error, at the cost of a significant increase in computational expense. In contrast, SCAN[11], and other meta-GGAs[41, 42, 43, 44, 11] attempt to correct the errors of PBE by introducing the orbital kinetic energy density into the functional, which allows for the simultaneous representation of extended systems and molecules, and enables SCAN to appropriately treat different chemical bonds (e.g., covalent, metallic, and even weak bonds), which no LDA or GGA can[45]. Since the design of SCAN is targeted to satisfy all fundamental constraints simultaneously, rather than correcting specific drawbacks of PBE, we expect that SCAN would yield an overall improvement in the representation of all system properties relative to PBE, rather than the trade-offs in accuracy typical of other functionals.

2.2 MnO_2 polymorphs as a benchmark system

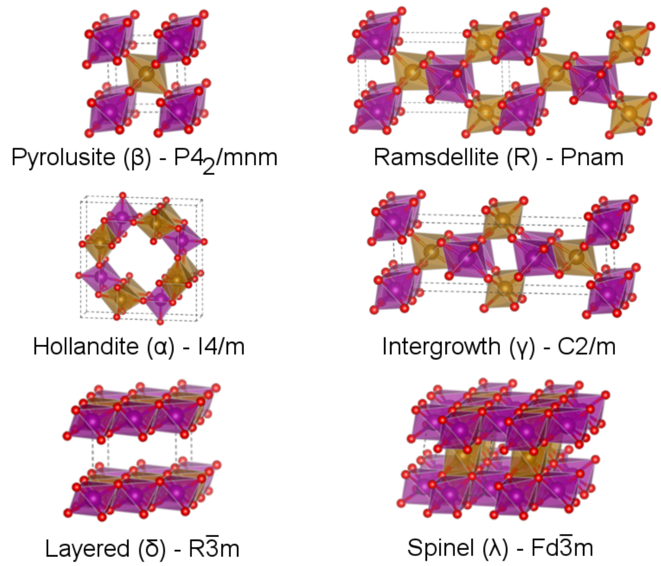

Figure 2-1: The polymorphs of MnO_2 with well-defined crystalline phases. The purple and yellow atoms represent spin-up and spin-down Mn respectively, while the red atoms represent O. The magnetic orderings shown correspond to the lowest-energy configurations within PBE, PBEsol, and SCAN. Note that the space group corresponds to structural symmetry, neglecting reductions of symmetry from the magnetic ordering.

One particularly interesting system for investigating structure-transition energetics within DFT is the set of manganese oxides. The Mn-O system contains a diverse set of relatively well- characterized structures both across a range of stoichiometries (MnO, Mn_3O_4, Mn_2O_3, and MnO_2), and within a single stoichiometry (pyrolusite β, ramsdellite R, hollandite α, intergrowth γ, spinel λ, layered δ MnO_2), as shown in Figure 2-1. All the MnO_2 polymorphs share a common basic atomic structure - small Mn^{4+} ions in a spin-polarized $3d^3$ configuration and large, highly polarizable O^{2-} ions in a spin-unpolarized $2p^6$ configuration, arranged in corner- and edge- sharing MnO_6 octahedra. The different packings of these octahedra form a variety of polymorphic structures, many of which have been studied extensively for applications in energy storage, catalysis, pigmentation, etc[46, 47, 48, 49, 50, 51, 52, 53, 54].

The relative stability of the various oxidation states of Mn-O has been previously investigated within the Perdew-Burke-Erzenhof (PBE) and PBE+U forms of GGA-DFT, as well as with the exact-exchange-corrected hybrid PBE0 and Heyd-Scuseria-Erzenhof (HSE) functionals[55]. However, the energetics and properties of the polymorphic phases of MnO_2 remain unresolved in first-principles calculations[56, 57, 58]. Experimentally, it is established that pyrolusite β-MnO_2 is the ground state of pure MnO_2[48], but to our knowledge no non-empirical DFT method has stabilized β-MnO_2 as the ground state of the system. In this section, we resolve this problem with the use of the recently reported SCAN meta-GGA[11] and show that the resolution of the ground state structure problem in the MnO_2 system also leads to a much more accurate representation of the basic physics of the material.

2.3 Computational methods

All calculations are done within the Vienna Ab-Initio Simulation Package (VASP)[5, 6], using a Γ-centered k-point grid with a reciprocal space discretization of 0.25 Å^{-1}. For both PBE+U and PBEsol+U, we rely on the Dudarev effective-U formulation[33], applying a U=3.9 eV to the $3d$ states of each Mn atom, based on previous optimizations for the formation energy, redox potential, and agreement with higher-order functionals[55, 59]. To obtain the total energy of each phase we choose the supercells given in Table 2.1, in all cases initializing the calculation based on experimentally reported geometries and relaxing the structures self-consistently within each functional. As all MnO_2 phases are known to be well-represented energetically by antiferromagnetic (AFM) orderings[55, 60, 58, 61, 62, 63, 64, 65], we ensure that the chosen supercells were compatible with all likely AFM orderings. To obtain the magnetic structure of each phase, we enumerate up to 12 of the most likely configurations, chosen as the orderings with a net zero magnetic moment and highest symmetry. The magnetic structures used for HSE calculations and all analysis across all functionals are given in Figure 2-1 and are the ground state magnetic orderings for PBE, PBEsol, and SCAN, but not PBE+U or PBEsol+U, which we will address in a later section. Subsequent band structure and DOS calculations were set up using the scheme proposed by Setyawan and Curtarolo [66, 67], based on the self-consistently relaxed, symmetry-reduced primitive cells derived from the AFM orderings described above.

2.4 Functional accuracy in the MnO_2 system

Phase	**Lattice Parameters** (a, b, c) (Å)	**Volume** (Å^3/f.u.)	$\mathbf{\Delta H_f}$ (meV/f.u.)	$\mathbf{E_{gap}}$ (eV)
β	4.39(1), 4.39(1), 2.871(4)	27.8(1)	0	0.27
R	9.29(3), 4.49(4), 2.857(8)	29.8(5)	56(32)	
α	9.80(2), 9.80(2), 2.85(1)	34.2(2)	>0	
γ	13.7(1), 2.86(1), 4.46(1)	29.2(3)	>0	
λ	5.67(1), 5.67(1), 5.67(1)	32.3(1)	>0	
δ	5.69(1), 5.69(1), 7(3)†		>0	2.1‡

Table 2.1: Experimental parameters for the polymorphs of MnO_2, given for the supercells used for total energy calculations. Uncertainty, given in parenthesis, is determined as the standard deviation between experimental results (β, R, α), or assumed uncertainty from diffraction refinement (γ, λ, δ). The formation enthalpy is given with respect to β-MnO_2. † The c lattice constant (interlayer spacing) in δ-MnO_2 is highly uncertain as all reported samples of this phase have some amount of intercalated cations or water. ‡ The band gap for δ-MnO_2 measured by Pinaud *et al.* is for birnessite-type δ-MnO_2, but explicitly noting the absence of mid-gap Mn^{3+} states[68], suggesting it should be similar to that of pure δ-MnO_2. Ref: β[48, 51, 69, 70, 71, 19, 72, 73, 74], R[48, 75, 76, 77, 51, 19], α[48, 78, 51, 19], γ[49], λ [50], δ[79, 80, 68]

The formation energies of the various MnO_2 phases with respect to the experimental ground state, β-MnO_2, are given in Figure 2-2. While the experimental formation enthalpies of most phases are not known, they must be positive in order for β to be the ground state phase. It is clear that only PBEsol and SCAN even qualitatively reproduce this result, and only SCAN is able to quantitatively reproduce the experimentally known formation enthalpy of R-MnO_2. The fact that only PBEsol and SCAN give qualitative agreement with experiment in terms of picking the correct ground state phase could be expected from the fact that SCAN and PBEsol are the only functionals that yield reasonably accurate descriptions of non-covalent electronic density overlaps, which are critically important for distinguishing between the various packings of MnO_6 octahedra that form the diverse polymorphs of MnO_2. However, due to its ability to recognize not only weak electron density overlap but also strong chemical bonds[81], SCAN significantly improves on the successes of PBEsol, giving an altogether more accurate picture of the physics of the MnO_2 system, leading to the remarkable quantitative agreement between experiment and SCAN ($\Delta H_f^{\beta \to R}$ = 54.2 meV/MnO_2 from SCAN versus 56 ± 32 meV/MnO_2 experimentally[48]).

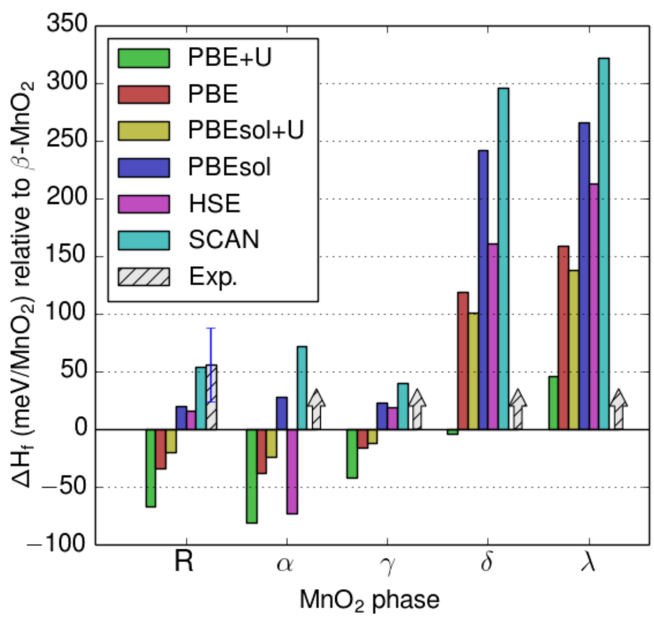

Figure 2-2: Formation energies of MnO_2 polymorphs with respect to the experimental ground state, β-MnO_2. Only PBEsol and SCAN stabilize β-MnO_2 as the ground state phase, and only SCAN quantitatively agrees with the experimental transition enthalpy from β-MnO_2 to R-MnO_2. Note that the experimental 'arrows' drawn for the α, γ, δ, and λ phases indicate that experimentally the formation energy of these phases is some unknown positive quantity.

In terms of electronic structure, all phases of MnO_2 are semiconducting. However, as can be seen in Figure 2-3, both PBE and PBEsol predict β-MnO_2 to be a metal due to the self-interaction error present in both functionals[82], and the resulting reduction of the calculated band gap. The empirical Hubbard U correction opens up a small band gap close to the experimental value (PBE+U: 0.20 eV, PBEsol+U: 0.28 eV, Exp: 0.27 eV[73, 74]), which could be expected as, by construction, the Hubbard U leads to the localization of carriers, flattening of d-bands, and opening of band gaps[33]. HSE in turn converges to a much larger band gap (1.7 eV), while SCAN gives a gap (0.43 eV) that is close to the +U and experimental results. The results are similar for the δ phase where the experimental band gap is also known: PBE and PBEsol underestimate the bandgap (1.1 eV and 0.96 eV respectively, versus 2.1 eV experimental [68]) PBE+U, PBEsol+U, and SCAN give almost identical band gaps in good agreement with experiment (2.0 eV, 2.1 eV, and 2.0 eV respectively), and HSE overestimates the band gap (3.4 eV). It must be noted that the experimental band gaps in the MnO_2 system are not definitively established - the gaps reported here are based on the best estimates available in the literature. The fact remains however that SCAN significantly increases the band gap compared to PBE and PBEsol, which are known to underestimate band gaps, and agrees with values obtained from empirically-fitted PBE+U and PBEsol+U functionals, while keeping the gaps well below those of HSE. The improvement in band gap could originate from two sources. First, the SCAN meta-GGA, like the hybrid functionals, is implemented in a generalized Kohn-Sham scheme in which the exchange-correlation potential is not a multiplicative operator[11]. Second, the self-interaction error in SCAN is greatly reduced in the case of well–localized electrons as SCAN uses a functional form that is almost self-interaction free in the case of atomic-like densities, where the exchange-correlation hole remains near its reference electron[11]. As the valence band in β-MnO_2 consists of weakly-hybridized Mn t_{2g} and O p_z states, this condition may be approximately satisfied, leading to a cancellation of self-interaction in SCAN, and consequently an increased band-gap compared to PBE or PBEsol. We must note however that this result is somewhat atypical - we find that for many materials, including rutile TiO_2, SCAN corrects about half of the PBE underestimation of the experimental gap.

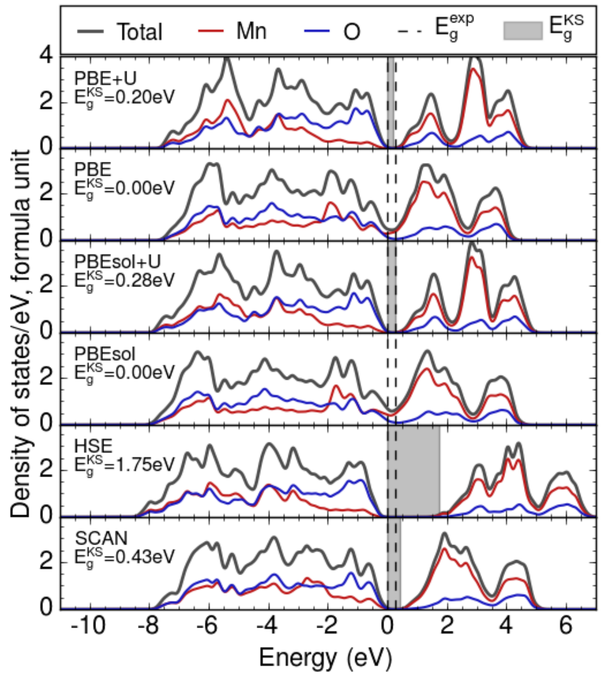

Figure 2-3: The total and atom-projected density of states of β-MnO_2. The shaded regions denote the band gap predicted by each functional, while the dotted line marks the experimental bandgap, 0.27 eV[73, 74]. The DFT bandgap is given by the generalized Kohn-Sham eigenvalues from a band structure calculation, while the DOS is calculated with a 0.1 eV smearing.

Another important property of the MnO_2 system is its magnetic configuration. Experimentally, β-MnO_2 adopts a helical magnetic configuration[83, 84, 85] while all other phases are believed to be antiferromagnetic (AFM)[62, 63, 64, 65]. In previous DFT work, the ferromagnetic (FM) form of β and α MnO_2 was found to be stable in PBE+U, in conflict with experiment [55, 61, 60]. We find that both PBE+U and PBEsol+U stabilize FM orderings with respect to the reference AFM configurations given in Figure 2-1, and overall favor alternate AFM configurations with clusters of nearest-neighbor aligned spins, contrary to what could be expected on the basis of oxygen-mediated superexchange governing the antiferromagnetism in MnO_2. In contrast to the +U functionals, PBE, PBEsol, and SCAN favor the AFM configuration in β, R, α and γ, and give essentially degenerate results for the AFM and FM configurations in δ and λ, likely due to the fact that the size of the true antiferromagnetic ground state unit cell in these phases includes up to 128 spins[63, 86] the enumeration

	PBE+U	PBE	PBEsol+U	PBEsol	HSE	SCAN
MRE	1.64%	0.64%	0.25%	-0.73%	-0.37%	-0.51%
MARE	1.64%	0.66%	0.53%	0.79%	0.62%	0.68%

Table 2.2: The lattice parameter mean (absolute) relative error (MRE, MARE) of the β, R, α, γ, and λ phases of MnO_2, as compared to the experimental values presented in Table 2.1. It is clear than SCAN performs better than the similarly efficient non-empirical PBE and PBEsol functionals, and is outperformed by only HSE and the empirically fitted PBEsol+U. Note that the δ phase is excluded due to highly uncertain experimental lattice constants, as discussed in the caption of Table 2.1.

of which is beyond the scope of this work.

A final measure of functional accuracy is its ability to reproduce lattice parameters, as they are often indicative of how well the functional captures the bonding character of the solid[87, 88]. The improved performance of SCAN with respect to lattice constants in comparison to PBE and PBEsol, as can be seen in Table 2.2, follows from the fact that SCAN yields a superior description of both the bonds within the MnO_6 octahedral environment and the weak electron density overlap between octahedra. It is worth noting the exceptional performance of PBEsol+U in reproducing the lattice constants here. While PBEsol underestimates lattice constants, the +U modification typically leads to larger lattice parameters by reducing the electronic overlap between atoms, counteracting the error in PBEsol. Consequently, PBEsol+U is able to minimize the lattice constant error for an optimal choice of U-value[58].

For all the properties of MnO_2 that we have considered (polymorph formation energy, band gap, magnetization, and lattice constants), SCAN is the only functional to give high-quality, *ab-initio* results in agreement with experiment across the board. In contrast, the empirically-fitted PBEsol+U functional performs as well as or better than SCAN on band gaps and lattice constants, but mispredicts the polymorph order and the magnetic character of the system. PBEsol performs well on the polymorph order and magnetization, but significantly underestimates lattice constants and band gaps. HSE, while being much more computationally expensive than all other functionals tested here, only performs well on lattice constants. The consistent agreement between SCAN and experimental results across multiple properties suggests that SCAN, more so than other functionals, is able to capture the physics governing the system rather than acting as a fortuitous correction that improves a target property. We propose that the reason for this superior and consistent performance lies in the design features of SCAN - its built-in agreement with numerous limiting constraints on the exchange-correlation energy, and the inclusion of appropriate norms for which semi-local functionals can be exact or nearly-exact, which serve to guide the functional from one constraint to another. We expect similarly positive results on other transition metal oxides with high-spin configurations and less-than half-full d shells, and somewhat worse results in more self-interaction-dominated systems. However, much more extensive calculations are needed to fully explore the accuracy of SCAN across other chemical spaces.

In conclusion, we have investigated the accuracy of several common DFT functionals, as well as the recently introduced SCAN meta-GGA, with respect to their ability to reproduce key properties of the challenging MnO_2 system. Specifically, we looked at the relative stability, band gaps, magnetic structure, and lattice constants of the β, R, α, γ, λ, and δ phases on MnO_2. We found that although each individual property can be reproduced to good agreement with experiment by several functionals, only SCAN gives quantitatively reliable results for all properties at once. The accuracy, reliability, and computational efficiency of this new functional opens the door to the rigorous theoretical study of the manganese oxide system, from its still-uncertain basic physics to the complex mechanisms underlying the rich catalytic, electrochemical, and optoelectronic behavior of this material.

2.5 General performance across binary compounds

Generalizing from the favorable performance of SCAN in reproducing the properties and energetics of MnO_2 polymorphs, we examine the performance of this exchange–correlation functional more broadly, focusing specifically on the question of phase stability across binary ionic compounds. The ability to evaluate chemical stability, i.e., whether a stoichiometry will persist in some chemical environment, and structure selection, i.e. what crystal structure a stoichiometry will adopt, is critical to the prediction of materials synthesis[89], reactivity[26, 27] and properties[53]. We demonstrate that SCAN[11] is able to address both facets of the stability problem reliably and efficiently for main group compounds, while transition metal compounds are improved but remain a challenge. SCAN therefore offers a robust model for a significant portion of the periodic table, presenting an opportunity for the development of novel materials and the study of fine phase transformations even in largely unexplored systems with little to no experimental data.

For known materials, the question of solid phase stability can be resolved experimentally through a variety of calorimetric techniques, which yield the enthalpy of formation(ΔH_f). In the prediction of new materials however, the formation enthalpy must be calculated from first-principles, which is most commonly done using DFT with the well-established Perdew-Burke-Ernzerhof (PBE)[9] density functional. Furthermore, in the evaluation of solids differing in structure, but not chemistry, the differences between the formation enthalpies of competing phases often lie on a very fine energy scale, and are very difficult to measure experimentally, motivating their calculation from first-principles[90].

Due to the diversity of chemical degrees of freedom, from subtle structural differences to changes in bonding characteristics, it is challenging for first-principles methods to tackle both facets of the stability problem at reasonable computational cost. High–level wavefunction methods[91] (e.g., the configuration interaction or quantum monte carlo approaches) can achieve accuracy comparable to calorimetry, but they are limited to systems having a relatively small number of electrons per periodic unit cell due to their high computational cost. DFT[4, 92, 93, 94], with the PBE[9] generalized gradient approximation to its exchange-correlation energy currently is the dominant approach for calculation due to its relatively cheap computational cost and reasonable accuracy. Unfortunately, errors in formation enthalpy predicted by PBE are usually at the level of $\approx$0.2 eV/atom (see Figure 2-4), which is not sufficient for the comparison of competing formation reactions, especially those leading to chemically similar solids. We find that SCAN[11] halves the errors of PBE in predicting formation enthalpies of about 200 binary solids[95], while retaining a comparable efficiency to PBE. Remarkably, SCAN also yields a significant improvement in the reliability of crystal structure selection, consistently halving the error rate in ground state selection accuracy and reducing the error in the relative energies of crystal structures. While the computational cost of SCAN is modestly greater than (usually 2 to 3 times) that of PBE, it is much less (in general by an order of magnitude in plane-wave codes) than that of hybrid functionals, and very much less than that of wavefunction methods.

To systematically compare the behavior of SCAN and PBE, we group chemistries by how they are affected by known errors in semi-local density functionals. The three major sources of error in PBE are the self-interaction error (SIE), the incomplete error cancellation between the target compound and the elemental references, and the absence of van der Waals interactions. SIE is intrinsic to all semi-local density functionals, among which are PBE and SCAN. SIE manifests itself in transition metal compounds, especially in semiconducting and insulating oxides, more than in main group compounds due to the presence of valence d electrons that localize more than valence sp electrons[37]. The late $3d$ elements Cr, Mn, Fe, Co, and Ni are especially problematic. To resolve SIE in true first-principles spirit, non–local corrections are necessary, which are typically computationally expensive and scale poorly with system size. Therefore, we first address the behavior of main group compounds so as to characterize the performance of PBE and SCAN as efficient semi-local functionals largely in the absence of SIE.

The evaluation of the enthalpy of formation is based on 196 binary compounds with 101 main group systems and 95 systems containing transition metals (see Appendix A). The analysis of structure selection accuracy is based on 297 ionic binary chemistries, of which 191 are main group compositions and 106 contain transition metals (see Appendix A). In the choice of chemistries, we choose only compositions for which the low-temperature, low-pressure ground-state crystal structure is known experimentally. The chemistries included in this sample are comprised of compositions chosen to benchmark formation enthalpy, AB-type ionic compounds, and a selection of binary compositions previously enumerated in crystal structure prediction studies[20]. To the best of our knowledge, this selection of chemistries does not introduce any bias in the likelihood of structure selection error not present more generally in binary main group and transition metal compounds. For each chemistry, we consider experimentally reported crystal structures from the Inorganic Crystal Structure Database[19], as well as likely structures predicted by data mined elemental substitution methods[20], giving a total of 3026 crystal structures. Finally, to determine whether or not a DFT-relaxed crystal structure matches the experimentally reported structure, we rely on a distortion-tolerant affine map, implemented as the StructureMatcher algorithm in the Pymatgen package[96]. All calculations are performed using the Vienna Ab-Initio Simulation Package (VASP)[5, 6] using the projector augmented wave (PAW) method[8] with a reciprocal space discretization of 25 Å^{1} and a plane wave energy cutoff of 520 eV. In magnetically active systems, the energy is taken as the lowest of a ferromagnetic and a sample of small–unit–cell antiferromagnetic orderings. All calculations are converged to 10^{6} eV in total energy and 0.01 eV/Å on atomic forces.

As shown in Figure 2-4a, the mean absolute error (MAE) of SCAN in the formation enthalpy of 102 main group compounds is 0.084 eV/atom, about 2.5 times lower than that of PBE, while the MAE of SCAN for the 21 main group oxides shown in

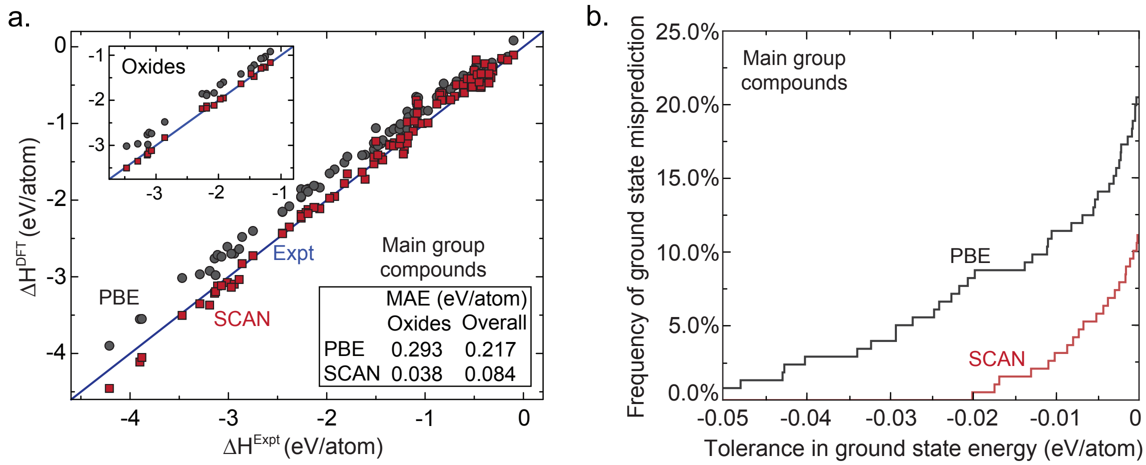

Figure 2-4: SCAN provides a significant improvement over PBE in computing the absolute and relative stability of main group compounds. **a.** The formation enthalpy of main group compounds, and oxides in particular. **b.** The probability that the computed energy of a predicted structure with respect to that of the experimental ground state structure lies below a threshold energy or tolerance across main group compounds, for a range of tolerances.

the inset is 0.038 eV/atom. The reduction in error afforded by SCAN relative to PBE originates from the fact that PBE is not able to simultaneously and accurately treat the different types of chemical bonds[11, 12] (covalent, metallic, ionic, hydrogen, and van der Waals) found in a compound and its constituent elemental phases, leading to the well-known imperfect error cancellation, e.g., between the molecular O_2 reference and metal oxides[59]. SCAN, on the other hand, is able to capture the behavior of all such interactions by introducing the Kohn-Sham kinetic energy density into the functional in a way that satisfies all known limiting behaviors and constraints on electronic interaction appropriate to semilocal functionals[11]. This construction leads to a widely-predictive functional[97]. In particular, without being fitted to any bonded system, SCAN captures even the intermediate-range van der Waals attraction between neighboring atoms in a solid, which PBE largely neglects. Furthermore, PBE underestimates the chemical stabilities of most solids, for example erroneously making InN chemically unstable, an error which SCAN avoids. These errors arise largely from PBE's over-stabilization of reference molecules, and could not be fixed by simply adding a van der Waals correction to PBE.

An even stronger indication of the general reliability of SCAN for stability calculations is its superior performance in identifying ground state crystal structures. Here the intermediate-range van der Waals interaction, present in SCAN but not in PBE, can play a particularly important role, for example by stabilizing the correct CsCl structure in the heavy halides CsCl, CsBr, and CsI. Based on 191 stoichiometric main group binary compounds with 1659 experimentally-reported and predicted crystal structures, we identify the most stable low-temperature, low-pressure phases within PBE and SCAN. We then evaluate the frequency with which PBE or SCAN stabilizes an incorrect ground-state structural polymorph in comparison to the experimental structure. The zero-temperature ground state crystal structure is thermodynamically defined as the phase of lowest enthalpy, as, under these conditions, enthalpy is exactly equal to the system Gibbs free energy. Thus, the relative zero-temperature DFT-computed energies of competing crystal structures provide a nearly complete representation of their relative Gibbs free energies under these conditions, omitting the change in zero-point vibrational energy which is on the scale of 0.005 eV/atom[98, 99, 100, 101], ambient pressure effects, which lie on the scale of 0.001 eV/atom, and smaller contributions. To account for these effects, as well as other potential noise in the calculations, we introduce a tolerance on structure selection ΔE_{tol}, and count the frequency with which PBE or SCAN erroneously stabilize a crystal structure by more than ΔE_{tol} with respect to the experimental ground state structure. As can be seen in Figure 2-4b, SCAN provides a significant improvement over PBE in selecting the correct ground state structure, reducing the frequency of structure prediction error from 12% to just 3% at a 0.01 eV/atom tolerance, where the improvement in structure selection accuracy likely originates from the more accurate physical model provided by SCAN relative to PBE. Notably, as the energy scale of competing crystal structures[24, 22, 30] is far below the average error suggested by total formation enthalpy statistics discussed earlier, it is evident that reliable structure selection is a sensitive indicator of how well a functional captures fine details in the relative stability of chemically-similar phases.

These structure selection results highlight the difficulty of reliable structure prediction in first-principles calculations. While PBE yields close to a 21% error rate in structure selection in absolute terms and a 12% error rate with a 0.01 eV/atom tolerance, this error rate is likely a lower bound as no method we are aware of can guarantee that no other crystal structures exist with a lower energy for any given chemistry. Conversely, experimental uncertainties in ground-state crystal structure originating from difficult to observe low temperature phase transitions, small off stoichiometries, and other errors mean that even the exact functional would likely not be able to achieve complete agreement with experiment. In this light, SCAN's 3% error rate within the 0.01 eV/atom tolerance is remarkable. The impact of this improvement is immediately visible - for example, in SiO_2, SCAN is necessary to reproduce the correct α-quartz low-temperature, low-pressure ground state structure, and correspondingly, the pressure-temperature phase diagram, as PBE overstabilizes the high-temperature β-cristobalite polymorph. The intermediate-range van der Waals interaction in SCAN stabilizes the correct, higher-density quartz phase of this earth-abundant material. Taken together with the promising performance in predicting formation enthalpy, these results suggest that SCAN is highly reliable for both the absolute and relative stability of the main group compounds.

We now turn to transition metal compounds, where self-interaction error poses a fundamental limitation on the performance of semi-local density functionals. For the formation enthalpies of 98 transition metal binaries, Figure 2-5b shows that SCAN still has an MAE of 0.122 eV/atom, which is significantly larger than that of the main group compounds. However, SCAN still improves over PBE by about 0.08 eV/atom, or 40% of the total PBE error, for the transition metal compounds. Similarly, as can be seen in Figure 2-52b, based on 106 transition metal binary compounds with 1366 experimental and predicted structures, SCAN still gives a significant improvement relative to PBE in structure selection accuracy, although the absolute performance of both functionals is much worse than that in the main group compounds, both in the

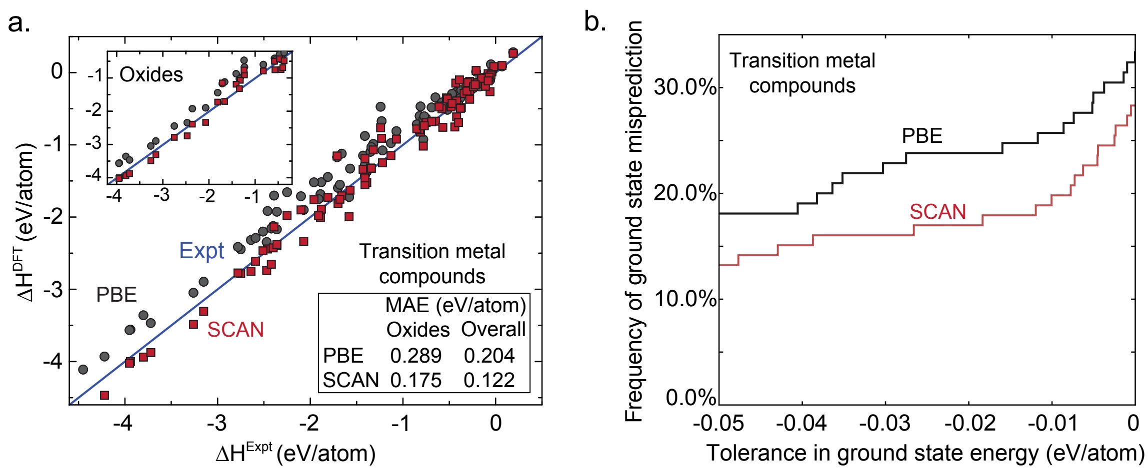

Figure 2-5: SCAN considerably reduces the average error in formation enthalpy and structure selection error frequency relative to PBE in transition metal compounds, which are more difficult than are the main group compounds due to the increased contribution of the self-interaction error. (**a.**) The enthalpy of formation of transition metal binary compounds, and oxides in particular. (**b.**) The probability of incorrect structure selections by PBE or SCAN across transition metal compounds, for a range of tolerances.

frequency of structure selection errors and their energetic magnitude. The fact that this discrepancy persists even at a 0.02 eV/atom tolerance, where the SCAN error rate in main group chemistries approaches zero, suggests that further improvements in functional performance would require a fundamentally different approach, moving to non-local functional forms or explicit self-interaction corrections[102, 103, 104].

A number of different approaches have been developed to deal with the imperfect error cancellation of PBE, such as the fitted elemental-phase reference energies (FERE) scheme[105], and other schemes with fitted corrections to elemental and molecular reference states[59, 106]. These corrections assume that most of the error in compound formation enthalpy depends only on the overall composition, and attempt to eliminate this error by using the total energies of elemental phases as fitting parameters. In the case of FERE, with about 30 fitting parameters, the PBE MAE is reduced from 0.250 eV/atom to 0.052 eV/atom for a set of 110 main-group binary solids which largely overlaps our testing set. However, neither FERE nor the other composition-based schemes can provide the correction to PBE needed to predict the relative stability of different phases of a compound, which is critically important for structure selection and by extension, the prediction of properties which depend on local structural changes rather than simply the average composition. Furthermore, fitting schemes, based on common structures and thus common geometries and oxidation states, are difficult to generalize outside of their initial fitting data, especially to situations where rare electronic configurations may give rise to unexpected errors not accounted for by the fitted correction[106].

The development of semilocal exchange–correlation functionals in DFT has been driven by the promise of these approximations to efficiently evaluate the stability and properties of both known and predicted solid phases. The SCAN functional, without any fitted corrections, approaches experimental accuracy in both total energy and the relative stability of solid phases across main group compounds, and the remaining challenges to DFT functionals appear to be self-interaction error dominated systems. Correspondingly, future improvement in general-use functional performance will require a solution to the self-interaction problem and a representation of non-local phenomena.

2.6 Correction of oxidation potential error in SCAN

While the generally accurate representation of transition metal compounds in SCAN will require the resolution of self–interaction error, likely requiring non–local functionals, it is possible to significantly improve the reliability of SCAN results in this space through a judicious choice of thermodynamic reference state. The primary impact of electronic self–interaction error is to understabilize all occupied states with respect to the unoccupied states, decreasing band gaps and oxidation potentials[82]. This error can be compensated by penalizing partial occupancy and destabilizing unoccupied states, such as in the case of the Hubbard U correction, but this approach requires the fitting of an arbitrary U parameter, and as described earlier in this chapter, leads to errors in magnetism and structure selection. In order to preserve the benefits of the SCAN functional with regard to accurate structure selection, magnetic configuration, and bond lengths, while alleviating the error in oxidation potential, a post–hoc correction scheme can be used.

The core assumption of the correction scheme presented here is that the dominant source of error in transition metal compounds is the oxidation potential of the transition metal, rather than the energy of the reference elemental phase as had been assumed in previous works[105, 59, 106]. Under this assumption, the error in formation energy can be largely eliminated by decomposing the formation energy of a transition metal compound into two steps. The first step is the formation of the transition metal ion in its correct oxidation state from the elements, which can be obtained from experimental data or high–accuracy calculations. The second step is the formation of the target compound from this intermediate through reactions preserving the transition metal oxidation state, computed in SCAN. Thus, the SCAN calculation is only responsible for reproducing the energies of reactions preserving transition metal oxidation state, for which self–interaction error largely cancels out. While it is still necessary for SCAN to reproduce oxidation energy of main group anions, the error associated with these reactions is much lower, as evidenced by the favorable performance of SCAN among main group chemistries.

Mathematically, this correction scheme for formation energy can be written as

$$\begin{aligned}\Delta E_f^{corr}\left[M^{n+}X_b^{m-}\right] =& E^{DFT}\left[M^{n+}X_b^{m-}\right] - E^{DFT}\left[M^{n+}Y_c^{p-}\right]\\&- bE^{DFT}\left[X^0\right] + cE^{DFT}\left[Y^0\right]\\&+ \Delta H_f^{exp}\left[M^{n+}Y_c^{p-}\right]\end{aligned}$$

where M^{n+} represents a transition metal in the $+n$ oxidation state, X^{m-} and Y^{p-} represent main–group anions in the $-m$ and $-p$ oxidation states respectively, E^{DFT} represents energy computed in DFT, and H^{exp} represents experimentally–obtained enthalpy.

A practical implementation of this referencing scheme can be obtained from a further simplification - the substituted anion Y and associated reference intermediate $M^{n+}Y_c^{p-}$ may be the same for all transition metal ions M^{n+}.

$$
\begin{aligned}
\Delta E_f^{corr}\left[M^{n+}X_b^{m-}\right] =& E^{DFT}\left[M^{n+}X_b^{m-}\right] - E^{DFT}\left[M^{n+}Y_c^{p-}\right] \\
& - bE^{DFT}\left[X^0\right] + cE^{DFT}\left[Y^0\right] \\
& + \Delta E_f^{DFT}\left[M^{n+}Y_c^{p-}\right] \\
& - \left(\Delta E_f^{DFT}\left[M^{n+}Y_c^{p-}\right] - \Delta H_f^{exp}\left[M^{n+}Y_c^{p-}\right]\right) \\
=& E^{DFT}\left[M^{n+}X_b^{m-}\right] - \left(E^{DFT}\left[M^0\right] + bE^{DFT}\left[X^0\right]\right) \\
& - \left(\Delta E_f^{DFT}\left[M^{n+}Y_c^{p-}\right] - \Delta H_f^{exp}\left[M^{n+}Y_c^{p-}\right]\right) \\
=& \Delta E_f^{DFT}\left[M^{n+}X_b^{m-}\right] - c_Y\left[M^{n+}\right]
\end{aligned}
$$

where $c_Y\left[M^{n+}\right] = \Delta E_f^{DFT}\left[M^{n+}Y_c^{p-}\right] - \Delta H_f^{exp}\left[M^{n+}Y_c^{p-}\right]$ is a correction factor to the formation energy of the transition metal ion M in the $+n$ oxidation state. Thus, an equivalent form of this correction scheme is a simple constant correction factor for the total energy of any transition metal ion, derived to compensate for the self–interaction induced error in SCAN.

A simple choice for these states are the binary oxides ($Y = \mathrm{O}$) as their experimental formation energies are well known, covering the majority of oxidation states for the common transition metals. Furthermore, while the binding energy of the oxygen molecule, and thus the oxidation potential of oxygen, has historically been highly inaccurate in DFT[59], SCAN eliminates this error as evidenced by the low error in the formation energy of main group oxides shown in Figure 2-4. The correction factors c_O derived for the redox active $3d$ transition metals based on the binary oxides are given in Figure 2-6.

The implementation of this referencing scheme significantly reduces the error in the

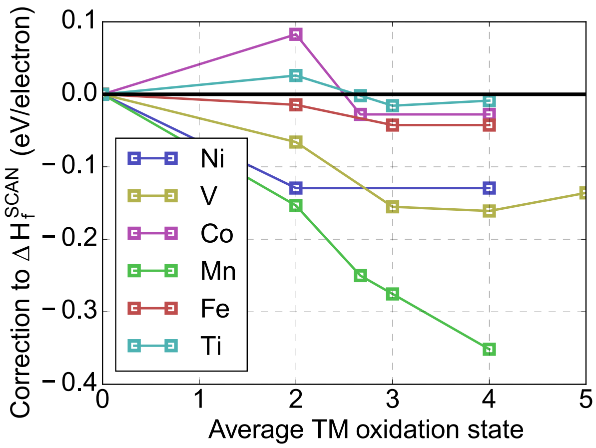

Figure 2-6: Correction factor for the SCAN oxidation potential of the $3d$ transition metals derived from the binary oxides.

formation energies of ionic transition metal compounds, bringing this error in line with that of the main group compounds. While more thorough benchmarking is necessary to ascertain precise values for the formation energy error, selected tests consistently yield consistent error values between errors typical of main group compounds and transition metals, indicating that the correction scheme largely eliminates transition–metal specific errors. One precise test of this referencing scheme is the oxidation potential of Li- and Na-ion cathode compounds, which are known to high accuracy from experimental electrochemical data. Formally, the oxidation potential is defined as

$$V = -\frac{G_f\left[Li_xMX\right] - \left(xG_f\left[Li\right] + G_f\left[MX\right]\right)}{xe}$$

where Li_xMX represents a lithiated compound and MX represents the delithiated compound. As entropic effects are typically negligible, the Gibbs free energy of formation can be approximated by the enthalpy of formation, which itself is approximated by the computed DFT energy of formation. Figure 2-7 shows the error in the computed oxidation potentials of a range of Li- and Na-ion cathode materials, with respect to the experimentally–measured oxidation potentials[37, 107, 108]. It is clear that the referencing scheme corrects a large fraction of SCAN error in oxidation potential, bringing SCAN results closer to experiment and results obtained from the hybrid HSE functional[34, 37] or empirically–fitted PBE+U approach[59]. Whereas SCAN without any correction has a mean absolute error of 0.296V within this dataset, the correction scheme reduces the error by half to 0.167V, below that of HSE and PBE+U, which have mean absolute errors of 0.228V and 0.242V respectively.

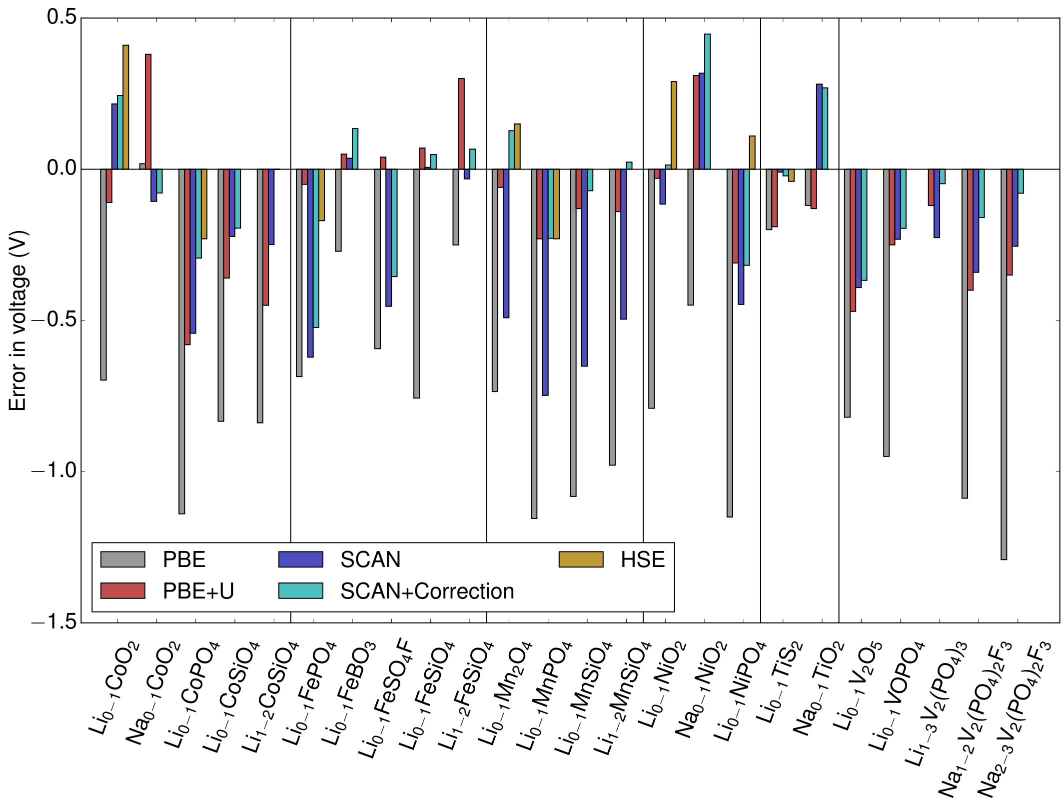

Figure 2-7: The error in the electrochemical oxidation potential of various Li- and Na-ion batteries, as compared to the experimentally reported voltage[37, 107, 108], for a range of functionals, as well as the SCAN correction scheme ("SCAN+Correction"). In the case of PBE+U, the U value is fit to oxide formation energies following previous benchmarking[59].

2.7 Conclusion

To summarize, in this chapter, I have identified the SCAN meta-GGA exchange–correlation functional as a general–use functional in the analysis of synthesis reactions. I have argued that the accurate representation of non–covalent interactions and medium–range van der Waals forces within SCAN yields accurate energies for chemistry–preserving reactions, resulting in the reliable identification of ground state crystal structures and their properties. I then derived a thermodynamic referencing scheme, which eliminates most of the error in reactions which involve electron transfer, yielding accurate energies of formation across the periodic table. The accurate representation of energies among both similar and dissimilar chemistries is essential for analyzing the evolution of a synthesis from precursor to product, making SCAN and the referencing scheme described here the ideal toolset for first–principles synthesis prediction.

Chapter 3

Phase selection during nucleation - the case of FeS_2

In this chapter, I apply the quasi-thermodynamic view of synthesis described in Section 1.3 to understanding the formation of the pyrite and marcasite polymorphs of FeS_2 during hydrothermal growth. I demonstrate that phase selection in this system can be explained by the surface stability of the two phases as a function of ambient pH within nano-size regimes relevant to nucleation. This result suggests that a first-principles understanding of nano-size phase stability in realistic synthesis environments can serve to explain or predict the synthetic accessibility of structural polymorphs, providing a guideline to experimental synthesis design.

The content of this chapter is based, often verbatim, on a previously published manuscript:
D. A. Kitchaev, G. Ceder. "Evaluating structure selection in the hydrothermal growth of FeS_2 pyrite and marcasite" *Nature Communications*, 7, 13799 (2016)

3.1 Hydrothermal growth of FeS_2 polymorphs

Nucleation and growth from solution remains one of the most experimentally and geologically important synthesis methods for crystalline solids. Hydrothermal growth, which involves precipitation from a superheated aqueous solution of precursor salts, is a particularly common route for natural mineral formation and synthetic single-crystal growth[109]. Despite the importance of this method, recipes for the hydrothermal growth of target solid phases remain largely empirical. At the same time, phase formation during hydrothermal growth is relatively well characterized by an initial nucleation step from a homogeneous aqueous solution, followed by particle growth, all occurring without significant diffusion limitations. The importance and inherently near–thermodynamic nature of this process makes hydrothermal growth an ideal initial test case for the quasi–thermodynamic analysis of metastable phase formation.

We base our study of hydrothermal phase selection on the FeS_2 mineral system due to its engineering relevance[110, 111], geologic importance[112, 113, 114], and unresolved structure selection mechanism[113]. The FeS_2 system contains two common phases - pyrite and marcasite - and while hydrothermal recipes for the synthesis of both phases are established[112, 115, 116, 117], the underlying forces governing phase selection during growth are not understood[113]. It is known that marcasite can be grown as the dominant phase below pH=5 [115, 112, 116], despite pyrite being the thermodynamic ground state of bulk FeS_2[118]. However, the mechanism by which pH influences phase selection in FeS_2 is unclear as it does not affect the relative stability of bulk pyrite and marcasite[115, 113, 119, 120].

Here, we quantify phase selection during the hydrothermal growth of FeS_2 by evaluating the full thermodynamic potential governing the evolution of the system throughout the growth process. The thermodynamics describing particle growth in solution are given by the sum of bulk and surface energy, which scales as $\Phi = \frac{4}{3}\pi r^3 g_\mathrm{b} + 4\pi r^2 \overline{\gamma}$ where g_b is the volumetric bulk Gibbs free energy of formation, $\overline{\gamma}$ is the particle-averaged surface energy, and r is the particle size[25]. Following the formalism outlined above, we propose that the effect of pH can be understood in terms of nucleation and growth from solution which incorporates this competition between bulk and surface stability[121, 23, 122, 21]. Contrary to the bulk, the surface energies of the two phases vary with pH due to the adsorption of H^+ and OH^- ions[123, 124, 125]. By accounting for adsorption in the evaluation of surface energy, we are able to fully account for the effects of solution chemistry in a theoretical treatment of synthesis, accounting for "spectator ions" that influence growth through the surface of the material, but are not represented in the chemical formula of the bulk product.

We evaluate $\Delta\Phi = \Phi_{\text{marcasite}} - \Phi_{\text{pyrite}}$, the driving force for the formation of the marcasite phase with respect to pyrite, at all stages of growth, and as a function of the growth environment. The bulk energy of the growing crystal is determined by the energy of the pure crystal, along with contributions from defect formation, off-stoichiometry, and strain. In this work, however, we focus on the growth of pure FeS_2 pyrite and marcasite, assuming the bulk energy of both phases to be that of their stoichiometric configuration[126]. The energy of the solid-liquid interface is governed by a combination of bulk-like bond breaking and off-stoichiometry due to adsorption and segregation. It is convenient to approximate the interface energy by the sum of a solid-solvent interface energy and the free energies of adsorption for solute species within the electrostatic double layer, neglecting in this case segregation from the bulk solid. Thus, we separately compute the free energy of a pristine interface between the stoichiometric solid and solvent, $\left(G^{\text{surface+solvent}} - G^{\text{bulk}}\right)$, and the free energy of adsorption of solutes from the solution and segregation of species from the bulk, $\Delta\mu_i^{\text{ads.}}$, giving us all the information necessary to obtain the free energy of the solid-liquid interface, $\gamma A = \left(G^{\text{surface+solvent}} - G^{\text{bulk}}\right) + \sum N_i^{\text{ads.}}\Delta\mu_i^{\text{ads.}}$. While in principle, adsorption-induced segregation can be included[127], we do not include this coupling for FeS_2 as no significant segregation is to be expected in this compound. By evaluating the thermodynamics relevant to FeS_2 particle growth from first-principles, we find that the transition from pyrite to marcasite growth under acidic conditions may be explained by the pH-dependent stability of the surfaces of the two phases, suggesting that the quasi–thermodynamic vision of synthesis described here may serve as a valid and computationally-accessible metric of the synthesizability of metastable materials.

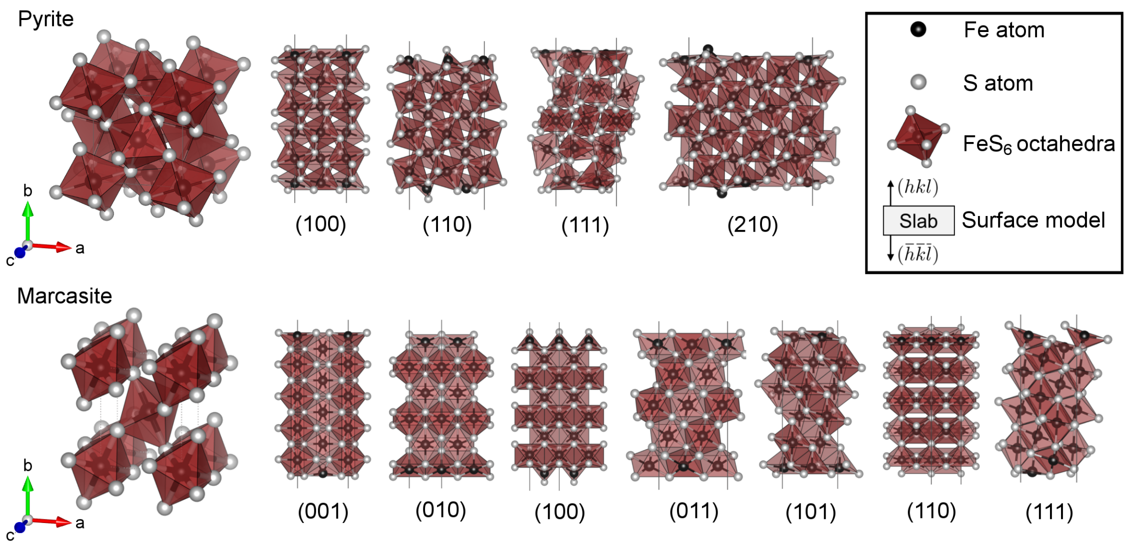

Figure 3-1: Structure of FeS_2 bulk and surface slab models. The structures of FeS_2 pyrite (top) and marcasite (bottom) bulk, as well as the relaxed surface slab models of the significant crystallographic facets of both phases. The surface structures represent 2D periodic slabs of a thickness large enough such that the few middle layers of the slab are energetically "bulk-like", while the top and bottom layers capture the structure and energetics of the (hkl) and $(\bar{h}\bar{k}\bar{l})$ facets respectively.

3.2 Formalism and computational methods

3.2.1 Thermodynamic model of an aqueous interface

The defining feature of an aqueous interface is the existence of an electrostatic double layer due to the adsorption of charged species on the solid[128]. However, much of the complexity of the double layer can be neglected when calculating the total energy of the interface. To derive an approximate treatment of this structure, it is helpful to break down the electrostatic double layer into three components: the electronic "space charge" region, the chemisorbed region within the Helmholtz plane, and the physisorbed "diffuse" region outside the Helmholtz plane, as shown schematically in Figure 3-2a. The adsorption energy of chemisorbed species is likely large, and thus must be represented accurately, accounting among other features for the charge state

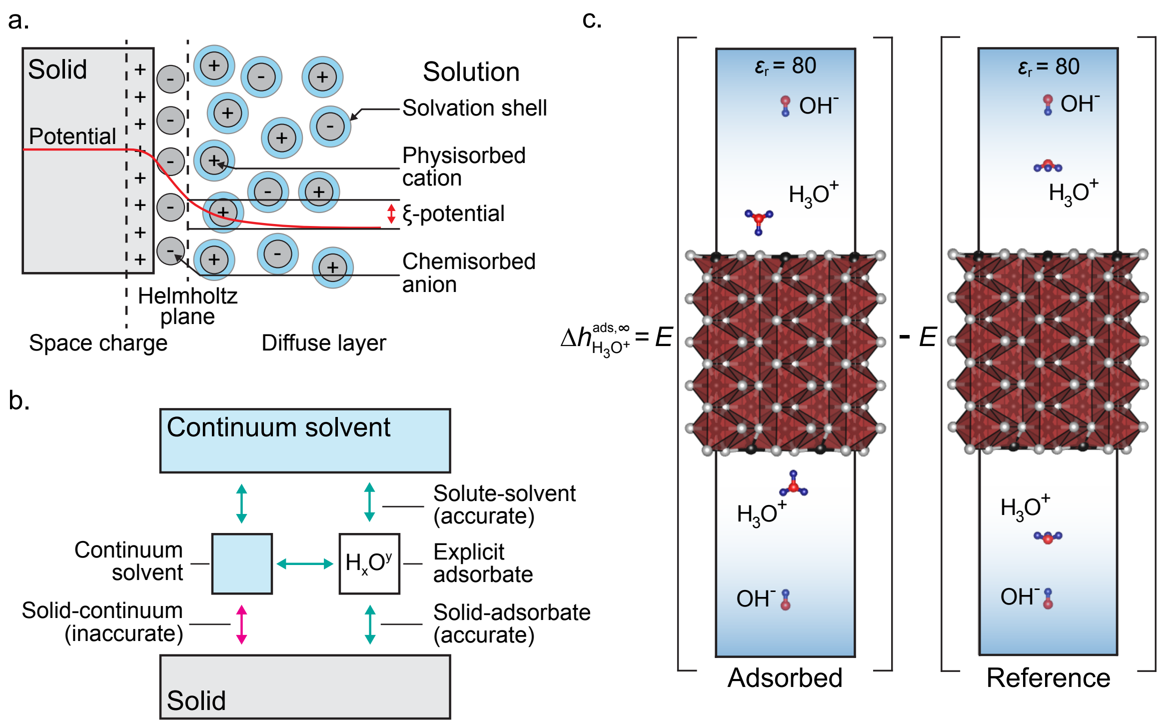

Figure 3-2: Scheme for computing the free energy of an aqueous interface. **a**. The structure of an electrostatic double layer, consisting of a space charge in the solid, a tightly bound chemisorbed layer within the Helmholtz plane, and weakly bound physisorbed ions in the diffuse layer. **b**. The continuum solvation model provided by VASPsol, which accurately captures the interactions between solute molecules and the solvent, as well as the solvent with itself, but does not accurately represent the interactions between the solvent and an extended solid surface. We introduce a solvation scheme to correct the unreliable solid-solvent interaction with a more physical model calculated from the explicit adsorption of water molecules. **c**. To calculate the adsorption energy of charged ions at infinite dilution, we choose a calculation scheme that allows electron transfer between the cationic and anionic species to occur self-consistently. In both the adsorbed and reference states, the ions are sufficiently separated to allow the continuum solvent to partially screen the interactions between them, such that the effect of the electrostatics can be subtracted out analytically as a post-calculation correction. Here, we show the adsorption of H_3O^+ onto a sulfur site on the marcasite (001) surface as an example of this calculation, within the VASPsol continuum solvent model.

of the adsorbate. The space charge region in the solid arises due to the changes in the electronic structure of the solid associated with bond breaking and adsorption from the liquid, and thus will be captured intrinsically by any accurate first principles model of the surface and the chemisorbed layer. In contrast, the contribution of the diffuse layer to the total energy of the system is not always significant. The electrostatic potential at the Helmholtz plane, experimentally measured as the ξ potential, is typically on the order of 40 mV [124, 123], while the capacitance of the double layer region is on the order of 0.5 F m^{-2} [124, 123], meaning that the total energy stored in the diffuse layer is on the order of 10^{-4} J m^{-2}. This quantity is negligible on the scale of total interfacial energies in ceramic-aqueous systems, which are in the range of 1 J m^{-2}[24]. Thus, a model of the chemisorbed species within the Helmholtz plane, constructed to ensure the correct charge state of the adsorbed species, but neglecting the details of the diffuse layer, yields an accurate estimate of the true interfacial energy, even in the presence of an electrostatic double layer.

To fully model a solid-liquid interface, it is generally necessary to consider the adsorption of all ions present in solution. A more tractable simplification is to consider only the effect of known potential-determining ions, as these ions are by definition those which adsorb strongest and thus determine the structure of the double layer. In the case of FeS_2, the potential-determining ions are H_3O^+ and OH^-[123, 124], suggesting that in an aqueous medium, the tightly-bound chemisorbed layer consists primarily of these species, in addition to the H_2O solvent molecules. Thus, it is only necessary to consider the adsorption of OH^-, H_2O, and H_3O^+, accounting for all other ions only to the extent that they set the ionic strength and pH of the solution. The energy of adsorbing H_2O is equivalent to the energy of solvating the solid surface, and will be addressed in a later section. Further, we assume that at a given pH, OH^- and H_3O^+ will never be adsorbed simultaneously. Based on this set of assumptions, the adsorption energy of the two ions can be written based on the minimization of the free energy of adsorption, given by the enthalpy ΔH^{ads} and entropy ΔS^{ads} of adsorption with respect to the number of adsorbates N^{ads}:

$$N^{\mathrm{ads}}_{\mathrm{H_3O^+}} \Delta\mu^{\mathrm{ads}}_{\mathrm{H_3O^+}} = \min_{N^{\mathrm{ads}}_{\mathrm{H_3O^+}}} \left[\Delta H^{\mathrm{ads}}_{\mathrm{H_3O^+}} - T\Delta S^{\mathrm{ads}}_{\mathrm{H_3O^+}}\right]$$

$$N^{\mathrm{ads}}_{\mathrm{OH^-}} \Delta\mu^{\mathrm{ads}}_{\mathrm{OH^-}} = \min_{N^{\mathrm{ads}}_{\mathrm{OH^-}}} \left[\Delta H^{\mathrm{ads}}_{\mathrm{OH^-}} - T\Delta S^{\mathrm{ads}}_{\mathrm{OH^-}}\right]$$

We approximate the enthalpy of adsorption ΔH^{ads} by accounting for adsorbate-solid, adsorbate-solvent, and adsorbate-adsorbate interactions. The adsorbate-solid and adsorbate-solvent interactions are captured by the enthalpy of adsorption at infinite dilution $\Delta h^{\mathrm{ads},\infty} = E^{\mathrm{ads}} - E^{\mathrm{ref}}$, where E^{ads} and E^{ref} are the DFT energies of the ion adsorbed onto the solid and in solution respectively, shown schematically in Figure 3-2c. Note that this energy of adsorption includes the energy of desorbing a water molecule, as the adsorption process is competitive with the pure solvent. We approximate adsorbate-adsorbate interactions with the Debye-Huckel model of screened electrostatics in an electrolytic medium, given here by V^{el}. Thus, we can write the enthalpy of adsorption for OH^- and H_3O^+ as:

$$\begin{aligned}
\Delta H^{\mathrm{ads}}_{\mathrm{H_3O^+}} &= N_{\mathrm{H_3O^+}}\left(E^{\mathrm{ads}}_{\mathrm{H_3O^+}} - E^{\mathrm{ref}}_{\mathrm{H_3O^+}}\right) + V^{\mathrm{el}} \\
\Delta H^{\mathrm{ads}}_{\mathrm{OH^-}} &= N_{\mathrm{OH^-}}\left(E^{\mathrm{ads}}_{\mathrm{OH^-}} - E^{\mathrm{ref}}_{\mathrm{OH^-}}\right) + V^{\mathrm{el}} \\
V^{\mathrm{el}} &= \frac{1}{2}\sum_{i\neq j}\frac{q_i q_j e^{-|\mathbf{r}_i-\mathbf{r}_j|/\lambda}}{4\pi\epsilon_r\epsilon_0|\mathbf{r}_i-\mathbf{r}_j|}
\end{aligned}$$

where $\mathbf{r}_i$ are the positions of the adsorbed ions on the solid surface, λ is the Debye screening length of the solution, and ϵ_r is the dielectric constant of the solution near the interface. In our model, we use a Debye screening length of $\lambda = 1.0$nm, based on an average over screening lengths for reported synthesis recipes for pyrite and marcasite[115]. As we are considering the 2D electrostatic interactions between adsorbates, screened by adsorbed water molecules, we set the dielectric constant $\epsilon_r = 12$, estimated from reported experimental and computed values of the dielectric constant of interfacial water in similar systems[129, 130]. Finally, we set our temperature to 473K in accordance with the experimental conditions commonly reported for FeS_2 hydrothermal growth[115, 116].

To obtain the entropy of adsorption, we consider the entropy of the adsorbed and solution states of the ion, s^{ads} and s^{soln} respectively. The entropy of the adsorbed ion is well approximated by the configurational entropy over adsorption sites. The entropy of the ion in solution is given by the configurational entropy over the translational degrees of freedom of the ion in solution, which, assuming that OH^-, H_2O, and H_3O^+ all have approximately the same volume, is given by $k_B \log [x]$, where x is the mole fraction of the ion of interest. We then relate the entropy of H_3O^+ to pH by treating pH as an activity with respect to a 1M solution of H_3O^+ at standard state and assuming that the solution behaves ideally, which yields:

$$s^{\text{soln}}_{\text{H}_3\text{O}^+} = k_\text{B}\frac{T_0}{T}\ln M_\text{w} + 2.3k_\text{B}\ \text{pH}$$

where the M_w is the molarity of water and $T_0 = 300\text{K}$ is temperature in the reference state. Following the same assumptions, as well as the fact that OH^-, H_2O, and H_3O^+ are in equilibrium, we derive the entropy of OH^- in solution in terms of the calculated formation enthalpy of H_3O^+ and OH^- from $2H_2O$, which we denote Δh^0_w:

$$s^{\text{soln}}_{\text{OH}^-} = \frac{\Delta h^0_\text{w}}{T} - k_\text{B}\frac{T_0}{T}\ln M_\text{w} - 2.3k_\text{B}\ \text{pH}$$

A detailed derivation of these results is given in Appendix B. Combining the solution references with the configuration entropy of the adsorbed state, we have the entropy of adsorption for both H_3O^+ and OH^- in terms of pH:

$$\begin{aligned}
\Delta S^{\text{ads}}_{\text{H}_3\text{O}^+} &= N_{\text{H}_3\text{O}^+}\left(s^{\text{ads}}_{\text{H}_3\text{O}^+} - s^{\text{soln}}_{\text{H}_3\text{O}^+}\right) \approx N_{\text{H}_3\text{O}^+}\left(s^{\text{ads}}_{\text{H}_3\text{O}^+} - 2.3k_\text{B}\ \text{pH} - k_\text{B}\frac{T_0}{T}\ln M_\text{w}\right)\\
\Delta S^{\text{ads}}_{\text{OH}^-} &= N_{\text{OH}^-}\left(s^{\text{ads}}_{\text{OH}^-} - s^{\text{soln}}_{\text{OH}^-}\right) \approx N_{\text{OH}^-}\left(s^{\text{ads}}_{\text{OH}^-} - \frac{\Delta h^0_\text{w}}{T} + 2.3k_\text{B}\ \text{pH} + k_\text{B}\frac{T_0}{T}\ln M_\text{w}\right)
\end{aligned}$$

We have thus obtained a thermodynamic picture of ion adsorption that is efficiently computable from first principles and captures the primary trends we could expect to see at the solid-liquid interface as a function of pH. A similar analysis can be readily performed for other dissolved ions, based on their computed solubility product K_sp, generalizing this approach to a solid-aqueous interface with any ideal or near-ideal aqueous solution.

3.2.2 Computational implementation of the adsorption model

Based on the thermodynamic framework derived above, it is clear that in order to obtain a full quasi–thermodynamic picture of hydrothermal growth of FeS_2 pyrite and marcasite, only a few density functional theory calculations are necessary. First, we must calculate the bulk energy and structure of pyrite and marcasite. Then, for each low-energy crystallographic facet of each phase we must obtain the interfacial energy between the FeS_2 solid and water, or equivalently, the solvation energy of each crystal facet, $\left(G^{\text{surface+solvent}} - G^{\text{bulk}}\right)$. Finally, for each solvated facet, we must calculate the enthalpy of adsorbing dilute H_3O^+ and OH^- ions onto all likely adsorption sites, $\Delta h^{\text{ads},\infty}$. An example calculation illustrating the thermodynamic formalism can be found in Appendix C.

Table 3.1: Bulk thermodynamics of pyrite and marcasite. Calculated and experimental bulk parameters for pyrite and marcasite phases of FeS_2, as well as the most important crystallographic facets of both phases. References: [118, 131, 112, 126, 132, 133, 134]

Phase	**Lattice (Å)** (a, b, c)	$\mathbf{\Delta H_f}$ (meV/f.u.)	**Facets**
Pyrite (Pa3)	Calc: 5.329, 5.329, 5.329 Exp: 5.416, 5.416, 5.416	Calc: 0 Exp: 0	(100), (110), (111), (210)
Marcasite (Pnnm)	Calc: 4.371, 5.339, 3.347 Exp: 4.433, 5.426, 3.389	Calc: 8.3 Exp: 43 ± 2	(100), (010), (001), (110) (101), (011), (111)

All calculations were done using the Vienna Ab-Initio Simulation Package (VASP)[5, 6] implementation of density functional theory (DFT), using PAW pseudopotentials[135, 8] with a plane wave basis set using an energy cutoff of 520 eV. Consistently with previously reported results, we find that the PBEsol exchange-correlation functional[31] provides an accurate and computationally efficient model of FeS_2[28, 136], correctly stabilizing pyrite over marcasite as the ground state of the system in agreement with experiment[131, 112] and higher order functionals, although not quite reaching the experimentally measured transition enthalpy between the two phases[118] (see Table 3.1). While the SCAN [11] functional may provide more accurate results, following the discussion of chapter 2, this functional was not available at the time that this work was completed. To ensure consistency between the high-symmetry bulk calculations and low-symmetry adsorption calculations, we remove all symmetry restrictions from the calculation, giving the system identical relaxation degrees of freedom across all calculations. Finally, for bulk calculations, we choose a Γ-centered k-point mesh (6x6x6 for pyrite, 6x6x8 for marcasite) based on previously optimized calculation parameters in similar systems[13].

In our surface calculations, we consider the symmetrically distinct low-index facets of pyrite and marcasite previously reported to be significant. Specifically, in pyrite, we consider the (100), (110), (111), and (210) facets[132, 133], while in marcasite, we consider the (100), (010), (001), (110), (101), (011), and (111) facets[134], defined with respect to the unit cells given in Table 3.1. To generate the surface structures, we choose surface terminations that minimize the number and strength of bonds broken, evaluated based on the integral of charge density associated with each bond in question, and are maximally non-polar, following the Tasker surface stability criterion[137]. In the case where several surface terminations satisfy these criteria, we consider all such terminations. The resulting most stable (under solvated conditions) surface structures are shown in 3-1. While there is limited experimental data available to verify the accuracy of this approach, in the case of the well-characterized pyrite (100) surface, our approach leads to a surface structure consistent with that derived from LEED characterization[138]. Finally, we neglect the contribution of the solid to the solid-liquid interface entropy as it is known to be negligibly small in similar ceramic systems[139].

3.2.3 Solvation model

To account for solvation, we rely on the VASPsol continuum solvation model[140] to avoid the computationally prohibitive sampling of explicit solvent configurations. The VASPsol model serves two important purposes - it reproduces the mean-field interactions between ions and bulk solvent, and provides a dielectric medium which screens electrostatic interactions between charged adsorbates, their counterions, and their periodic images. However, while the VASPsol model is known to accurately reproduce the energy of solvating isolated molecules[140], its performance with respect to the solvation of solid surfaces is uncertain.

To correct any unphysical interactions between the VASPsol continuum solvent and the solid slab, we introduce a solvation correction scheme. We assume that the VASPsol model accurately reproduces all solvent-solvent and solvent-ion interactions, but fails to capture solvent-solid interactions as shown schematically in Figure 3-2b. To correct this error, we first remove the energy associated with the interaction of the continuum solvent and the solid by subtracting out the difference between the energy of the clean surface (solid "slab") in contact with vacuum $E_{\text{slab}}^{\text{vac}}$ and in contact with the continuum solvent $E_{\text{slab}}^{\text{vaspsol}}$, which we will refer to as $\Delta E_{\text{slab}}^{0} = E_{\text{slab}}^{\text{vaspol}} - E_{\text{slab}}^{\text{vac}}$. We then add back the interactions between the solvent and the slab by explicitly calculating the energy of adsorbing isolated water molecules within the continuum solvent, $\Delta E_{\text{slab}}^{\text{solv}} = E_{\text{H}_2\text{O, ads}}^{\text{vaspsol}} - \left(E_{\text{H}_2\text{O, ref}}^{\text{vaspsol}} - TS_{\text{H}_2\text{O, ref}}^{\text{exp.}}\right)$, for each adsorption site on the solid, where $S_{\text{H}_2\text{O, ref}}^{\text{exp.}}$ is the experimentally-measured entropy of bulk water. Note that we neglect the entropy of the adsorbed water as we assume that the interfacial water layer is relatively constrained and ice-like, significantly reducing its entropy relative to that of the bulk solution[141]. Having obtained this shift for each adsorption site, we can correct any calculation done with only the continuum solvent to capture the solid-solvent interactions potentially misrepresented by VASPsol.

For example, to calculate the energy $E_{\text{interface}}$ of a surface with N^{sites} identical adsorption sites, of which N^{ads} are occupied by some adsorbing ions and $N^{\text{sites}} - N^{\text{ads}}$ are filled by water, we calculate the energy of a periodic slab with explicit adsorbed ions (but not water molecules) within VASPsol to get $E_{\text{interface}}^{\text{vaspsol}}$. We then apply the solvation correction to get the true interface energy:

$$E_{\text{interface}} = E_{\text{interface}}^{\text{vaspsol}} - \Delta E_{\text{slab}}^{0} + \left(N^{\text{sites}} - N^{\text{ads}}\right) \Delta E_{\text{slab}}^{\text{solv}} \tag{3.1}$$

In the case where there are distinct adsorption sites, the energy of solvation $E_{\mathrm{slab}}^{\mathrm{solv}}$ becomes site specific. For FeS_2, we assume that the site-specific solvation energy is determined by the local chemistry, giving separate solvation energies for Fe and S sites on the surface. As it is impossible to adsorb H_2O simultaneously to adjacent Fe and S sites due to steric constraints, we take the lower energy of the Fe and S adsorption sites for each facet as the the facet-specific solvation energy $\Delta E_{\mathrm{slab}}^{\mathrm{solv}}$, and the density of these sites as the number of adsorption sites N^{sites}. Combining these terms, we obtain the solid-solvent interfacial energy term, with $N^{\mathrm{ads}} = 0$:

$$\left(G^{\mathrm{surface+solvent}} - G^{\mathrm{bulk}}\right) \approx E_{\mathrm{interface}}^{\mathrm{vaspsol}} - \Delta E_{\mathrm{slab}}^{0} + N^{\mathrm{sites}} \Delta E_{\mathrm{slab}}^{\mathrm{solv}} = E_{\mathrm{slab}}^{\mathrm{vac}} + N^{\mathrm{sites}} \Delta E_{\mathrm{slab}}^{\mathrm{solv}} \tag{3.2}$$

where $E_{\mathrm{interface}}^{\mathrm{vaspsol}} - \Delta E_{\mathrm{slab}}^{0}$ simplifies to $E_{\mathrm{slab}}^{\mathrm{vac}}$ in the case of zero adsorbed ions.

3.2.4 Charged adsorption

In order to obtain a full picture of interfacial stability across various solution conditions (here, pH levels), it is necessary to calculate the enthalpy of adsorption of all relevant ions (here, OH^- and H_3O^+) at infinite dilution, as discussed in the thermodynamic derivation earlier. To do so, it is necessary to ensure that in both the adsorbed and reference state, the charge state of the adsorbing ion is physical. Under periodic boundary conditions imposed by plane-wave DFT, the charge state can be set explicitly by removing a number of electrons from the system, and compensating the resulting charge with a homogeneous background. A more physical model is to include a counter-charge in the system and allow charge transfer from the cationic to the anionic species to occur self-consistently. However, in this case, it is important to take care to ensure that no unphysical electrostatic interactions between the anion, cation, and their periodic images contribute to the adsorption energy.

One approach to ensure that unphysical electrostatic interactions do not contribute to the adsorption energy is to construct a supercell large enough such that the electrostatic interactions between ions decay to a negligible level. A more computationally tractable approach is to choose a reference state such that the electrostatic interactions either cancel out between the adsorbed and reference states, or can be subtracted out analytically, giving an accurate enthalpy of adsorption at infinite dilution $\Delta h^{\mathrm{ads},\infty}_{\mathrm{H_3O^+}} = E^{\mathrm{ads}}_{\mathrm{H_3O^+}} - E^{\mathrm{ref}}_{\mathrm{H_3O^+}}$. One such choice of reference state is given in Figure 3-2c. In this setup, the nearest neighbor cation-cation and anion-anion image interactions cancel out between the adsorbed and reference state, leaving only the cation-anion interactions and ion-solid interactions. In both cases, the continuum solvent medium provided by VASPsol ensures rapid decay of the electrostatic interactions as a function of distance, such that even at a 5 Å minimum separation (with a VASPsol dielectric constant $\epsilon_r = 80$ for an aqueous system), electrostatic interactions between the ions are small enough that they can be subtracted out from the total energy as a post-calculation correction. If we assume that the ion-solid interaction in the reference state is small, which is reasonable considering that the solid is not charged and the separation between the ion and solid is over 10 Å, the only remaining interaction is the one we are interested in - the ion-solid interaction in the adsorbed state. Note that in this case, the ion charge state is self-consistently set to the correct value in both the adsorbed and reference configurations, as can be confirmed by a Bader charge analysis[142]. Relaxed adsorption geometries for H_3O^+ and OH^- derived using this approach for all facets of pyrite and marcasite can be found in Appendix D.

3.3 Interface thermodynamics

We first evaluate the relative energies of the various crystallographic facets in pyrite and marcasite and their tendency to adsorb OH^- and H_3O^+ ions, as given in Table 3.2 and illustrated in Figure 3-3. In pyrite, the (100) and (210) facets are dominant in the vacuum and solvated cases, in line with the common occurrence of these facets in natural cubic and pyritohedral habits of pyrite[143, 134]. In marcasite, we find that the spread of surface energies between different facets is smaller than in pyrite, with the (010), (101), (110), and (111) facets all having low energies, in agreement with

Phase	**Facet**	$\gamma^{vac}_{(hkl)}$ (J m^{-2})	$\gamma^{solv}_{(hkl)}$ (J m^{-2})	$\Delta E^{ads,\infty}_{H_3O^+} - \Delta E^{solv}_{slab}$ (eV/pH=0, 473K)	$\Delta E^{ads,\infty}_{OH^-} - \Delta E^{solv}_{slab}$ (eV/pH=0, 473K)
Pyrite	(100)	1.38	1.11	0.300	0.789
	(110)	2.14	1.26	0.757	0.206
	(111)	1.80	1.71	0.072	0.353
	(210)	1.82	1.07	0.899	0.299
Marcasite	(001)	1.70	1.45	0.215	0.210
	(010)	1.54	1.10	0.485	0.884
	(100)	2.12	†	†	†
	(011)	1.75	1.74	0.097	-0.246
	(101)	1.07	0.94	0.684	0.215
	(110)	1.68	1.19	0.471	-0.254
	(111)	1.67	1.21	0.443	-0.097

Table 3.2: Surface and adsorption energetics of FeS_2 in water. Calculated surface energies of various facets of pyrite and marcasite in vacuum ($\gamma^{vac}_{(hkl)}$) and in contact with pure non-dissociated water ($\gamma^{solv}_{(hkl)}$), as well as the calculated adsorption energy of H_3O^+ and OH^- at infinite dilution, with respect to the chemical potential of each ion in solution at pH = 0, 473K and a hydrated adsorption site. More precisely, $\Delta E^{ads,\infty} - \Delta E^{solv}_{slab}$ captures the strength of the adsorbate-solid interactions with respect to the free energy of the ion in solution and a hydrated solid surface, but does not include the contribution of adsorbate-adsorbate interactions or configurational entropy on the surface. † Omitted due to convergence issues on the hydration reference state.

their prevalence in natural marcasite crystals[134]. We then calculate the particle-averaged surface energy of each phase, which gives the total energetic contribution of the surface to the free energy of the solid (see Figure 3-3b). One way to verify the accuracy of the surface energy curve is through the experimentally-measured iso-electric point, which corresponds to a transition from a positively-charged (clean or H_3O^+-adsorbed) to a negatively-charged (OH^--adsorbed) surface. The onset of OH^- adsorption onto surface Fe sites in pyrite around pH=1, seen as the point at which the surface energy of pyrite begins to decrease, agrees well with the experimentally measured isoelectric point (IEP) in pyrite at pH=1.4 [123, 124]. Similarly, the absence of a maximum in surface energy in marcasite down to pH=0 suggests that some of the marcasite surfaces are always hydroxylated, even at very low pH, which agrees with the lack of an experimentally observed isoelectric point in marcasite within an experimentally accessible pH range[144]. In both cases, the agreement of the equilib-

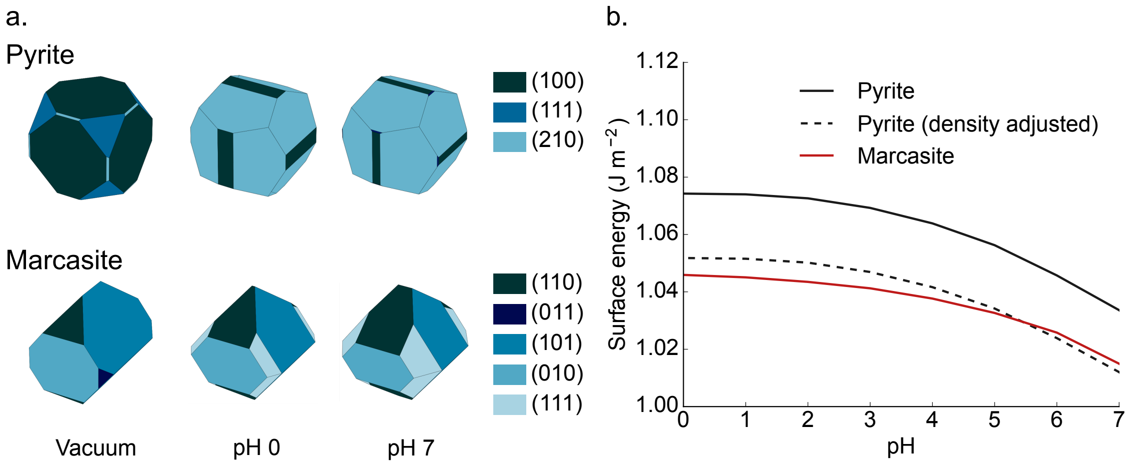

Figure 3-3: Surface energies of FeS_2 pyrite and marcasite. **a**. Equilibrium particle shapes (Wulff shapes) for pyrite and marcasite in vacuum and in solution at pH=0 and pH=7. **b**. Surface energies of pyrite and marcasite averaged over the equilibrium Wulff shape across a range of pH levels. The solid lines give the surface energy of pyrite and marcasite per unit area, while the dashed line gives $\overline{\gamma}_\mathrm{p}\left(\frac{\rho_\mathrm{m}}{\rho_\mathrm{p}}\right)^{2/3}$, the effective molar surface energy of pyrite scaled to account for the higher density of pyrite relative to that of marcasite. The density adjustment is necessary for a direct comparison of the effect of surface energy on stability as it accounts for the fact that the relevant free energy for determining the relative stability of pyrite and marcasite is the molar free energy. Thus, the surface energy of a pyrite particle with an equal mole number to that of a marcasite particle must be scaled down to account for the smaller size of the denser pyrite structure.

rium particle morphology and adsorption character of negative ions with experimental observations of the IEP indicates that the interface free energies of the low-energy facets in the OH^--adsorption regime are captured reasonably accurately.

From the particle-averaged surface energies given in Figure 3-3b, it is clear that while marcasite surfaces are more stable than that of pyrite under highly acidic conditions, a rapid onset of OH^- adsorption onto pyrite under more basic conditions stabilizes the pyrite surface. The origin of this transition lies in the variation in OH^- adsorption strength among the various facets of pyrite and marcasite - in pyrite, OH^- adsorbs onto the (210) facets covering the majority of the Wulff shape, while in marcasite, stabilization due to OH^- adsorption is initially limited to the otherwise unstable (110) and (111) facets.

3.4 Phase selection during synthesis

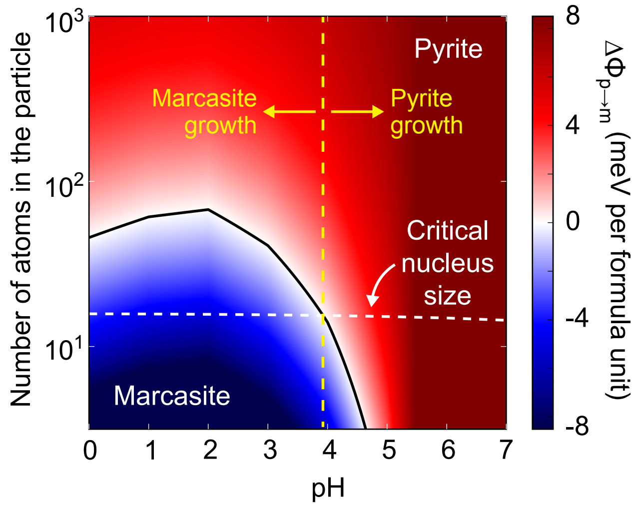

Figure 3-4: Thermodynamics of nanoscale FeS_2. The finite-size phase diagram of FeS_2 across a range of pH values, illustrating the low-particle-size, low-pH region of thermodynamic stability for marcasite. Note that we report a single critical nucleus size based on the experimentally reported supersaturation[115] for both pyrite and marcasite because the difference between the two is negligible.

The influence of surface energy on phase selection in FeS_2 synthesis can be viewed from both a thermodynamic and a kinetic standpoint. Combining the bulk and surface energy of pyrite and marcasite across all sizes and pH levels, we construct the size-pH phase diagram of FeS_2, given in Figure 3-4. We can immediately see that marcasite is the lowest-energy phase in acid at small particle sizes, giving rise to a driving force for the formation of marcasite under these conditions. At this stage of growth, the system is significantly influenced by nucleation kinetics, which we can analyze within the scope of classical nucleation theory.

As shown schematically in Figure 3-5, nucleation from solution proceeds over a nucleation barrier, which arises from the energetic penalty of forming a high-surface-area critical nucleus and scales as $\bar{\gamma}^3/g_{\mathrm{b}}^2$, where $\bar{\gamma}$ is the average surface energy of the nucleating phase, and g_{b} is the volumetric bulk driving force for precipitation [25]. The relative rates of pyrite and marcasite nucleation are exponential in the difference between their nucleation barriers, such that even a small decrease in surface energy

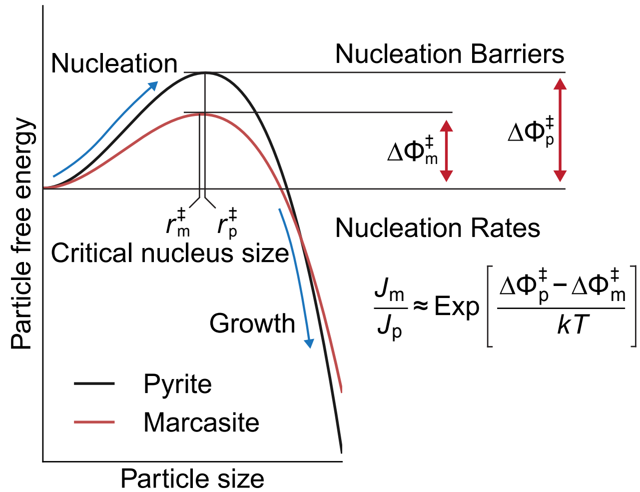

Figure 3-5: Relationship between finite-size energetics and nucleation kinetics. A schematic illustration of nucleation kinetics leading to the formation of metastable marcasite due to a lower kinetic barrier to nucleation $\Delta\Phi^{\ddagger}_{\mathrm{m}}$ and a correspondingly exponentially higher nucleation rate J_{m}, relative to that of pyrite ($\Delta\Phi^{\ddagger}_{\mathrm{p}}$ and J_{p} respectively)[25].

from pyrite to marcasite can lead to a large excess of marcasite nucleation. Taking the experimentally reported supersaturation for FeS_2 hydrothermal growth[115], we can immediately see that at the critical nucleus size, marcasite has a lower free energy than pyrite below pH=4, and thus nucleates exponentially faster. This transition to marcasite-dominant nucleation agrees with experimentally observed onset of marcasite formation between pH=4 and pH=6 [112, 115], and the absence of marcasite when FeS_2 is grown under more basic conditions. Thus, we can conclude that marcasite growth in acidic media may be explained by its finite-size thermodynamic stability and preferential nucleation under these conditions.

3.5 Generalizeability of the phase selection model

The agreement between the experimentally observed stabilization of marcasite in acid and our computational results lends significant credibility to the model of synthesis derived here. Considering that the energy scale of pH is small compared to typical energy scales involved in solid-state chemistry, the agreement of the transition point between pyrite and marcasite within 1-2 pH units is quite remarkable. We speculate that the primary reason underlying this result is the systematic cancellation of error between the chosen adsorbed and reference states. For example, we neglect dispersion interactions in our model due to computational constraints, despite the fact that they certainly play a significant role in determining the behavior of the real FeS_2-water interface. However, the error due to this necessary simplification likely cancels between the adsorbed and reference states of the ions, giving a sufficiently accurate estimate of the behavior of the system.

One other potential issue in the analysis presented here is the validity of the classical energy decomposition into bulk and surface terms to obtain the energy of the nucleus[25]. Accounting for the exact dynamics and free energies of the growing nucleus is extraordinarily difficult given any current computational or experimental method, and impractical given the goal of obtaining a scalable "synthesizability filter" for computational materials discovery. Instead, the semi-continuum analysis presented here aims to provide a first-order extrapolation of finite-size free energies from the bulk to the size scales relevant to nucleation. Of course, given the small energy scales involved, more detailed studies of the small-scale thermodynamics and nucleation kinetics in this system would help clarify the validity of the approximations made here, as well as identify any non-classical nucleation and growth behavior that may occur.

3.6 Conclusion

To summarize, I have demonstrated that pH–dependent phase selection in the hydrothermal growth of FeS_2 pyrite and marcasite can be rationalized through a quasi–thermodynamic analysis of nucleation and growth, accounting for the adsorption of "spectator ions" onto the nucleating particle. I developed a first–principles methodology for computing interfacial energies in aqueous media, accounting for the adsorption of charged ions. Using this method, I constructed a finite size phase diagram with the inclusion of any arbitrary set of "spectator ions" adsorbing on the solid surface. This phase diagram demonstrates that it is possible to quickly identify approximate solution conditions under which there may be a driving force for the formation of a target metastable phase, for example FeS_2 pyrite or marcasite. With this knowledge, one can quickly design syntheses that would allow the system to express the identified driving force, nucleating within the desired region of the phase diagram. Thus, I believe that both the general model proposed here, and the analysis of FeS_2 can serve as a useful thermodynamic baseline for predicting phase selection during synthesis, and as such, accelerate the realization of novel materials.

Chapter 4

Phase selection through off-stoichiometry - the case of MnO_2

In this chapter, I address the formation of off-stoichiometric intermediates as a handle for driving polymorph selection in the diverse class of MnO_2-framework structures. Specifically, I build on the benchmark of the SCAN functional for the *ab-initio* modeling of MnO_2 discussed in Chapter 2 to examine the effect of alkali-insertion, protonation, and hydration to derive the thermodynamic conditions favoring the formation of the most common MnO_2 phases - β, γ, R, α, δ, and λ - from aqueous solution. I explain the phase selection trends through the geometric and chemical compatibility of the alkali cations and the available phases, the interaction of water with the system, and the critical role of protons. This discussion offers both a quantitative synthesis roadmap for this important class of functional oxides, and a description of the various structural phase transformations that may occur in this system. Furthermore, I discuss the selectivity of off–stoichiometry as a handle for structure selection, contrasting the polytypic, large–tunnel todorokite phase to the more compact phases of MnO_2 which have more ordered crystal structures. Finally, I examine the interplay of off–stoichiometry and finite–size effects on the crystallization pathways of MnO_2 polymorphs from aqueous solution, demonstrating close agreement between the predictions made by the quasi–thermodynamic analysis and experimental results.

The content of this chapter is based, often verbatim, on four manuscripts which are published or in preparation for publication. In all cases, the work presented here consists of my contribution to the theoretical analysis, whereas the full details of the work can be found in the referenced publications:

- D. A. Kitchaev, S. T. Dacek†, W. Sun†, G. Ceder. "Thermodynamics of phase selection in MnO_2 framework structures through alkali intercalation and hydration." *J. Am. Chem. Soc.*, 139(7), 2672-2681 (2017)

- X. Hu†, D. A. Kitchaev†, L. Wu, Q. Meng, B. Zhang, A. Marschilok, E. S. Takeuchi, G. Ceder, Y. Zhu. "Revealing rich polytypism in todorokite MnO_2" [in preparation] (2017) (†equal contribution)

- P. Selvarasu†, D. A. Kitchaev†, J. Mangum, L. T. Schelhas, J. Perkins, K. Shun-Gilmour, B. Gorman, M. Toney, G. Ceder, D. Ginley, and L. Garten. "Phase selection in the aqueous growth of Mn^{3+} oxides." [in preparation] (2017) (†equal contribution)

- B-R. Chen†, W. Sun†, D. A. Kitchaev, J. S. Mangum, V. Thampy, L. M. Garten, D. G. Ginley, B. P. Gorman, K. H. Stone, G. Ceder, M. F. Toney, L. T. Schelhas. "Understanding crystallization pathways leading to manganese oxide polymorph formation" [submitted] (2017)

4.1 The MnO_2 family of compounds

The diverse modifications of MnO_2, formed through a variety of off-stoichiometric intermediates, have been widely studied as Li-ion battery cathodes[145, 146], photocatalysts[147, 148], molecular sieves[149], supercapacitors[150], and pigments[46], where each application requires a specific MnO_2 structural polymorph[53] or structural motif in the case of nanocrystalline manganese oxides[147]. Despite an abundance of literature reporting synthesis recipes for each MnO_2 polymorph and documenting the transformations between them, the understanding of the underlying driving forces is sparse.

This gap in the present knowledge of the manganese oxide system makes it difficult to separate kinetic effects from thermodynamics in any mechanistic analysis of MnO_2 formation, or to make quantitative predictions regarding phase transformations, which limit both the scientific understanding of manganese dioxide chemistry and the design of functional MnO_2-based materials.

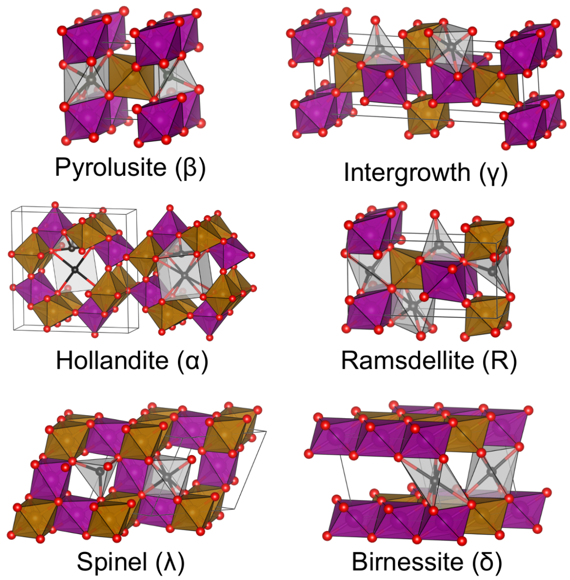

Figure 4-1: Common polymorphs of MnO_2 and predicted sites for alkali intercalation. The purple and yellow spheres and surrounding octahedra denote spin-up and spin-down Mn atoms and MnO_6 octahedra[151], while the black spheres and surrounding grey polyhedra denote potential intercalation sites for alkali and alkali-earth ions in the structure. Each site shown defines a distinct sublattice - while a single site of each type is shown, all equivalent sites are included in the structural enumeration. Note that for the birnessite (δ) phase we consider the monoclinic O1-stacked (P$\overline{3}$m1) and O3-stacked (R$\overline{3}$m)(shown) configurations as competing configurations of the same phase[152]. Furthermore, while the γ phase generally refers to a range of intergrowth structures with a varying fraction of β-like and R-like domains, we choose a representative structure with 50% β-type tunnels for the purposes of all calculations.

The most common structures accessible by aqueous synthesis in the manganese dioxide system are the rutile-type β phase, hollandite-type α, ramsdellite-type R, birnessite-type δ, spinel-type λ, and γ, which is an intergrowth of β and R with various fractions of β/R domains and twinning[151, 153]. These six structures are shown in Figure 4-1, which illustrates their overall framework, as well as their approximate low temperature magnetic configuration and predicted interstitial sites. Importantly, we consider a single prototypical γ structure that is a 50% mixture of β and R domains, as a model of the general class of such intergrowth phases[49, 153]. All of these structures consist of corner- and edge- sharing MnO_6 octahedra which pack to form a hexagonal-close-packed (HCP) oxygen sublattice in the case of β, α, R, γ, and O1-stacked δ[152], or a face-centered-cubic (FCC) oxygen sublattice in the case of λ and O3-stacked δ[152]. In terms of their magnetic structure, all MnO_2 polymorphs are well-represented as relatively simple antiferromagnets[65, 61, 60, 151], although the true magnetic structure of certain polymorphs is more complex[83, 63]. The packings of MnO_6 octahedra create a variety of voids that form sublattices of structurally equivalent interstitial sites, which allow the intercalation of cations and water into the MnO_2 frameworks.

Given the diverse applications of MnO_2 polymorphs, there are a number of established synthesis methods that yield phase-pure forms of each structure[50, 154, 78, 155, 156, 157, 53]. The β, α, R, λ, and δ forms can be made hydrothermally from an aqueous solution containing Mn^{2+} or $MnO_4{}^-$, as well as some alkali or alkali-earth cations. The γ phase, also known as "electrolytic manganese oxide" (EMD), is a common product in high-rate electrochemical deposition, typically from an aqueous solution of $MnSO_4$ and H_2SO_4, although this phase can also be made hydrothermally as "chemical manganese oxide" (CMD)[158, 159, 153]. While the synthesized products often contain significant amounts of intercalated alkali or alkali-earth cations, protons, and/or water, mild post-processing of the as-synthesized product can yield stoichiometrically pure forms of the various MnO_2 polymorphs without any intercalated ions[50, 78, 155, 160]. In other cases however, the extraction of intercalants from the MnO_2 framework induces phase transformations, suggesting that the cations play a key role in kinetically or thermodynamically stabilizing the polymorphs during initial phase selection[155, 161], consistent with the results of several *in-situ* studies[162, 163]. These results motivate our work on establishing a thermodynamic baseline for the stability of off-stoichiometric intercalated MnO_2-type phases, both for distinguishing thermodynamic and kinetics effects, and for guiding the targeted synthesis of MnO_2 structures through off-stoichiometric intermediates.

Previous work on characterizing the thermodynamics of the alkali-containing manganese oxides has yielded partial data on the nature of the driving forces governing phase selection. Calorimetry on several naturally occurring MnO_2-framework type minerals[48, 164] gave an early indication of the critical importance of alkali cations in the thermodynamic stabilization of a number of MnO_2 frameworks. Subsequent computational work has reproduced several of these pathways. For example, based on a density functional theory (DFT) analysis, Reed *et. al.* report the destabilization of δ-MnO_2 with respect to λ under Li^+ intercalation[165], Balachandran *et. al.* identify the importance of structural water in stabilizing R over β[56], Cockayne *et. al.* and Wei *et. al* study the stabilization of α and δ with respect to β by dilute K^+ intercalation and hydration[58, 166], Tompsett *et. al.* and Wang *et. al.* model the destabilization of the α and β frameworks respectively under Li^+ intercalation [167, 168], while Ling *et. al.* calculate the conversion α to λ on Mg^{2+} insertion[169]. In a recent work, Li *et. al.* computationally hypothesize a number of possible mechanisms for the transformation from δ to the β, R, α, and related tunnel structures. In all cases, computational work has been limited to a subset of MnO_2 phases and alkali-ions, typically focusing on fixed-composition or single-phase (topotactic) reactions. While these data give insight into a subset of possible reactions in the manganese dioxide system, an analysis of MnO_2 synthesis pathways requires a grand-potential approach that considers all possible phases and compositions. Previously, such an analysis was not possible as existing *ab-initio* methods failed to give accurate results for the relative energetics of MnO_2 polymorphs[151]. The recent resolution of these methodological difficulties through the SCAN exchange-correlation functional[11, 151] enables us to establish a consistent model of alkali-MnO_2 thermodynamics across all phases and compositions.

In this work, we construct a comprehensive thermodynamic baseline for the common polymorphs of MnO_2 in an aqueous environment, accounting for the effect of water, as well as H^+, Li^+, Na^+, K^+, Mg^{2+}, and Ca^{2+} ions. Importantly, we consider all MnO_2-derived phases across all dry and hydrated ternary compositions to offer a reliable energetic ranking of MnO_2 polymorphs across a variety of stoichiometries. In addition to establishing thermodynamic boundary conditions for the aqueous synthesis of MnO_2 structures, our data yield a full set of potential "energetically downhill" phase transformations in the system, which are critical data for the prediction of transformation pathways between the polymorphs under non-equilibrium conditions, the evaluation of classical and non-classical nucleation pathways[170], and the interpretation of *in-situ* data. Finally, our analysis reveals the evolution of the driving force for phase transformation upon the extraction or insertion of cations, which is of interest for estimating the feasibility of topotactic reactions in this space.

More generally, the MnO_2 system, whose diverse polymorphism arises from an array of intercalation redox reactions that allow each phase to accommodate significant off-stoichiometry, is an ideal model system to analyze the coupling between redox activity in transition metal ceramics and the diversity of their structures. As we discuss here, the types of intercalation sites created by each transition-metal framework determine which structures can be synthesized in the presence of alkali and alkali-earth ions of varying size and valency, as well as water. As such, we establish alkali intercalation as a predictive synthesis handle analogous to prior work on structure selection by surface stability[122, 21, 89], advancing the field of predictive synthesis and materials design.

4.2 Formalism and computational methods

To approach the problem of accessing the thermodynamics of the β, γ, R, α, δ, and λ -MnO_2 phases in the presence of alkali intercalation and hydration, we must define a chemical space of interest, determine the structure of all phases across the chemical space, and compare their energetics to that of all competing phases within a grand potential that is representative of the aqueous solutions used in synthesis. Formally, this grand potential can be written as

$$\psi = g_b - n_A\mu_A + n_e e\phi$$

where g_b is the molar bulk Gibbs free energy of formation. This potential accounts for the incorporation of n_A external ions at a chemical potential of μ_A into the growing phase, and the associated transfer of n_e electrons at an external potential of ϕ. This potential ψ defines the phases of $A_xMnO_2 \cdot yH_2O$ stable under solution conditions defined by a combination of μ_A and ϕ, yielding the space of phases which may be bulk–stable in the various possible hydrothermal synthesis media.

The chemical space we consider are the compounds with the formula $A_xMnO_2 \cdot yH_2O$ for A = H, Li, Na, Ca, Mg, Ca, $0 \leq x \leq 1$, $0 \leq y \leq 1$, based on the range of intercalation and hydration reported experimentally[48, 19]. Within this range, we determine the structure of each of the β, γ, R, α, δ, and λ phases by placing the intercalant cations and/or water in the interstitial sites available in each phase, and choosing the lowest energy structure. Furthermore, we map all $A_xMnO_2 \cdot yH_2O$ phases reported in the Inorganic Crystal Structure Database (ICSD)[14] and the Materials Project[14] to the β, γ, R, α, δ, and λ polymorphs through a distortion-tolerant affine map[96], or consider them as a competing phase in cases where the underlying MnO_2 framework does not correspond to any of the six polymorphs in question. Through this procedure, we capture all experimentally reported structures, and predict likely low-energy structures within each MnO_2 phase, giving a reliable sample of the configuration space of $A_xMnO_2 \cdot yH_2O$ compounds.

To obtain accurate energetics for each $A_xMnO_2 \cdot yH_2O$ structure, we follow the methodology recently established to yield accurate energetics for MnO_2 polymorphs[151]. We perform all DFT calculations within the Vienna Ab-Initio Simulation Package (VASP)[5, 6] with projector-augmented wave (PAW) pseudopotentials[8], a reciprocal space discretization of at least 25 Å^{-1}, and the SCAN meta-GGA exchange-correlation functional[11]. To balance computational efficiency with accuracy, we pre-relax all structures using a Γ-point-only calculation, followed by a pair of full k-point relaxations converged to $2 * 10^{-7}$ eV/atom on the electronic structure, and a maximum force of 0.02 eV/Å on all atoms. As the magnetic structure of the Mn sublattice plays a significant role in determining the relative stabilities of MnO_2 polymorphs, we initialize all magnetic configurations using the ground state antiferromagnetic (AFM) orderings given by Kitchaev *et. al.*[151] for structures topotactic to the MnO_2 polymorphs given, or a pair of representative AFM and ferromagnetic (FM) orderings in other cases. To allow for symmetry-breaking relaxations, we do not enforce any symmetry constraints in our calculations. This calculation scheme provides an acceptable balance between accuracy and computational efficiency, although it must be noted that more detailed enumeration and specialized functionals may be needed to reproduce the complex magnetic and charge orderings that arise in some of these phases[171].

For all structures with alkali and alkali-earth inserted cations, the presence of relatively strong orderings in unhydrated A_xMnO_2 structures limits the contribution of configurational entropy as compared to the enthalpy differences between competing structures. As a result, we can approximate the relative Gibbs free energies of the A_xMnO_2 structures by their DFT-derived T = 0 K enthalpies. In the case of proton insertion, this assumption is not necessarily valid, as the interactions between protons in the structure may be insufficient to limit their configurational entropy, and we find that the enthalpy differences between H_xMnO_2 structures are small enough to be competitive with entropic effects. Similarly, the phonon modes associated with the vibrationally-active O-H bonds may significantly contribute to the free energies of protonated MnO_2 structures at room temperature. To account for these effects, we bound the contribution of protons to the configurational entropy by that of an ideal lattice solution, based on the lattice defined by protons in the relatively well-ordered MnOOH structures. Furthermore, we calculate the zero-point energy and phonon entropy of all low-enthalpy H_xMnO_2 structures[172]. Put together, the DFT-derived enthalpy, zero-point energy, configurational entropy, and vibrational entropy yield the relative Gibbs free energies of H_xMnO_2 phases. Finally, in the case of hydrated structures, the DFT-calculated formation energy of $A_xMnO_2 \cdot yH_2O$ from bulk water and A_xMnO_2 formally corresponds to the enthalpy of hydration. Although the entropy of the hydration reaction is difficult to calculate exactly, we place a bound on its magnitude by assuming that the intercalated water has an entropy that is no higher than that of bulk water. While a significant simplification, this bound is sufficient to establish the key effects of hydration on MnO_2 thermodynamics.

Based on the calculated energetics, we derive the intercalation phase diagram of each MnO_2 polymorph by constructing the convex hull of all topotactically-related structures. Combining these convex hulls, we construct the open-system phase diagrams, which map the equilibrium phases as a function of pH and alkali chemical potential. In the case of phase diagrams given as a function of composition, we calculate formation energies with respect to pure β-MnO_2, the ground state $AMnO_2$ structure, and liquid water at 298 K. In the case of open systems, the zero of alkali chemical potential is chosen as that of the ion at a 1 molal concentration in water at 298 K and pH=0 at zero applied potential, which we calculate as the DFT formation energy of the elemental reference plus the experimentally-measured formation energy of the alkali ion in water[106]. Finally, to partially counteract the effect of self-interaction in the Mn d-states, we apply to a constant potential shift equal to 0.337 V to all calculated structures so as to reproduce the experimental formation energy of β-MnO_2 with respect to Mn and O_2 gas in the open-system phase diagrams. This correction serves a similar purpose to the SCAN oxidation potential correction derived in chapter 2, which was not available at the time this work was completed. Finally, we use experimentally-reported equilibria to set the energy of the hausmannite Mn_3O_4 structure[173, 174]. While we must introduce a trade-off between redox potential accuracy and structure prediction accuracy in choosing to use SCAN instead of the more common Hubbard-U approach[106, 175], we find our aqueous stability results to be accurate within 2 pH units[173], which is acceptable for evaluating the structure selection trends we are interested in.

4.2.1 Generation of A_xMnO_2 intercalated structures

To generate suitable candidate intercalation structures across A_xMnO_2 compositions, we first identify sublattices of structurally equivalent interstitial sites in β, α, R, γ, δ, and λ -MnO_2. Representative sites for each sublattice are shown in Figure 4-1. Note that in addition to reproducing previously cited sites in each structure (octahedral site in β [168]; octahedral and tetrahedral sites in γ and R[155]; 2a, 2b, 8h and 8h' Wyckoff sites in α[167]; octahedral sites in δ[152, 160]; octahedral and tetrahedral sites in λ [145]), we identify several additional candidate sites that help diversify our initial structure dataset. In the case of hydrogen intercalation, we displace all predicted interstitial sites until they are at 1 Å of the nearest oxygens to account for the fact that H is typically found as part of an OH^- group. Of these potential OH^- groups, in order to identify the likely stable candidates, we consider those occupying the most electrostatically favorable positions. Based on the generated sublattices of structurally equivalent sites, we proceed to generate orderings for A_xMnO_2 on each sublattice. An important consequence of this approach is that we only consider the occupancy of a single type of site at a time - for example, in the spinel-type λ-MnO_2, for x $\leq$ 0.5, we do not consider simultaneous octahedral and tetrahedral occupancy, and for x $>$ 0.5, we only consider octahedral sites. To keep the number of calculations tractable, we only consider a single ordering for each sublattice and each composition, chosen as the electrostatically most favorable alkali-vacancy configuration.

4.2.2 Generation of hydrated A_xMnO_2 configurations

In order to account for the possibility of water intercalation into the A_xMnO_2 compounds, we proceed to calculate the formation energy of $A_xMnO_2 \cdot yH_2O$ structures. As we are only interested in the effect of bulk hydration on the relative stability of the chosen MnO_2 polymorphs, we only consider the effect of hydration on ground state A_xMnO_2 structures. In other words, we only consider hydration to the extent that it stabilizes the ground states of each polymorph with respect to that of other polymorphs, rather than capturing the coupled effects of water and alkali ions on the structure of various MnO_2 frameworks. To this end, for the ground state A_xMnO_2 structures of each MnO_2 polymorph, we calculate the DFT formation energy of topotactically-related $A_xMnO_2 \cdot yH_2O$ structures. Based on the number of interstitial sites available in each of the A_xMnO_2 structures capable of accommodating a water molecule, and experimentally reported hydration levels [48, 19] we restrict our enumeration to y = z/8 for some integer z, with y $\leq$ 1/2 - x in the case of β, α, R, γ, and λ, and y $\leq$ 1 - x in the case of δ.

To generate $A_xMnO_2 \cdot yH_2O$ structures, we employ a heuristic method. As our objective is to obtain a realistic configuration of water molecules obeying basic electrostatic considerations, we divide the water insertion procedure into four steps. First, we find all coordinates in the structure lying at a distance of at least 2 Å (twice the water O-H bond length) from any atom. In the case of β, R, and γ, we reduce this cutoff to 1.8 Å to allow for the intercalation of water into the small tunnels. We then generate the most electrostatically favorable arrangement of O^{2-} ions within these coordinates, where each oxygen is a placeholder for a water molecule. Finally, we determine the electrostatically optimal positions of hydrogen atoms under the constraint that each O^{2-} specie is coordinated by two hydrogens at a 1Å bond length. Initializing from this configuration, we proceed with the same DFT calculation methodology as with A_xMnO_2 structures, converging the structure to 2 * 10^{-7} eV/atom on energy, but forego the convergence on forces for reasons of limited computational resources.

4.2.3 Generation of Ruetschi defects

An alternative form of water incorporation into MnO_2 frameworks is through the formation of Ruetschi defects[176, 177], which consist of a Mn^{4+} vacancy, compensated by four localized H^+ ions. The resulting structure can be written as $Mn_{1-y}H_{4y}O_2$ or (1-y)$MnO_2 \cdot 2yH_2O$, where y corresponds to the Ruetschi defect concentration. We calculate the formation energies of dilute Ruetschi defects in pure β, α, R, γ, δ and λMnO_2. To do so, we generate all possible symmetrically distinct Mn^{4+} vacancies within a $Mn_{16}O_{32}$ supercell of each phase, chosen to maximize the nearest-neighbor distance between Ruetschi defects in the calculated structures. For each vacancy, we then calculate the formation energy of all symmetrically distinct arrangements of four protons within the vacant MnO_6 octahedron.

4.3 Thermodynamics of off-stoichiometric MnO_2

We begin by evaluating the thermodynamics of alkali and alkali-earth intercalation into MnO_2 structures in a dry environment in order to establish the baseline effect of cation type and concentration on the stability of β, α, R, γ, δ, and λMnO_2 phases. For each of A = Li, Na, K, Mg, and Ca, the formation energy of each polymorph at concentration A_xMnO_2 with respect to phase separation between β-MnO_2 and the ground state $AMnO_2$ structure is given in Figure 4-2 (this choice of reference state is arbitrary and only serves to clearly present the data here). The solid squares and lines denote the ground states within a constrained MnO_2 framework, i.e. the behavior for the topotactic insertion of A. The grey dashed line denotes the energy of the global equilibrium ground state configuration of A_xMnO_2, without any constraints on the MnO_2 sublattice. As such, the curves in Figure 4-2 give not only the equilibrium configuration of A_xMnO_2 polymorphs at each composition, but also the driving force for phase transformation between each pair of polymorphs, or other phases non explicitly considered. For example, in the case of Na_xMnO_2, all ground state configurations are commensurate with the MnO_2 polymorphs we consider, while in the case of Ca_xMnO_2, other ICSD-reported structures arise as the ground state across a limited composition range, even along the A_xMnO_2 composition line. With alkali insertion, the lowest energy polymorph changes frequently, and different inserting ions can stabilize different polymorphs, creating a clear opportunity for polymorph selection through the controlled addition of group I or II elements during synthesis.

We proceed from the baseline energetics of the dry A_xMnO_2 structures to consider

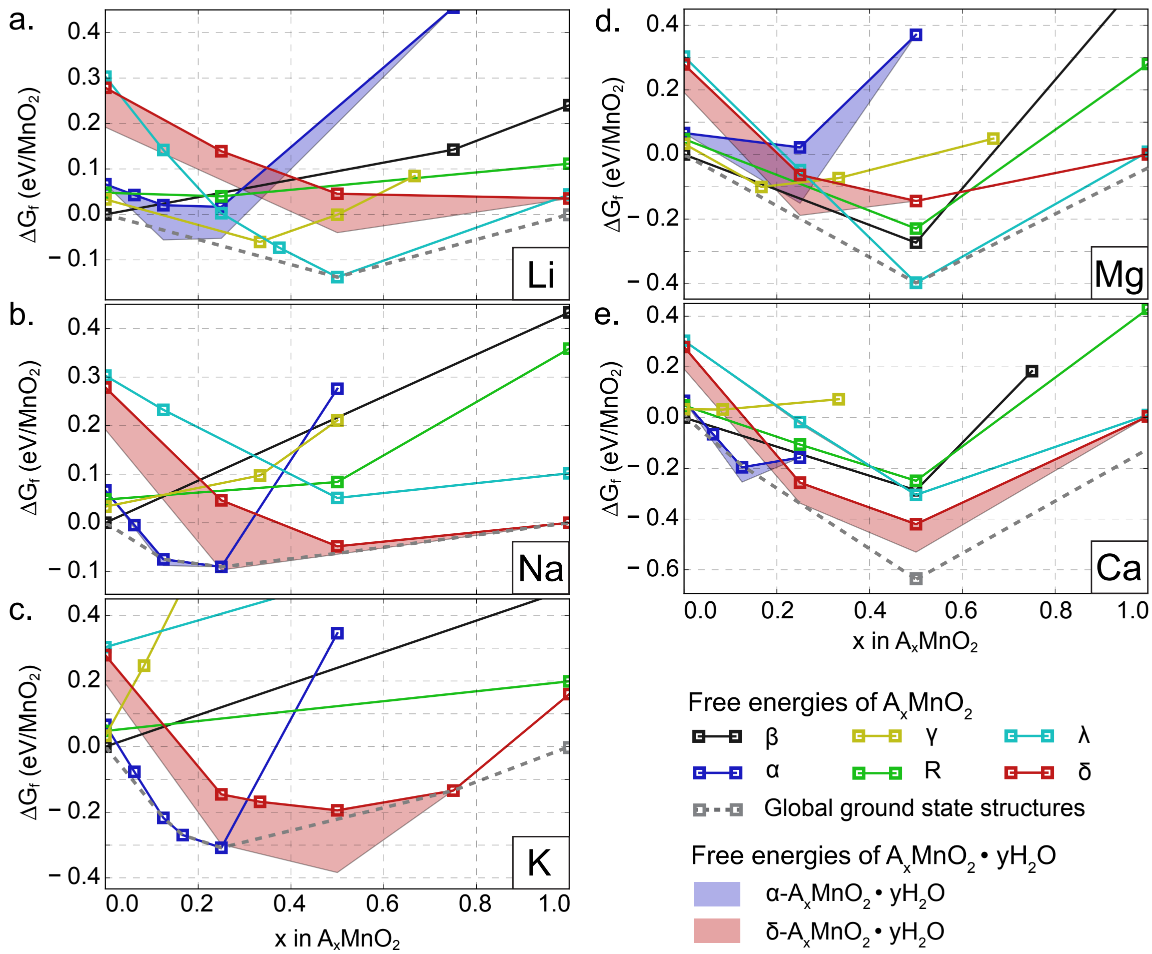

Figure 4-2: Computed formation free energies of the β, α, R, γ, λ and δMnO_2 polymorphs intercalated with **a.** Li^+, **b.** Na^+, **c.** K^+, **d.** Mg^{2+}, or **e.** Ca^{2+} cations. The energy is given with respect to a linear combination of β-MnO_2 and the most stable $AMnO_2$. The solid markers correspond to the ground state structures for a given MnO_2 framework as a function of composition. The dotted line illustrates the global thermodynamic equilibrium along this same composition line, without the restriction that the MnO_2 framework remain topotactic. Finally, the shaded regions depict the range of free energies of each phase that could be expected from hydration, with the lower bound corresponding to equilibrium with pure water at 298K, assuming that the intercalated water has bulk-like entropy. While all phases were hydrated, only the α and δ phases admitted stable hydrated configurations. Note that the $AMnO_2$ phases for A = Mg, Ca favor the δ phase among the MnO_2 frameworks considered here, but are globally unstable with respect to phase separation into MnO and AO rocksalts.

the effect of hydration on the formation energy of each MnO_2 polymorph. The shaded regions below the equilibrium lines of the α and δ phases in Figure 4-2 denote the likely range of formation energies for hydrated $A_xMnO_2 \cdot yH_2O$ structures, with the uncertainty in the exact value arising from the fact that we are unable to reliably calculate the entropy of intercalated water, and instead simply bound the entropy by that of bulk water. Note that while we calculate the hydration energy of all polymorphs, only the α and δ phases yield hydrated configurations energetically favorable with respect to the dry A_xMnO_2 structure and bulk water at 298K. As a result, we do not plot the hydration energies of the β, R, γ or λ structures.

Finally, we evaluate the effect of proton incorporation, where we classify protons by whether or not they lead to the reduction of Mn from 4+ to 3+. Following previous work by Ruetschi *et. al.*[176], we term protons which intercalate into the structure and reduce Mn as Coleman protons[178], and those which compensate Mn vacancies and are not involved in redox reactions as Ruetschi protons[176, 177].

The formation energy of Coleman protons, whose thermodynamics are shown in Figure 4-3a, can be represented analogously to the larger alkali ions as their formation is a type of intercalation reaction. However, as protonated structures form vibrationally-active O-H bonds, we also consider the effects of zero-point energy and phonon free energy. Furthermore, as this type of proton is highly mobile [177], we must account for the contribution of configurational entropy to the formation energy. Thus, in Figure 4-3a, the solid lines correspond to the Gibbs free energy of formation along the H_xMnO_2 composition line at 298K, estimated from the sum of the DFT-derived enthalpy of formation, the zero point energy, vibrational free energy, and configurational entropy. More detailed free energy curves of MnO_2 and MnOOH structures are available in Appendix F. Interestingly, we find the contribution of zero-point energy and vibrational free energy to the relative stability of MnO_2 polymorphs is minimal. This result is likely due to the fact that the local bonding environment in all phases is very similar, making finite temperature vibrational effects a weak handle for polymorph selection.

In contrast to Coleman protons, which can be thermodynamically stabilized by controlling the external chemical potential of H^+, Ruetschi protons are equivalent to structural water and are independent of pH, at least at equilibrium. Thus, the formation energies of Ruetschi protons, shown in Figure 4-3b for each polymorph with respect to β-MnO_2 and bulk water at 298K, follow the thermodynamics of isolated point defects. Ruetschi protons exist as localized clusters of four OH^- groups at the site of a Mn^{4+} vacancy, and as such are electrostatically neutral away from the immediate environment of the Ruetschi defect and largely immobile at lower temperatures[177]. As a result, we assume their configurational entropy to be given by the formation entropy of the initial Mn^{4+} vacancy, and the defects to be non-interacting within the 0-10% concentration range shown in Figure 4-3b. Furthermore, we assume that the effect of O-H vibration within the Ruetschi defects is largely independent of the surrounding structure, affecting their stability versus water but not their relative stability within the various MnO_2 polymorphs. Put together, we find Ruetschi defect formation to be unfavorable at any significant concentration in all MnO_2 structures, but less so in the R and γ phases than β.

In real protonated manganese dioxide structures, both Coleman and Ruetschi protons are reported to be present[176, 179], such that their effect on the formation energy must be considered in tandem. Assuming that the effects of Coleman and Ruetschi protons are approximately independent, we calculate the stability of MnO_2 frameworks across $MnH_{4x+y}O_{2+2x}$ compositions, where x denotes the concentration of Ruetschi defects and y denotes the concentration of Coleman protons. The resulting stability map, given in Figure 4-3c, reveals that the balance between overall proton content, and the degree to which protons reduce Mn^{4+} determines the relative stability of the β, R, and γMnO_2 frameworks. While Ruetschi defects, requiring a high activity of H_2O, stabilize the γ phase, the combination of high water content and high acidity, leading to Coleman protons, should help the formation of ramsdellite. Indeed, both the γ and ramsdellite phases are typically grown by plating out of aqueous solution with high acidity[158]

Finally, as our primary goal is the control over MnO_2 framework structure during

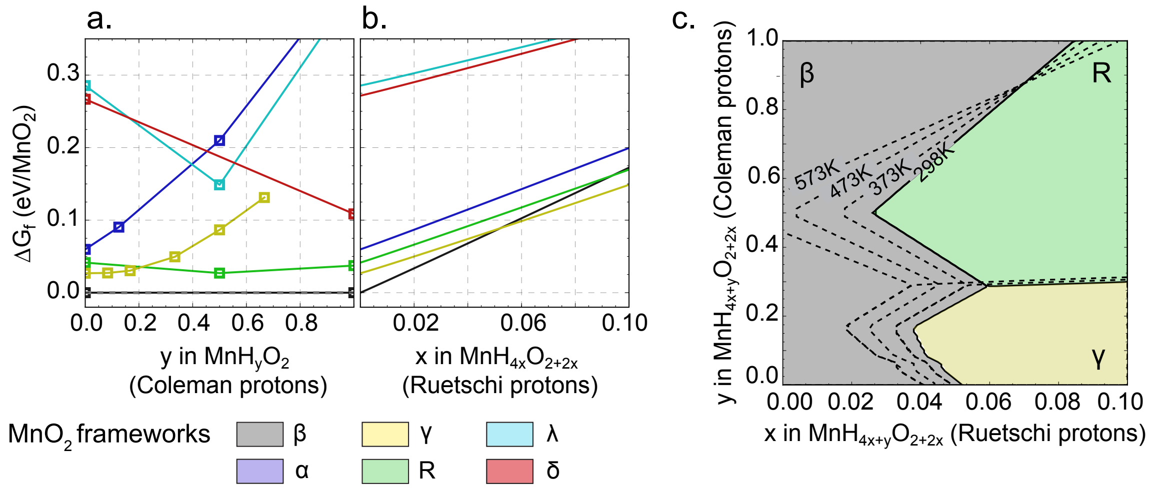

Figure 4-3: Thermodynamics of proton incorporation into MnO_2 polymorphs, as **a.** reducing (Coleman) protons, and **b.** non-reducing (Ruetschi) protons. In **a.** and **b.**, the solid lines indicate the formation free energy at each proton concentration with respect to the β-type pyrolusite-magnetite equilibrium line (**a.**) or β-MnO_2 and water (**b.**). All formation energies are given at 298K, accounting for the effect of DFT-derived formation enthalpy, zero-point energy, vibrational free energy, and configurational entropy. **c.** The combined effect of Coleman and Ruetschi protons on stabilizing R- and $\gamma-MnO_2$ with respect to β, assuming that their effect on the free energy of $MnH_{4x+y}O_{2+2x}$ is independent.

aqueous synthesis, we evaluate the stability of all A_xMnO_2 ground states across a range of solution conditions. Combining the thermodynamic equilibria data given in Figure 4-2 and Figure 4-3a, we construct the open-system aqueous phase diagrams for each A_xMnO_2 system, shown in Figure 4-4. A list of all reactions we consider in this stability map is available in Appendix E. To illustrate the effect of hydration on these phase diagrams, we separate the stability regions of unhydrated A_xMnO_2 phases and those of the hydrated α and δ phases. Since we find Ruetschi defects to be unstable with respect to dehydration, we do not include them in these grand-potential equilibrium phase diagrams. inally, we do not include co-intercalated structures, or alkali-rich structures such as the alkali manganates with the formula A_xMnO_{2+y} as they fall outside the scope of the structural and chemical space we are considering, although outside of mild aqueous conditions, in particular at high alkali potentials and in oxidizing environments, these structures do become stable. The aqueous phase diagrams shown in Figure 4-4 show both the equilibrium compositions of A_xMnO_2

that could be expected to form under various conditions of pH and alkali chemical potential, and the underlying MnO_2 framework, offering a direct comparison to aqueous precipitation experiments reported as synthesis routes for MnO_2 polymorphs. Similarly, these data elucidate the effect of changing solution pH and chemical potential on alkali stability within MnO_2 frameworks, giving a quantitative map for the acid-induced chemical extraction of alkali ions from MnO_2 frameworks, and the corresponding phase transformations[157].

4.4 Off-stoichiometry and MnO_2 phase selection

4.4.1 Alkali-stabilized phases: α, λ, and δ

The first conclusion we are able to draw from our analysis is that the α, λ, and δ frameworks, while not the ground states for the MnO_2 composition, are thermodynamically stabilized by alkali intercalation, meaning that control over the product MnO_2 framework can be achieved by controlling the chemical potential of alkali cations in the precursor solution. Specifically, Li^+ and Mg^{2+} favor the spinel (λ) phase, Na^+, Ca^{2+}, and especially K^+ favor the hollandite (α) phase, and all cations except Li^+ favor the layered (δ) phase in some composition range. During hydrothermal growth, these cations are typically present in the growth solution either from a $MnO_4{}^-$ precursor salt, or as a deliberate additive (typically, as an alkali hydroxide salt). As a result, the primary handle over alkali chemical potential is the initial salt concentration, leading to β, α, λ, or δ-type A_xMnO_2 growth. This result is consistent with a number of reported transitions between MnO_2 frameworks. For example, several experimental studies report a transition from β to α to δ on increasing the K^+ content in the precursor solution, and the reverse transformation with decreasing pH[156, 182, 157, 183, 184]. These observations are in qualitative agreement with the phase diagram shown in Figure 4-4c, although it is difficult to compare the results quantitatively as the authors do not maintain a consistent K^+ concentration in the solution throughout the synthesis, or consistently report the pH for their reactions.

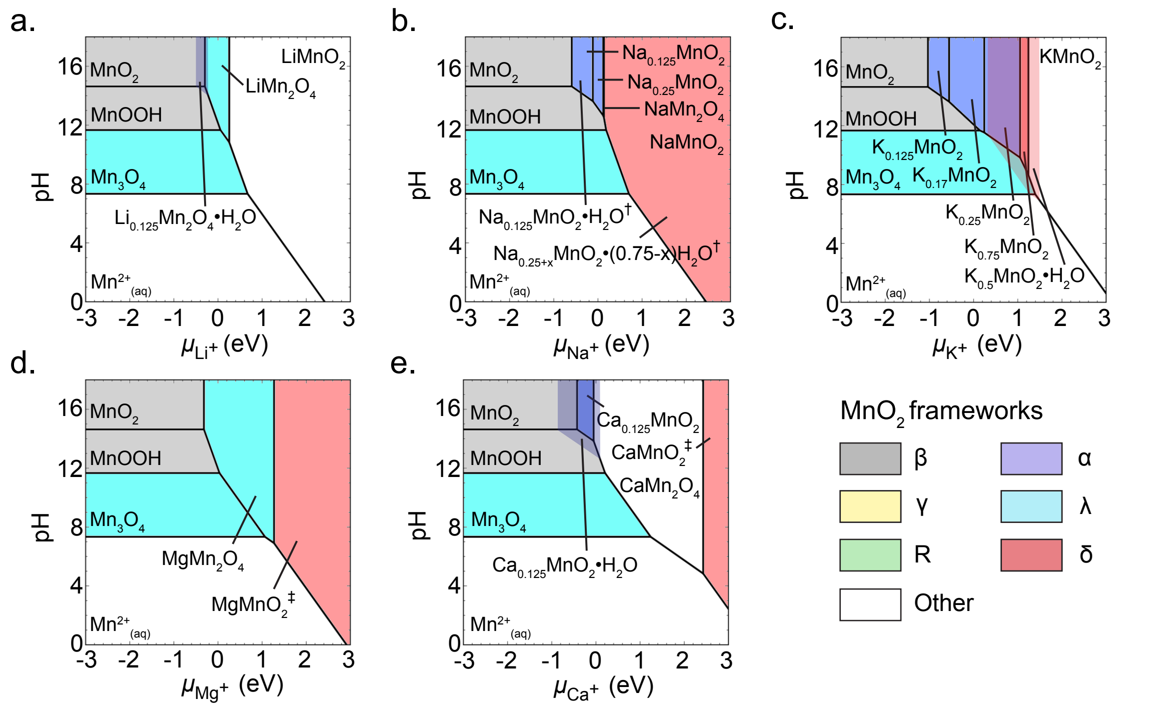

Figure 4-4: Constrained equilibrium thermodynamics driving phase selection between MnO_2 polymorphs as a function of solution conditions at 298K and zero applied potential, for solutions containing **a.** Li^+, **b.** Na^+, **c.** K^+, **d.** Mg^{2+}, or **e.** Ca^{2+} cations. The zero of the alkali-ion chemical potential corresponds to the chemical potential of the ion in an aqueous solution at a 1 molal concentration. The bixbyite Mn_2O_3 phase does not appear here as we find it to be unstable with respect to MnOOH up to 231 °C, in close agreement with TGA experiments[180] and recent DFT results[175], but in conflict with older results[181]. Hydrated configurations from Figure 4-2 are included as lightly shaded regions demonstrating the relative stability of hydrated phases but not the precise hydrated composition, which we do not resolve in this study. The set of reactions considered in these phase diagrams are available in Appendix E. In particular, we do not include the A_xMnO_{2+y} manganate phases which would appear under oxidizing conditions as they fall outside the scope of our analysis, or the alkali oxides and hydroxides which would appear at high alkali potential. † The hydrated α and δ regions align almost exactly with the non-hydrated regions and are not shown for clarity. ‡ The $AMnO_2$ phases for A = Mg, Ca favor the δ phase among the MnO_2 frameworks considered here, but are unstable with respect to phase separation into MnO and AO rocksalts.

We can further validate our results indirectly based on reported phase transformations during the electrochemical cycling of alkali-containing MnO_2 structures. For example, the decomposition of the orthorhombic $LiMnO_2$ structure to the λ-type

$LiMn_2O_4$ spinel on Li^+ removal which can be seen in Figure 4-4a is well documented in the literature[185, 186]. Similarly, Sun *et. al.* have recently reported that Mg^{2+} intercalation into δ-MnO in the absence of water results in irreversible decomposition of the δ structure, while in the presence of water, quasi-reversible conversion between hydrated δ-$Mg_{0.15}MnO_2 \cdot 0.9H_2O$ and dry λ-MnO_2 is possible[161]. This result is in agreement with the stabilization of δ-$Mg_{0.25}MnO_2$ by hydration seen in Figure 4-2d with respect to the anhydrous β-MnO_2 - λ-$Mg_{0.5}MnO_2$ equilibrium line. As the anhydrous δ phase is never stable for Mg_xMnO_2 , $0 \leq x \leq 0.5$, we would expect that after initial decomposition on Mg insertion, there would never be a driving force for the δ phase to reform on Mg extraction, while in the hydrated case, reformation of the δ structure is thermodynamically plausible. The coupling between intercalation and structure selection seen in our data, and illustrated in these experiments, enables electrochemical processing to function as an effective structure-sensitive synthesis tool in the case of redox-active systems such as MnO_2 .

The mechanism by which various alkali cations stabilize a particular polymorph is related to two primary characteristics of a MnO_2 framework - the compatibility between available interstitial sites and the preferred coordination environment of the alkali ion, and the ability of the framework structure to accommodate changes in electronic configuration, both due the electrostatic repulsion of intercalated cations, and the change in Mn redox state upon intercalation. To derive these characteristics, we examine the effect of cation size and cation valence, noting that Li^+ and Mg^{2+} have very similar ionic radii, as do Na^+ and Ca^{2+}, which allows us to examine the effects of size and valency independently of each other. Furthermore, we relate the stabilization of certain A_xMnO_2 structures by water to the ability of water to increase the coordination of cations in otherwise unstable sites, creating a partial solvation shell around around the cation. Importantly, structure stabilization by water is specifically not a consequence of the interaction of water with the MnO_2 framework directly, but rather of the ability of water to stabilize intercalated cations in the structure.

The first relationship between cation type and phase selection is that of the compatibility between available interstitial sites in the structure and the preferred coordination of the alkali ion. For example, the hollandite α phase contains four potential intercalation sites - the 8-fold coordinated 2b and 4-fold coordinated 2a tunnel-centered sites, and the asymmetrically 4-fold and 5-fold coordinated off-center 8h' and 8h sites respectively. The only cation large enough to occupy the 2b site is K^+, creating a highly stable, well-coordinated alkali-oxygen environment that results in the wide window of stability for α-MnO_2 across K chemical potentials consistent with experimental results[156, 182, 157, 183, 184]. The slightly smaller Na^+ and Ca^{2+} are not stable in the 2b site, instead occupying the lower-coordinated 2a and 8h sites. Nonetheless, the bonding afforded by these sites, while less strong than in the case of K^+, provides sufficient alkali-oxygen coordination to stabilize α within a limited range of Na^+ and Ca^{2+} chemical potentials. Finally, in the case of Li^+ and Mg^{2+}, the ionic radius of the cation is only compatible with the asymmetric and low-coordinated 8h and 8h' sites, failing to provide any reasonable coordination geometry for the intercalated cations. Thus, Li^+ and Mg^{2+} do not stabilize the α framework in agreement with reported decomposition of the α phase on Li^+ and Mg^{2+} insertion[146, 169].

The opposite trend can be observed in the stability of the λ phase, which only has relatively small tetrahedral and octahedral sites. The small alkali-oxygen bond lengths of the tetrahedral site allow it to form a highly stable coordination environment in the presence of Li^+ or Mg^{2+}, while failing to accommodate the larger Na^+, Ca^{2+}, or especially K^+ ions, as can be seen by the destabilization of the tetrahedrally-occupied spinel-type λ-AMn_2 O_4 with increasing cation size. However, the most extreme example of coordination preference is that of proton-incorporated structures. While intercalated protons tightly bind to oxygen to form OH^- groups, stable proton sites are those where the proton bridges two oxygens, in agreement with previous FTIR results[187]. The [1x1] and [2x1] tunnels in β, R and γ, as well as the layer stacking arrangement in δ, create numerous environments where such a O-H-O bridge is possible, while the [2x2] tunnel structure of α does not allow for any such environments to form. Correspondingly, the α phase is rapidly destabilized by proton intercalation, as can be seen in Figure 4-3a. Thus, compatibility of cation size and coordination preference with the MnO_2 framework is a key parameter determining the feasibility of structural stabilization by alkali intercalation.

A second characteristic of alkali-to-polymorph compatibility is the ability of the transition metal structure to accommodate the valency of the alkali, manifested both in reduction of the transition metal, and the electrostatic repulsion between the intercalants. A clear example of this effect is the difference in the stabilization of α by the similarly sized Na^+ and Ca^{2+}, seen in Figures 4-2b and 4-2e. While both cations occupy similar 2a and 8h sites, the maximum stable concentration of Ca^{2+} in the α tunnels is lower than that of Na^+ due to the stronger electrostatic repulsion between Ca ions in the same α tunnel. As a result, the composition window over which Na^+ stabilizes α is much wider, as can be seen in Figure 4-2.

The effect of transition metal redox can be most clearly seen in the differences in phase selection between Li^+ and Mg^{2+}. At the fully intercalated $AMnO_2$ composition, all low energy structures place the alkali ion into an octahedral site, with the key difference that in the Li case, the Mn is in the Jahn-Teller active Mn^{3+} redox state, while in the Mg case, the Mn is in the Jahn-Teller inactive Mn^{2+} state. As a result, the structure of $MgMnO_2$ is the highly symmetric O3-δ phase, with the similarly symmetric octahedrally-occupied λ is only slightly unstable, while the $LiMnO_2$ structure strongly favors the low-symmetry o-$LiMnO_2$ geometry, which is able to accommodate Jahn-Teller distortions much better than the δ or λ phases. A similar effect can be seen in the the Na^+ and Ca^{2+} cases at the $AMn_2\ O_4$ composition. In $CaMn_2\ O_4$ case, the Mn is fully in the Jahn-Teller active 3+ state, while in the $NaMn_2\ O_4$ case, half of the Mn remains in the Jahn-Teller inactive 4+ state. Correspondingly, Ca stabilizes the highly-distorted marokite-type structure, while $NaMn_2\ O_4$ exists in the more symmetric post-spinel phase. A detailed illustration of the Jahn-Teller distortions in Mn^{3+}-containing structures as compared to pure

Mn^{2+} and Mn^{4+} phases, which we calculate in close agreement with recent EXAFS results[188], is available in Appendix G. While neither of these structures correspond to the six canonical MnO_2 polymorphs, they provide further evidence to the relationship between redox-state-controlled coordination-environment distortions and phase selection. Put together, the need for the transition-metal framework to accommodate both the change in the transition-metal redox state, and minimize electrostatic repulsion between intercalants introduces a further degree of selectivity between intercalant and the polymorphs it is able to stabilize.

The last important characteristic of alkali-mediated phase stabilization is the interaction of intercalated phases and water, analogous to recently reported results in MgV_2 O_5[189]. In pure MnO_2 structures, the only phase that we predict to hydrate exothermically is the layered δ phase, with even the fairly open α phase preferring to dehydrate. These results are consistent with the relaxed structure of the hydrated phases - while the hydrated structures are initialized with many water molecules oriented so as to create proton bridges with the oxygens in the MnO_2 framework, relaxed hydrated structures always minimize bonding between MnO_2 and water, creating clusters of water molecules that appear to be repelled from the MnO_2 structure itself. Similar structural changes occur in δ also, but it is likely that the medium-range van-der-Waals interactions with the water layer are stronger than between MnO_2 layers, stabilizing hydration even in the absence of direct bonding between MnO_2 and water.

In the presence of alkali cations, the behavior of water in the structures changes dramatically, as water is now able to bind to the highly-soluble alkali cations. As discussed earlier, the Li^+ and Mg^{2+} -intercalated α phase is unstable due to the low coordination of the alkali cations. When these structures are hydrated up to 0.25 mol H_2 O/mol MnO_2 however, the water coordinates the cations so as to increase their coordination from 4- and 5- fold for Li^+ and Mg^{2+} to 6- fold and 7-fold respectively. As the water compensates the undercoordination with a partial solvation shell, hydration helps to stabilize the intercalated α phase, as can be seen in Figures 4-2a and 4-2d.

Conversely, in the relatively well-coordinated Na^+ and Ca^{2+} α phases, hydration has a negligible effect on phase stability, while in the well-coordinated K-intercalated α, hydration is endothermic even at dilute K content. Thus, we may conclude that the most important effect of water is to stabilize alkali cations in otherwise unstable, undercoordinated environments, helping stabilize less dense MnO_2 frameworks. While we did not consider larger tunnel structures in this work, it is possible that this stabilization of undercoordinated alkali intercalants by water may explain the success of synthesis recipes for the larger [2x3], [2x4] and [3x3] tunnel analogs of the α phase by the cointercalation of significant quantities of Na^+ and water[190, 191, 192, 193]. Similarly, the energetic balance of alkali coordination by the MnO_2 framework and co-intercalated water explains the diversity of birnessite and buserite minerals, all variants of the layered δ phase with varying degrees of alkali solvation.[194, 195]

4.4.2 Proton-stabilized phases: γ and R

While alkali intercalation explains the stability of α, δ, and λ -MnO_2 , the two remaining frameworks, R and γ, are never ground states for any level of alkali incorporation. In the case of Li^+ and Mg^{2+}, the formation energy of R and γ with respect to the true thermodynamic ground state is small, as can be seen in Figures 4-2a and 4-2d, which is consistent with experimental reports of metastable R- and γ- type Li_xMnO_2 [155]. Nonetheless, it does not appear that any level of lithiation can truly thermodynamically stabilize the R or γ type framework.

We may speculate that one possible mechanism explaining the formation of ramsdellite is based on the effect of Coleman protons and the contribution of their configurational entropy to free energy at relatively high temperatures. Based on the the stability map shown in Figure 4-3c, one route by which R-MnO_2 could form is through the entropically stabilized R-type $H_{0.5}MnO_2$. Indeed, a R-type phase at this composition has been previously observed as a transient state in ramsdellite growth, as well as proton insertion into ramsdellite[153, 77]. In both cases, this phase has been termed “groutellite” by analogy to the metastable R-type groutite MnOOH phase.

Single-crystal ramsdellite can be synthesized through hydrothermal processing of a Li_xMnO_2 precursor in strong acid[155, 53], which further suggests that acid-mediated delithiation may lead to the formation of a protonated intermediate, which at high temperatures would favor the R-MnO_2 framework. The incorporation of protons into MnO_2 frameworks during acid-induced ion extraction may be key to the formation of the relatively dense R-MnO_2 structure, which much like β, is too dense to be stabilized by the intercalation of significant quantities of any cation larger than H^+.

One alternate mechanism for the formation of the R and γ phases involves the formation of Ruetschi defects. While these defects are metastable, and have been shown to irreversibly anneal out of the structure[176], Ruetschi defects are typically present in electrolytic manganese oxide (EMD), which predominantly consists of the γ phase[153]. The typical concentration of Ruetschi defects found in EMD is 0.05-0.09 % [176, 179], at which composition we indeed find γ or R to be the stable form of MnO_2 based on the stability map in Figure 4-3c. We may speculate that the origin of the trapped protons is two-fold. First, as EMD is typically grown by electrodeposition at high rates from an acidic solution of $MnSO_4$ and H_2 SO_4[158], the deposition of MnO_2 solid from Mn^{2+} ions involves the deprotonation of H_2 O[196]. At high deposition rates, any incomplete deprotonation would lead to a fraction of hydroxyl groups in the deposited structure, which would lead to the formation of Ruetschi defects, or metastable Coleman protons. After they are formed however, it is very difficult for Ruetschi defects to anneal out of the structure. To do so, they must reform a water molecule, which then must be transported through the EMD bulk. However, the [2x1] and [1x1] tunnels making up the γ-MnO_2 structure are small, such that the activation barrier for water to diffuse through the structure is very high, based on the energy required to place a water molecule in a R or γ-phase tunnel. Consequently, after their initial formation, Ruetschi defects likely remain trapped in the EMD structure, thereby stabilizing it against transformation to the β ground state phase.

Put together, the Ruetschi-defect and Coleman-protons may both stabilize R and

γ, as can be seen in Figure 4-3c. Thus, while the two mechanisms are distinct and are likely to arise in differing synthesis environments, both can lead to the formation of R or γ, suggesting that the careful characterization of proton content in MnO_2 may reveal identifying the formation mechanisms for these two phases.

Circumstantial evidence of the importance of protons in the formation of R and γ can be found in existing *in situ* data. Shen *et. al.*[162] observe a series of transformations from Na-birnessite precursors to other MnO_2 phases by *in situ* diffraction. The first observed pathway, which forms β from the birnessite precursor at high temperature and in highly acidic media, involves initial layer collapse due to chemical desodiation and/or dehydration, followed by a transformation from δ to R/γ and eventually β. It is likely that the acid-induced chemical desodiation of the structure simultaneously destabilizes the δ-MnO_2 framework, as can be seen in Figure 4-2b, and leads to the incorporation of protons into the MnO_2 structure. The proton incorporation leads to the formation of R/γ-MnO_2 at high temperature, which transforms to the β ground state as the protons are slowly annealed out. Consistent with this interpretation, the authors observe a change of the endpoint phase from β to α and a disappearance of the R/γ intermediate when the reaction is done in a more basic environment and at a higher external sodium chemical potential. hile alternate explanations of these observed pathways are certainly possible, we hypothesize that this quasi-equilibrium thermodynamic interpretation of the generally slow transformation process provides a compelling energetic foundation for phase transformations such as that reported by Shen *et. al.* in this system.

4.5 Selectivity of off–stoichiometric stabilization

Todorokite MnO_2 is a unique structure among the transition metal oxides owing to its exceptionally high porosity, and more specifically, large channel size. While todorokite is typically defined as a 3 by 3 tunneled manganese oxide mineral, its true atomistic structure has not been previously resolved. As most functional applications of todorokite, from molecular sieving to charge storage, depend on the precise geometry of its large conductive tunnel, this ambiguity presents a fundamental challenge to the development of structure-property relationships for this phase. Using high angle annular dark field (HAADF) imaging, my collaborators revealed the inhomogeneous structure of todorokite-MnO_2, resolving the diversity of tunnel sizes coexisting even in well-crystallized particles[197]. Here, I rationalize the formation and persistence of this distribution of tunnel sizes using first-principles thermochemical calculations, demonstrating the stabilization of a range of todorokite-like environments by the intercalation of partially solvated Mg^{2+} cations. Our results not only help resolve the structural character of the todorokite MnO_2 phase, but also suggest generalizeable principles determining the selectivity of off–stoichiometric structure-selection.

In this section, we refer to the todorokite family of structures as τ-MnO_2, where a structure with a N by 3 tunnel framework is denoted as belonging to the τ(Nx3) phase. As the τ(2x3) and τ(4x3) structures are crystallographically constrained to appear as doubled cells, we model their behavior as an ordered integrowth of a 2 by 3 and 4 by 3 tunnel, which we refer to the as the τ(2x3 + 4x3) phase.

Experimentally, the τ-MnO_2 family of structures form from aqueous, Mg^{2+}–containing solutions[190, 194, 197]. As alkali ions and hydration have been recently discussed as thermodynamic structure–directing agents in MnO_2 frameworks[90], we have investigated the role of Mg^{2+} in driving the formation of the τ-MnO_2 large tunnel structures. Configurational enumeration of the τ(3x3), τ(1x3), τ(2x3 + 4x3), and τ(5x3) phases across Mg_xMnO_2 and $Mg_xMnO_2 \cdot yH_2O$ compositions reveals that in all cases Mg^{2+} occupies sites at the corner of the MnO_2 tunnel. As can be seen in Figure 4-5a for the example of the traditional τ(3x3) todorokite structure, these sites provide the maximal coordination of Mg^{2+} by lattice oxygens. When H_2O is present, the oxygen from the water molecule orients towards the Mg^{2+}, further increasing its coordination, approaching the typical 6–fold coordination environment found in octahedral Mg–O

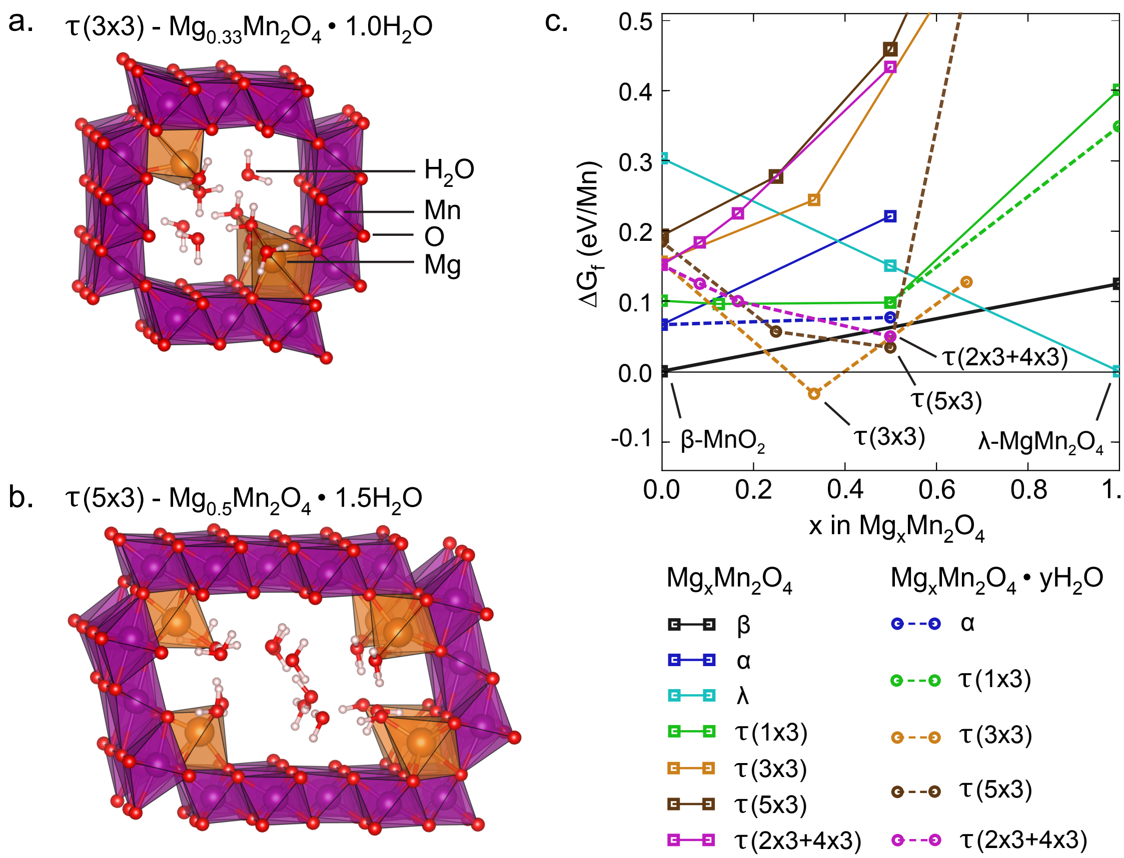

Figure 4-5: Stabilization of the τ-MnO_2 phase by the co-intercalation of Mg^{2+} and H_2O. The partially desolvated Mg^{2+}-H_2O complex occupies tunnel corner sites, stabilizing not only the (**a.**) traditional 3 by 3 tunnel todorokite structure, but also a range of other τ-MnO_2 structures such as the (**b.**) 5 by 3 tunnel structure. (**c.**) Relative Gibbs free energies of formation of the τ-MnO_2 phases at 200 ^{o}C across the $Mg_xMnO_2 \cdot yH_2O$ composition space with respect to the low–energy β, α, and λ Mg_xMnO_2 phases. For each value of x, the solid lines denote the formation energy of the non–hydrated Mg_xMnO_2 structure, while the dashed lines denote the expected formation energy for the most stable $Mg_xMnO_2 \cdot yH_2O$ structure. The free energy of the N by 3 tunnel structures with either Mg^{2+} or H_2O intercalation is consistently higher than that of the other low-energy phases in the Mg-MnO_2-H_2O space. However, the co-intercalated τ-$Mg_xMnO_2 \cdot H_2O$ structures are much lower energy and stable with respect to the β-MnO_2 and λ-$MgMn_2O_4$ endpoint phases.

complexes. This result is at odds with the picture of todorokite presented earlier[198], which placed Mg^{2+} in the tunnel center site. However, but this earlier refinement was highly uncertain in its chemical identification due to the similar X-ray scattering potential of Mg and O. Our analysis suggests that instead, the tunnel center is much more likely to be occupied by a water molecule.

While Mg^{2+} appears to strongly prefer the tunnel corner site, this site occupancy does not uniquely constrain the remaining Mn–O framework. In general, the hydrated Mg^{2+} ions occupying tunnel corner sites must be sufficiently separated from each other to avoid steric repulsion, but they do not directly interact with the Mn–O framework outside of the tunnel corner, leaving the overall tunnel size unconstrained. Consequently, a range of tunnel sizes exhibit the same behavior with partially hydrated Mg^{2+} occupying tunnel corner sites, such as in the τ(5x3) structure shown in Figure 4-5b. Similar behavior can even be observed in the smaller 2 by 2 tunnel found in the α-MnO_2 phase, although the strong electrostatic repulsion between adjacent Mg^{2+} ultimately destabilizes this smaller–tunnel phase[90].

The favorable Mg^{2+}–O coordination afforded by the tunnel corner site and hydration significantly stabilizes the Mg–intercalated τ-MnO_2 structure. The formation energies of these phases with respect to the β–MnO_2 and λ–$MgMn_2O_4$ endpoint phases shown in Figure 4-5c reveal that while the τ-Mg_xMnO_2 phases have high formation energies for all tunnel sizes, τ–$Mg_xMnO_2 \cdot yH_2O$ have much lower formation energies, and in the case of τ(3x3), are thermodynamically stable with respect to β–MnO_2, λ–$MgMn_2O_4$ and water at 200 ^{o}C. This result suggests that the formation of the τ-MnO_2 phase by hydrothermal growth from a Mg^{2+}–containing solution is thermodynamically controlled and indeed driven by the compatibility of this phase and the Mg^{2+}-H_2O complex.

The impact of the partially–solvated Mg^{2+}-H_2O complex in stabilizing the τ-MnO_2 family of structures suggests a plausible explanation for the diversity of tunnel sizes observed experimentally. The intercalated cation stabilizes the local Mn–O environment corresponding to a tunnel corner, and strongly repels other cations owing to its divalent charge, driving the formation of relatively large tunnel sizes. These structure–selection criteria are satisfied to varying degrees by the τ(3x3), τ(1x3),

τ(2x3+4x3), and τ(5x3) structures. Accordingly, all these phases have relatively low formation free energies as shown in Figure 4-5c. While we find the τ(3x3) phase to be lowest in free energy, the nucleation of this phase does not exclude the coherent formation of domains corresponding to the other low–energy τ-MnO_2 structure. While the total energy of such a non–equilibrium domain in a macroscopic particle is high, at the nucleation stage these diverse domains may be expected entropically. Of course, an alternative explanation for the experimental results is that we simply have not been able to resolve the configuration of the more complex, low–symmetry τ(2x3+4x3) and τ(5x3) structures as well as that of the τ(3x3), as the relaxation of the hydrated configurations in particular are fairly uncertain and prone to errors due to numerous local–minima. In this case, we may still conclude that the various τ-MnO_2 phases are stabilized by the partially–solvated Mg^{2+}-H_2O complex without forming any bonding environments that would strongly prefer a particular tunnel size. Thus, the todorokite–like structure formed experimentally is unequivocally thermodynamically favored by the co-intercalation of Mg^{2+} and H_2O, with disorder in tunnel sizes arising as a consequence of the diversity of Mn–O frameworks which accommodate the stable Mg^{2+}-H_2O bonding environment.

A stark contrast to the lack of structure-selecting constraints and resulting polytypism in the todorokite family of structures is the unique 2 by 2 tunnel size observed in hollandite MnO_2 structures. The origin of this difference lies in the geometry of stabilizing alkali intercalants in the tunnel structure, and their effectiveness at constraining degrees of freedom in the structure. Polytypism of the τ(Nx3) family arises from the fact that the partially solvated Mg^{2+} cation that stabilizes this tunnel occupies the tunnel corner site and only interacts strongly with the Mn-O framework immediately adjacent to this single tunnel corner. The lack of strong bonds spanning the width of the tunnel leaves the total tunnel size unconstrained, and results in a range of large tunnel sizes close in energy to each other. In contrast, the 2 by 2 tunnel seen in the hollandite structure is generally not stabilized by cations occupying corner sites, and instead is found with larger cations such as K^+ in the tunnel center site.

These cations interact strongly with all sides of the Mn-O tunnel and thus constrain its size. The unique stable cation site in hollandite thus suppresses polytypism and promotes the formation of a single type of local environment. Generalizing from this observation, we speculate that among intercalation-stabilized phases, the structural selectivity provided by a stabilizing cation is directly proportional to the fraction of structural degrees of freedom constrained by the cations' local bonding environment.

4.6 Off–stoichiometry and nucleation effects

While off–stoichiometry can offer a route to stabilizing a diverse array of crystal structure types in the bulk, finite–size effects and the related issue of nucleation and growth kinetics discussed in chapter 3 remain important in understanding the reaction pathways leading to the bulk endpoint phase. Phases stabilized at small particle size and favored by nucleation kinetics may be favored as transient growth intermediates, and could be extracted as synthesis products by quenching the growth process at an early time before the reaction reaches completion. Just as off–stoichiometry offers a handle on the relative stability of bulk phases, it also offers an avenue to control finite–size stability and nucleation preference. To evaluate the joint effect of particle size and composition, I construct higher dimensional phase diagrams, combining the role of various cation chemical potentials discussed in chapter 4, with the finite–size effects discussed in Chapter 3. The resulting phase stability map charts out the phases stabilized across relevant chemical potentials and particle sizes, offering an exhaustive list of phases potentially obtainable by nucleation and growth in a synthesis medium defined by the set of considered chemical potentials. This analysis offers a direct view of hydrothermal synthesis from a medium containing a number of ionic species and proceeding through a nucleation and growth process.

A rigorous test of the predictive power of the quasi–thermodynamic picture of synthesis is a direct comparison between computed growth pathways and a synthesis experiment conducted under the same conditions. In the following section, I describe two such tests, focusing on the nucleation and growth of manganese oxide polymorphs from sodium- and potassium- containing aqueous solutions. The experimental data for this work, described in detail in the associated publications[199, 200], was provided primarily by Bor-Rong Chen, Praneetha Selvarasu, Laura Schelhas, Lauren Garten, and Kevin Stone. Here, I present my contribution to the theoretical analysis of these systems and growth processes.

The relevant molar thermodynamic potential ψ for hydrothermal growth from aqueous solution combines the finite–size thermodynamic potential derived in chapter 3, with the potential derived to account for off-stoichiometry earlier in chapter 4, and is given as

$$\psi = g_b - n_A\mu_A + n_e e\phi + \frac{\gamma\nu}{\rho r}$$

where g_b is the molar bulk Gibbs free energy of formation. This potential accounts for the incorporation of n_A external ions at a chemical potential of μ_A into the growing phase. As the incorporation of cations is a reductive process, the relative stability of oxidized and reduced phases depends on the external electronic potential, ϕ, and n_e, the number of electrons transferred in the formation reaction. Finally, the energy of a finite size particle with effective particle radius r and molar density ρ depends on its surface energy γ, scaled by its Wulff shape factor ν ($\nu = \frac{Ar}{V} = 3$ for a sphere). This construction is equivalent to that derived in chapter 3, with the difference that the potential is normalized to yield the molar free energy, replacing the particle volume V and surface area A by a ratio of the two. In terms of conventional solution handles, the redox potential ϕ is measured as the oxidation-reduction potential (ORP), while the chemical potential of protons, μ_{H^+} is represented by pH ($\mu_{H^+} = -2.303k_BT$ pH)). The chemical potentials of other cations, A^+, can be mapped to their concentrations through conventional activity models or a simple ideal–solution approximation ($\mu_{A^+} = \mu^0_{A+} + k_BT\ln[A^+]$). By evaluating phases stabilized in ψ across all particle sizes and experimentally–obtainable potentials, we obtain a full list of possible synthesis products favored during some stage of growth, as well as the solution conditions necessary to obtain each phase.

Within the manganese oxide system, there are a large number of competing phases with phase transitions which offer a difficult benchmark for the ability of this theory to reproduce synthesis behavior. We focus on two systems in particular, Na-Mn-O-H and K-Mn-O-H, chosen on the basis of existing synthesis literature and the experimental accessibility of predicted phase boundaries in an aqueous growth medium. In both cases, we examine the role of increasing alkali ion potential on the synthesis product obtained from aqueous precipitation, accounting for the effect of size–effects on nucleation preference. To do so, we construct phase diagrams with axes of alkali chemical potential and $1/r$, the inverse particle radius, at a fixed solution pH and oxidation potential. Naturally, the solution pH and oxidation potential can be systematically changed and chosen to lie anywhere within the higher–dimensional thermodynamic stability field of the target phase, where the dimensions capture all thermodynamic handles. However, as our goal is to compare our theoretical predictions to experimental growth results, we choose the pH and oxidation potentials to match those measured experimentally at the beginning on the synthesis, where we assume initial nucleation and phase selection to occur.

4.6.1 Computational methodology for interfacial energies

To resolve the size–dependent potential ψ, and obtain data quantitatively comparable to experiment, three methodological changes are necessary with respect to that described in section 4.2.

First, instead of a universal correction to the Mn oxidation potential, it is necessary to rely on the more accurate SCAN referencing scheme discussed in chapter 2.

Second, it is necessary to include the vibrational contribution to the free energy of Mn–O phases with respect to that of the aqueous Mn^{2+} and MnO_4^- ions. This contribution is approximately constant and equal to -0.063 eV/mol at room temperature, based on the experimental entropy of β-MnO_2 (reference formation Gibbs free energy of -4.837 eV/mol[201] and enthalpy of -5.408 eV/mol[202], entropy of Mn + O_2 reference states 2.1 meV/mol K). The differences in vibrational free energies between A_xMnO_2 phases are small enough not to affect the relative free-energies of these phases (see Appendix F), justifying the use of this single constant free-energy term.

Finally, it is necessary to compute surface energies for the various MnO_2 phases in order to approximate the size–dependent term of ψ. Due to computational limitations, we only directly compute the surface energies of MnO_2 and MnOOH polymorphs as representative structures for the interfacial behavior of Mn^{4+} and Mn^{3+}–containing phases. To obtain these energies, we construct surface slab models of the interface following the same procedure as described in Chapter 3. As the relevant surface energy for hydrothermal growth is that of a hydrated surface, we also compute the energy of all surfaces with an adsorbed monolayer of water. However, these calculations frequently yield unphysical dissociated water molecules on MnO_2 surfaces, forcing us to rely on vacuum surface energies for all subsequent analysis. The result of this necessary simplification is that all surface energies are likely somewhat overestimated. Nonetheless, as we only rely on the relative surface energies of competing phases, the qualitative trends in the computed surface energies are still informative.

To approximate the contribution of surface energy to the free energy of the layered δ-$A_xMnO_2 \cdot yH_2O$ phases, we rely on an interpolation derived from δ-MnO_2 and δ-MnOOH, whose surface energies are resolved explicitly. Specifically, we interpolate the shape factor ν and total surface energy term of the thermodynamic potential ($\frac{\gamma\nu}{\rho r}$) as a function of x between δ-MnO_2 ($x = 0$) and β-MnOOH ($x = 1$) Within a broken–bond approximation, the surface energy of a δ-$A_xMnO_2 \cdot yH_2O$ structure is dominated by the removal of weak interlayer interactions, with some contribution of cleaving the MnO_2 layer itself. The strength of Mn-O bonds scales with the Mn oxidation state. The strength of interlayer interaction is determined by the fraction of the layer occupied by cations forming ionic bonds spanning the MnO_2 layers, versus weak van der Waals interactions between the MnO_2 layers themselves. As the strength of both the inter- and intra- layer interactions to first order only depend on the quantity of monovalent cations in the layer, we approximate the surface energy term in ψ for δ-$A_xMnO_2 \cdot yH_2O$ as a function of x by a linear combination of the surface-energy term derived for δ-MnO_2 and δ-MnOOH, weighted by the quantity of cations or equivalently, the average Mn oxidation state.

In the case of α-A_xMnO_2, we rely on the surface energy of pure α-MnO_2 as the cation content of all relevant α-A_xMnO_2 phases is low, such that the structure and energy of any interface is unlikely to be significantly different from that of the pure endpoint phase. While cation segregation to the interface is in principle possible, resulting in surface enrichment and significantly different surface energy, such a process is unlikely due to the strong electrostatic repulsion between A^+ cations in the α-MnO_2 tunnel and the favorable coordination environment provided by the α-MnO_2 framework.

While the numerous approximations involved in the computation of the A_xMnO_2 surface energies mean the resulting energies are not quantitatively precise, the most basic behavior of surface energies in this system is determined by the type of bonds that are broken within each structure - strong metal-oxygen bonds in the case of the 3D-bonded phases such as β and α, versus weak van-der-Waals bonds in the case of δ. As a result, the surface energies of these two families of structures differ by an order of magnitude, as can be seen in Table 4.1, such that even with the rough approximations presented here, the general trends in surface-energy controlled phase stabilization remain valid.

Phase	γ (J m^{-2})	ν	ρ (Mn/Å^3)
β-MnO_2	1.54	3.85	0.036
R-MnO2	1.33	3.53	0.034
α-A_xMnO_2	1.19	5.35	0.030
δ-MnO_2	0.12	12.77	0.030
δ-$K_{0.33}MnO_2$	0.14†	9.79†	0.023
δ-$K_{0.50}MnO_2$	0.18†	8.31†	0.023
δ-$K_{0.75}MnO_2$	0.25†	6.08†	0.021
δ-$NaMnO_2$	0.56†	3.77†	0.027
γ-MnOOH	0.84	3.85	0.030
α-MnOOH	0.65	4.34	0.029
β-MnOOH	0.56	3.77	0.027
Mn_3O_4	1.53	3.30	0.038

Table 4.1: Computed and interpolated vacuum surface energies of MnO_x phases. † The surface energies and shape factors of δ-A_xMnO_2 phases are derived from an interpolation of the surface energy term ($\frac{\gamma\nu}{\rho r}$) and shape factor ν for δ-MnO_2 and β-MnOOH. The surface energies of hydrated layered phases are taken to be the same as those of the unhydrated phases.

4.6.2 Transition from β-MnOOH to Na-birnessite

In the case of sodium–containing manganese oxides, the most commonly observed phase is layered birnessite δ-$Na_xMnO_2 \cdot yH_2O$. While the hollandite–type α-$Na_{0.125}MnO_2$ phase is computationally predicted to be stable, as can be seen in Figure 4-4, it has not been reported experimentally. The growth of sodium birnessite can be accomplished in a moderately oxidizing solution starting with a $Mn^{2+}SO_4$ precursor, with the oxidation strength set for example by ammonium persulfate (APS), and sodium and pH controlled by the addition of NaOH. Under these conditions, corresponding to an oxidation potential of approximately 250 mV, pure birnessite forms at pH 12 and higher, with a concentration of Na^+ in excess of 1M. Lowering the pH slightly to 10 results in a sodium–free layered MnOOH product, with a structure corresponding to the layered β-MnOOH phase, and further reductions in pH result in hausmannite Mn_3O_4. At pH 11 a mixed phase product consisting of β-MnOOH and δ-$Na_xMnO_2 \cdot yH_2O$ forms. While birnessite and hausmannite are thermodynamically stable under some solution conditions, β-MnOOH is always metastable the bulk, suggesting that the justification of its growth requires a closer analysis of the nucleation and growth process itself.

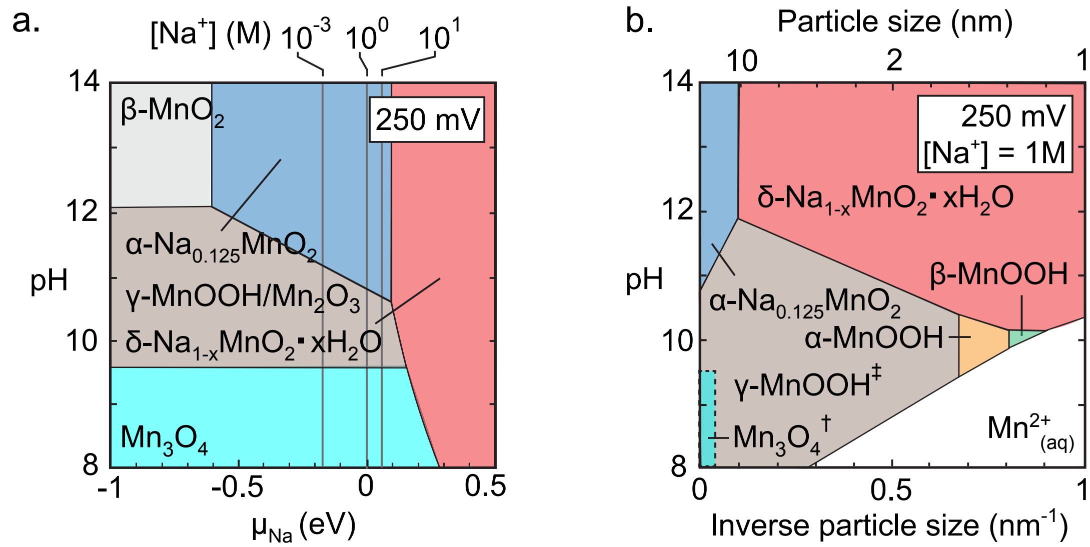

Figure 4-6: Phase selection in the growth of manganese oxides from a sodium-containing solution under fixed oxidation potential. **a.** Bulk stability of various proton and sodium containing manganese oxides as a function of pH and aqueous sodium potential. **b.** Effect of nano–scale size effects on the stability of these manganese oxide phases, mapping the energetics relevant for phase selection during nucleation. † The finite-size stability of Mn_3O_4 is not shown as the surface energy of Mn_3O_4 is highly uncertain. ‡ γ-MnOOH and Mn_2O_3 are computed to be nearly degenerate in energy under these conditions, such that their relative stability is uncertain.

The pH–dependence in synthesis observed experimentally can be well–explained by considering the finite–size energetics in the Na-Mn-O-H system. The phase diagram of ψ corresponding to this synthesis environment, shown in Figure 4-6, illustrates the transition in nucleation preference from birnessite δ-$Na_xMnO_2 \cdot yH_2O$ to β-MnOOH to Mn_3O_4, even though β-MnOOH is never favored in the bulk. In fact, as can be seen in Figure 4-6a, the birnessite δ-$Na_xMnO_2 \cdot yH_2O$ product is not stable even at a 10M aqueous concentration of Na^+, meaning that it is also a bulk–metastable synthesis product at the synthesis conditions under which it is grown. Only the formation of hausmannite Mn_3O_4 below pH 9 is can be explained by bulk thermodynamics alone. The origin of the layered products at higher pH values is evident from the finite–size phase diagram shown in Figure 4-6b. The β-MnOOH phase is the favored phase at the nanoscale in a narrow pH window around pH 10, suggesting that under these conditions it would nucleate first and may be retained if the reaction is quenched quickly enough, in close agreement with experiment. Moving to higher pH values, birnessite δ-$Na_xMnO_2 \cdot yH_2O$ becomes the favored nucleation product, consistent with its experimental observation above pH 11. The equilibrium product under these conditions, α-$Na_{0.125}MnO_2$ only becomes stable at relatively large particle sizes, suggesting that the formation of this phase is kinetically suppressed due to the ease to nucleating the competing birnessite phase.

4.6.3 Stepwise crystallization of α-K_xMnO_2 and β-MnO_2

Another system offering an opportunity to test size–dependent phase selection is the potassium manganese oxides. When sodium is replaced with potassium, the α–hollandite phase becomes significantly more stable, as discussed in an earlier section of this chapter. Correspondingly, growth of manganese oxides from a potassium–containing solution typically results in α-K_xMnO_2, although layered birnessite–type structures can also be obtained[156, 182, 157, 183, 184]. Furthermore, starting with the highly oxidized $KMn^{7+}O_4$ precursor rather than the $Mn^{2+}SO_4$ used in the previous synthesis helps to achieve higher oxidation potentials in solution and probe a different region of phase space, where for example the pure MnO_2 phases are expected be stable. Following previously reported synthesis procedures[156, 182, 157, 183, 184], we obtain a manganese oxide product hydrothermally from a solution of $KMnO_4$, $HMnO_4$, and HNO_3 with a ORP of 1200 mV and pH 2, focusing on solutions with $[K^+] < 10^{-6}$M and $[K^+] = 0.2$M. We monitor phase evolution in the crystallizing product using in-situ x–ray scattering, and compare to the quasi–thermodynamic stability map of the K-Mn-O-H system as a function of K^+ potential and particle size. The comparison of the order of phases observed in-situ, and the order of phases predicted by the size–dependent phase diagram offers a direct test of how well our quasi–thermodynamic analysis is able to predict a real growth pathway.

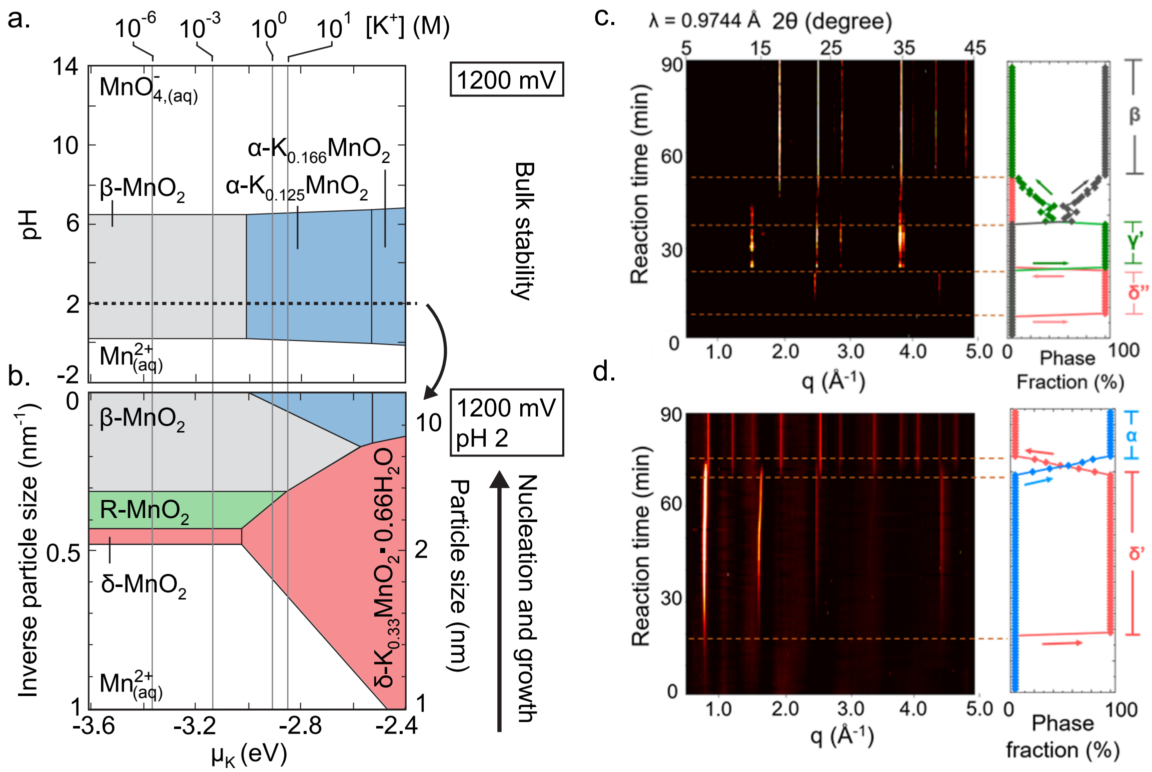

Figure 4-7: Phase selection in the growth of manganese oxides from a potassium-containing solution under fixed oxidation potential. **a.** Bulk stability of various proton and sodium containing manganese oxides as a function of pH and aqueous potassium potential. **b.** Effect of nano–scale size effects on the stability of these manganese oxide phases, mapping the energetics relevant for phase selection during nucleation. **c.,d.** Phase evolution during the hydrothermal growth of manganese oxide from solutions with $[K^+] < 10^{-6}$M (**c.**) and $[K^+] = 0.2$M (**d.**) as mapped by in-situ x-ray scattering. The δ' and δ" phases denote partial disorder in the layer stacking. γ' denotes a disordered integrowth of the R and β phases which was not explicitly considered in the finite–size phase diagram due to the complexity of resolving surface energies of disordered phases.

A comparison of the phases predicted to be size–stabilized and observed in-situ is illustrated in Figure 4-7. Within the experimentally relevant range of potassium potentials, the only bulk–stable products are the β-MnO_2 and α-K_xMnO_2 phases, as can be seen in Figure 4-7a. Taking into account finite–size effects and nucleation preference however reveals a much richer phase diagram, as can be seen in Figure 4-7b. The layered δ-MnO_2 and δ-$K_{0.33}MnO_2 \cdot 0.66H_2O$ phases are favored at the smallest sizes and by initial nucleation. At intermediate particle sizes and low potassium potentials, the ramsdellite R-MnO_2 phase are stabilized. Finally, at particle sizes exceeding approximately 10nm in radius, the bulk-stable β-MnO_2 and α-K_xMnO_2 phases become stable.

Experimental results in the low potassium region, shown in Figure 4-7c, give close agreement with the predicted order of phase formation. Initially, a δ-MnO_2 phase nucleates, albeit with significant disorder in its layer stacking as could be expected from the weak van-der-Waals interactions between the otherwise non–interacting O-Mn-O layers. At intermediate reaction times, a disordered γ' phase forms, which consists primarily of R-MnO_2 domains, with approximately 20% intergrowth of β-MnO_2. While the surface energy of this phase is not explicitly known, it is reasonable to expect that it would be similar to that of R-MnO_2 owing to their structural similarity. Finally, the equilibrium endpoint of the synthesis is the β-MnO_2 phase. This pathway is qualitatively consistent with the progression predicted by the size–dependent phase diagram, offering support for the predictive power of the underlying quasi–thermodynamic analysis.

The higher-potassium region reveals a somewhat more complicated picture. The size–dependent phase diagram predicts a progression of phases starting with the nucleation of δ-$K_{0.33}MnO_2 \cdot 0.66H_2O$, proceeding to the formation of R-MnO_2 and β-MnO_2, and finally settling on α-$K_{0.125}MnO_2$. In contrast, experimentally, only the δ-$K_{0.33}MnO_2 \cdot 0.66H_2O$ starting point and α-$K_{0.125}MnO_2$ endpoints are observed. This discrepancy is consistent with the assumptions of the quasi–thermodynamic analysis. The size–dependent phase diagram provides a highly restricted list of phases which may form. However, kinetic barriers not included in the finite–size analysis may always suppress the formation of a predicted phase. In the case of K-MnO_2 growth, we may speculate that the formation of R-MnO_2 and β-MnO_2 intermediates is suppressed because their formation would involve the segregation of all the potassium in the system into the solution, as K^+ defects are very unstable in these structures. Thus, in a diffusion–limited regime, only the δ-$K_{0.33}MnO_2 \cdot yH_2O$ and α-$K_{0.125}MnO_2$ phases are accessible. Nonetheless, this observed discrepancy highlights the importance of resolving kinetic obstacles to otherwise thermodynamic pathways to the prediction of practical synthesis pathways.

4.7 Conclusion

To summarize, in this chapter I addressed the role of off–stoichiometry in determining phase selection based on a case study of manganese oxides.

I first described the coupling between intercalation reactions and structure selection during MnO_2 synthesis, focusing in particular on the β, α, R, γ, δ, and λ polymorphs of MnO_2, synthesized from alkali and alkali-earth containing aqueous solutions. I have identified the compositions and solution conditions that could be expected to stabilize each of the common MnO_2 frameworks, and identified likely mechanisms leading to the formation of these polymorphs. Specifically, the α phase is stabilized by Na^+, Ca^{2+}, K^+ and hydration due to its ability to highly coordinate cations with framework oxygens or inserted H_2O. The λ phase is stabilized by Li^+ and Mg^{2+}, which prefer the small, low coordination sites in this structure. The δ phase is stabilized by hydration and in particular Na^+. To explain these results, I have highlighted the key importance of (1) the compatibility between available interstitial sites and cation bonding preference, (2) the ability of the transition metal framework to accommodate the valency of the intercalant, and (3) the ability of water to form a partial solvation shell around the intercalated alkali, on the stabilization of MnO_2 frameworks by alkali intercalation. Finally, I identified (4) the key importance of protons in the formation of the R and γ forms of MnO_2, both during hydrothermal processing and electrochemical deposition.

Second, I explored the selectivity of off–stoichiometry in guiding phase selection, contrasting phases whose structural degrees of freedom are well–constrained by an intercalated ion, to the case of the polytypic todorokite phase. Precisely understanding such nanostructural features in materials is essential to the rational assessment of structure-property relationships. Through atomic resolution imaging[197] and DFT calculations, my collaborators and I have demonstrated that Mg^{2+}-stabilized MnO_2 todorokite should not be seen as a pure τ(3x3) tunnel structure but rather as a polytypic τ(Nx3) family, where N is an integer generally less than or equal to 6, with 3 by 3, 4 by 3 and 5 by 3 tunnels appearing most frequently. We rationalized this intrinsic polytypism by the non-specific stabilization of τ(Nx3) structures by the co-incorporation of Mg^{2+} and water into the MnO_2 tunnels during hydrothermal synthesis. The resolution of the precise structural character of todorokite provides an opportunity for the precise evaluation of structure-property relationships in this phase, connecting the unique distribution of large tunnel sizes to functionality in catalysis, charge storage, and molecular sieving. More generally, we anticipate that the relationship we derived between constrained structural degrees of freedom and polytypism can be applied to the structural features of synthetic todorokites stabilized by other cationic complexes, as well as other transition metal oxide phases stabilized by cation intercalation and hydration.

Finally, I described two experiments validating the quasi–thermodynamic view of synthesis proposed in chapter 1. Based on a case study of the crystallization of manganese oxides, my collaborators and I have shown that this analysis consistently identifies synthetically accessible metastable phases, and the conditions under which they may be obtained. However, certain intermediate phases predicted by this analysis do not form, likely due to limitations on diffusion on the timescale of particle growth. The particle–size/alkali–potential phase diagrams derived here to map phase stability throughout nucleation and growth greatly restrict the space of potential synthesis products, but still do not account for phases made inaccessible by the slow kinetics of solid–solid transformations. Nonetheless, the close agreement achieved between the predicted synthesis pathways and experimental observations lends significant credibility to the predictive power of the quasi–thermodynamic view of synthesis developed here, and suggests promising directions for further work in understanding materials growth.

Chapter 5

Functionality from metastability - MnO_2 based catalysis

In this chapter, I present an example of a functional metastable material, whose unique properties arise from kinetically–trapped structural features. In manganese oxides, tetrahedrally–coordinated Mn is only observed in the reduced Mn_3O_4 phase, but can be metastably retained in higher oxidation states by rapid electrochemical oxidation. The resulting material forms a highly active oxygen evolution catalyst[203, 148]. In this chapter, I demonstrate that the superior catalytic performance of this material originates from these metastable tetrahedral Mn sites.

The content of this chapter is based, often verbatim, on a collaborative manuscript that is in preparation for publication. The work presented here consists of my theoretical analysis of the experimental results, which are available in full detail in the referenced publication:
Z. Chan, D. A. Kitchaev, J. Nelson Weker, C. Schnedermann, K. Lim, G. Ceder, W. Tumas, M. F. Toney, D. G. Nocera. "Electrochemical trapping of metastable Mn^{3+} ions for activation of MnO_2 oxygen evolution catalysts." [in preparation] (2017)

5.1 Oxygen evolution catalysis

The widespread implementation of solar energy at the level needed for global energy demand [204, 205] requires its efficient storage in the form of fuels [206]. The conversion of water to H_2 and O_2 is one of the most energy dense carbon-neutral fuel schemes to store solar energy[207]. Effective catalysts for the hydrogen evolution reaction (HER) and oxygen evolution reaction (OER) require a design that manages the coupling of electrons and protons so as to avoid high energy intermediates [208, 209]. Of these two proton-coupled electron transfer reactions, the OER is more kinetically challenging because it requires the management of four electrons and four protons. Oxidic catalysts of cobalt[210, 211, 212, 213, 214], nickel[215, 216, 217, 218, 219], manganese[203, 220] and other earth-abundant metals [221, 222] allow OER to be performed efficiently under a wide range of conditions including non-basic solutions, where corrosion of the catalysts may be circumvented by self-healing[223]. The manganese oxidic OER catalysts are particularly unique as they are distinguished by their ability to perform OER in acid [203, 220, 148, 221, 222, 223, 224, 225, 226, 227, 228, 229]. The OER activity of MnO_2 polymorphs is greatly enhanced when Mn^{3+} ions are present in the lattice [53, 230]. The Mn^{3+} ions may be introduced by cycling the potential of the MnO_2 polymorph [231, 232]. Alternatively, the Mn^{3+} ions may also be introduced chemically by using comproportionation of MnO_2 with $Mn(OH)_2$ to produce a hausmannite-like intermediate (α-Mn_3O_4) where Mn^{3+} ions are trapped in tetrahedral sites [203].

In this work, MnO_2 films activated with Mn^{3+}, henceforth referred to as MnO_2^{*3+}, are generated by the comproportionation of Mn^{4+} and Mn^{2+}, induced by a multistep electrochemical deposition of $Mn(OH)_2$ onto birnessite δ-MnO_2 between 1.1V and -0.4V versus NHE. Upon re–oxidation of these films back to a MnO_2 state, ex situ X-ray absorption spectra indicate an average Mn oxidation state of +3.6 to +3.8, respectively, instead of the expected +4.0 of MnO_2. X-ray absorption spectroscopy and other XPS studies on CV deposited MnO_2 films also estimate an average oxidation state of +3.6-3.8, which is consistent with the presence of Mn^{3+} [231, 232]. However, while Mn^{3+} appears to be present in the material and phenomenological known to enhance OER activity, the role of Mn^{3+} in activating films is not understood or why such a reduced state would persist under oxidizing conditions.

Our computational analysis reveals that Mn^{3+} in tetrahedral oxygen lattice sites are kinetically stable, and that the Mn^{3+} sterically strains the lattice raising the 2p O valence band above the $Mn^{3+}(T_d)$ and $Mn^{4+}(O_h)$ valence bands with a commensurate lowering of the metal-based conduction bands. Oxidation of tetrahedral Mn^{3+} is thus more difficult than that of oxygen. These results rationalize why Mn^{3+} is observed to persist at the onset of OER in MnO_2 polymorphs and why the presence of Mn^{3+} enhances OER.

5.2 Computatonal methods

To characterize the electronic structure of MnO_2^{*3+} catalyst, in particular focusing on accurately reproducing the relative energy levels of the transition metal and oxygen states, we rely on hybrid density functional theory calibrated using the GW approximation[233]. This methodology has been recently reported to accurately reproduce the properties of insulators[234] with mixed Mott-Hubbard and charge–transfer behavior, such as the MnO_2^{*3+} system at hand. Specifically, we calibrate the fraction of exact Hartree–Fock (HF) exchange, α_{EX}, introduced into a HSE–type hybrid exchange–correlation functional[34] to reproduce the Kohn–Sham gap obtained from a G_0W_0 calculation:

$$E_{\mathrm{XC}} = (1 - \alpha_{\mathrm{EX}})\, E_{\mathrm{x}}^{\mathrm{PBE}} + \alpha_{\mathrm{EX}} E_{\mathrm{x}}^{\mathrm{HF}} + E_{\mathrm{c}}^{\mathrm{PBE}}$$

where E_{XC} is the exchange–correlation energy and PBE refers to the Perdew-Burke-Ernzerhof exchange–correlation functional[9]. We choose an exact exchange fraction value of $\alpha_{\mathrm{EX}} = 0.35$ based the band gap of α-Mn_3O_4, computed in G_0W_0 to be 3.0

eV, in reasonable agreement with previous calculations[235] and experiment[236, 237, 238]. By calibrating to α-Mn_3O_4, we aim to capture the behavior of both tetrahedrally and octahedrally coordinated Mn, which are all present in this structure. We note that the value obtained by calibration to the birnessite-type MnOOH is also $\alpha_{EX} = 0.35$, while that obtained by calibration to the experimental band gap of α-Mn_3O_4, or the purely octahedral birnessite MnO_2 structure is $\alpha_{EX} = 0.29$. This difference however does not lead to any qualitative changes in the calculation outcomes to the best of our knowledge. All calibration curves are available in Appendix H.

To investigate the redox behavior of mixed tetrahedally and octahedrally–coordinated Mn within an oxide lattice, we study the oxidation behavior of the α-Mn_3O_4 structure, as it contains both types of Mn environments, and is structurally similar to the MnO_x catalyst. We follow a computational methodology previously reported for identifying defect–induced redox behavior in transition-metal semiconductors[239, 240] - starting with the α-Mn_3O_4 structure, we remove electrons from the system one by one, compensating the charge with a homogeneous jellium background, and allowing the system to locally relax while keeping the overall lattice fixed. We then track the oxidation states of the Mn and O atoms in the system by tracing the evolution of their magnetic moment, as the magnetic moment is a precise signature of Mn^{2+}, Mn^{3+}, Mn^{4+}, as well as O^{2-} and O^{-}.

All first–principles calculations are performed using the Vienna Ab-Initio Simulation Package (VASP)[5, 6] using the projector–augmented wave method[8], a reciprocal space discretization of 15 $Å^{-1}$ and a plane–wave cutoff of 650 eV. All calculations are converged to 0.01 eV $Å^{-1}$ on forces, and 10^{-8} eV on total energy to ensure that a reliable minimum is found. Structural models for Mn_3O_4, as well as MnO_2 and MnOOH used in the calibration are obtained from the Inorganic Crystal Structure Database (ICSD)[19], with magnetic orderings chosen based on small supercell enumerations as suggested by previous benchmarks for the MnO_2 system[151].

5.3 Impact of $Mn(T_d)$ on electronic structure

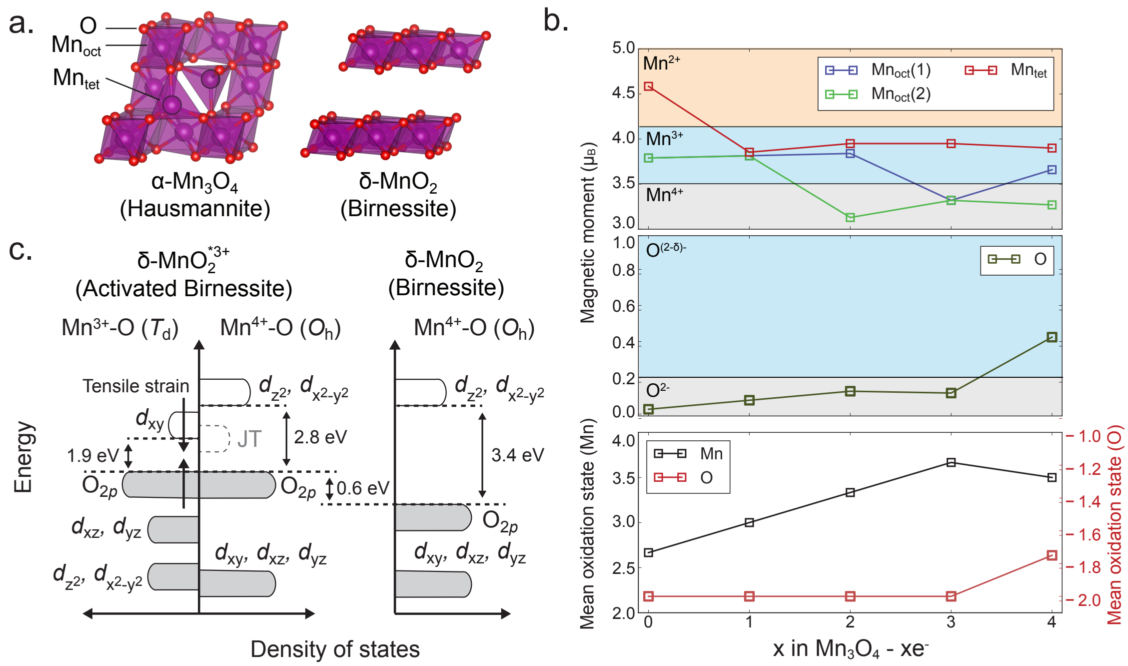

Figure 5-1: Electronic structure of the activated catalyst, based on an oxidized α-Mn_3O_4 hausmannite structure as a model system containing both octahedral and tetrahedral Mn-O environments. **a.** Schematic representation of the α-Mn_3O_4 hausmannite and δ-MnO_2 structures, illustrating their common underlying face-centered-cubic oxygen framework, and similarity in octahedral Mn structure. The unique tetrahedral Mn sites in α-Mn_3O_4 are highlighted. **b.** Evolution of oxidation states of Mn and O as electrons are removed from the α-Mn_3O_4 model system. **c.** Schematic of the band structure of the activated catalyst system, derived from the "α-Mn_3O_4-3e$^-$" model. The T_d and O_h sections of the band diagram represent tetrahedral and octahedral Mn environments, while the Jahn-Teller orbital depicts the relative position of the O_h LUMO accounting for structural relaxation through Jahn-Teller distortion.

The catalysis mechanism underlying the superior performance of the activated δ-MnO_2 films (i.e., δ-MnO_2^{*3+}) can be understood by consideration of the electronic structure derived from the various local Mn-O ligand fields. Ex-situ PDF analysis reported previously[148] indicates that the activated δ-MnO_2^{*3+} catalyst comprises α-Mn_3O_4 hausmannite-like and δ-MnO_2 birnessite-like phases, and does not contain any other known crystalline MnO_2 polymorph phases. Both of these structures comprise face-centered-cubic oxygen frameworks with Mn occupying octahedral and tetrahedral interstitial sites[90], as illustrated in Figure 5-1a. Previously reported

XAS characterization[148] establishes the presence of Mn^{3+} or Mn^{4+} sites in the activated δ-MnO_2^{*3+} film. Understanding the effect of the Mn^{3+} on the electronic structure of δ-MnO_2^{*3+} is thus key to revealing the source of superior catalytic activity.

While the exact structure of an amorphous film is not amenable to a precise atomistic description, electronic behavior of the activated catalyst can be modeled by electronic titration of hausmannite α-Mn_3O_4 from its initial $Mn^{2.66+}$ average oxidation state, to Mn^{4+}. As the α-Mn_3O_4 structure contains both the tetrahedral and octahedral Mn environments of interest, and no others, it provides a first-order approximation of the electronic structure of the catalyst, which can inform a discussion of the enhanced activity resulting from Mn^{3+} incorporation into a native Mn^{4+} oxidic lattice. Thus, oxidized α-Mn_3O_4 provides a tractable local environment model of the oxidized, partial tetrahedral structure of δ-MnO_2^{*3+}.

The oxidation behavior of this structural model, shown in Figure 5-1b, provides a picture of the relative stability of various oxidation states in the mixed tetrahedral/octahedral δ-MnO_2^{*3+} structure. From the initial hausmannite starting point, all tetrahedral Mn exists in the 2+ oxidation state whereas octahedral Mn exists in the 3+ oxidation state. The valence band is dominated by a tetrahedral $Mn^{2+}(T_d)$ state, while the octahedral manganese ions are in Jahn-Teller distorted, high-spin $Mn^{3+}(O_h)$ state, as expected for hausmannite[241]. As the structure is oxidized, electrons are removed from the high-energy tetrahedral Mn states forming tetrahedral $Mn^{3+}(T_d)$ alongside the octahedral $Mn^{3+}(O_h)$ states. The next oxidation step removes electrons from the octahedral manganese sites, forming $Mn^{4+}(O_h)$. Once 3 electrons per formula unit are removed from the Mn_3O_4 structure, all octahedral manganese are in the $Mn^{4+}(O_h)$ state, while all tetrahedral manganese ions are in the $Mn^{3+}(T_d)$ state. At this point the valence band is dominated by oxygen states, rather than tetrahedral $Mn^{3+}(T_d)$ states, indicating that the oxidation of tetrahedral $Mn^{3+}(T_d)$ is more difficult than that of oxygen. Consistent with this result, upon further oxidation, electrons are extracted from O2p orbitals, while the tetrahedral sites remain as $Mn^{3+}(T_d)$ (Figure 5-1b). Indeed, after the onset of oxygen oxidation, some of the octahedral Mn regains some $Mn^{3+}(O_h)$ character. Thus, with the observation of the energy ordering of a O valence band to higher energy than that of manganese valence bands, we conclude any tetrahedral Mn in the activated film would remain as $Mn^{3+}(T_d)$ even under highly oxidizing conditions, forcing oxygen electrons to the valence band edge even for an average Mn oxidation state below Mn^{4+}, as is observed in the in situ XAS data published elsewhere[242]

A schematic illustration of the electronic structure of the activated film, derived from the fully oxidized α-Mn_3O_4 structural model, is given in Figure 5-1c. Consistent with the results of the electronic titration calculation (Figure 5-1b), the highest occupied molecular orbital (HOMO) is dominated by O2p states, while the lowest unoccupied molecular orbital (LUMO) is comprised of antibonding states of tetrahedral $Mn^{3+}(T_d)$. Octahedral Mn is oxidized from $Mn^{3+}(O_h)$ to $Mn^{4+}(O_h)$ at a higher potential than that of the tetrahedral $Mn^{2+}/3+(T_d)$ transition; the origin of this order of oxidation potentials lies in the stabilization of octahedral $Mn^{3+}(O_h)$ by Jahn-Teller distortion. In the undistorted octahedral environment found with $Mn^{4+}(O_h)$ the unoccupied antibonding e_g state is shifted up in energy and lies above the LUMO of tetrahedral $Mn^{3+}(T_d)$. A more subtle effect on energy ordering arises from the impact of local tensile strain as adjacent tetrahedral and octahedral environments are oxidized. As $Mn^{3+}(T_d)$ states initially form from $Mn^{2+}(T_d)$, the average T_d Mn-O bond length decreases from 2.04 Åto 1.98 Å. Upon oxidation of the nearby octahedral environments to $Mn^{4+}(O_h)$, the strong Mn-O bonding in the octahedra stretches the bonds in the tetrahedral environment, increasing the average T_d Mn-O bond length to 2.16 Å. This local strain confers more ionic character to the T_d Mn-O interaction and lowers the energy of the antibonding T_d LUMO, further decreasing the energy gap between the occupied O2p states and unoccupied Mn states. This decrease in energy gap leads to a further facilitation of the OER, as these stabilized empty states accept the electrons released from reductive elimination of O_2.

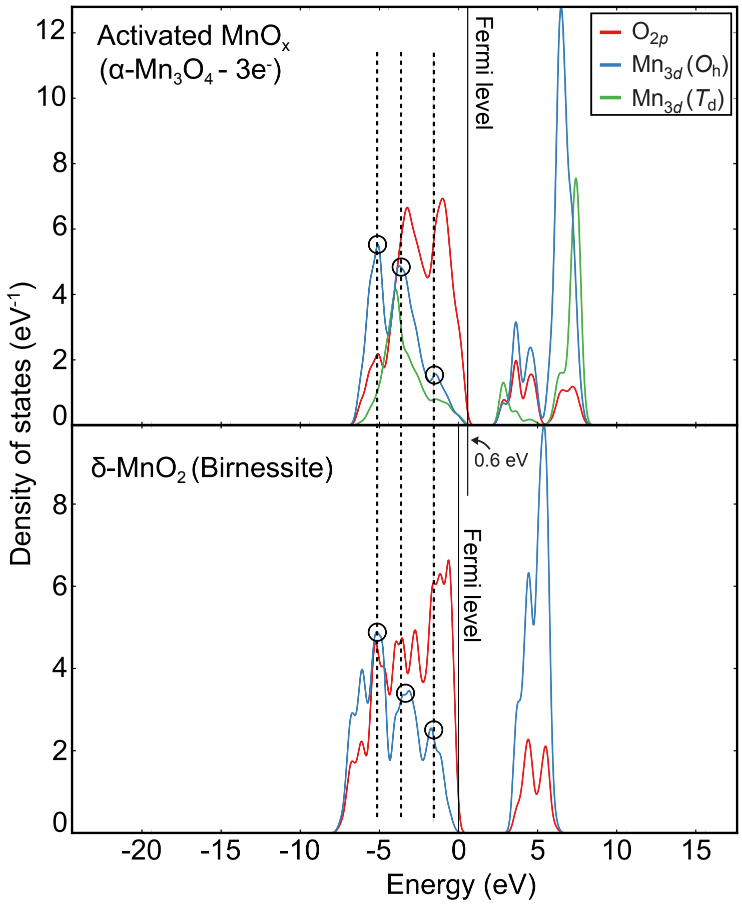

Figure 5-2: Band structure alignment between the activated catalyst model structure (α-Mn_3O_4-$3e^-$) and ideal δ-MnO_2 birnessite, based on the characteristic features of the $Mn^{4+}(O_h)$ environment present in both structures. The alignment reveals the presence of high-energy oxygen states in the activated catalyst structure, visible as an additional set of occupied oxygen states ranging up to 0.6 eV above the Fermi level of δ-MnO_2 birnessite.

An important feature of the electronic structure of the activated catalyst is the relative position of the HOMO oxygen band versus that of pure δ-MnO_2 birnessite. We align the band structures of the two structures using characteristic features of the $Mn^{4+}(O_h)$ environment present in both structures, effectively measuring the position of the occupied oxygen states with respect to the transition metal d-bands shared by both structures. Based on this alignment (Figure 5-2), we conclude that the activated catalyst contains higher energy oxygen states than pure δ-MnO_2 birnessite, with the oxygen band in the catalyst extending up to 0.6 eV above the Fermi level of birnessite. Note that while the absolute values of the HOMO-LUMO gaps may be overestimated by the computational methodology employed here, their relative values are reliable. The presence of these higher-energy oxygen states can be rationalized by the significant tensile strain experienced by oxygen bridging Mn^{3+} and Mn^{4+} environments, as this strain decreases the Mn-O orbital overlap and destabilizes the bonded state.

5.4 Impact of $Mn(T_d)$ on catalyst performance

The observation of tetrahedral Mn in the fully oxidized and activated δ-MnO_2^{*3+} film gives valuable insight into the electronic structure of the activated catalyst and provides a rationale for superior performance in the presence of Mn^{3+} in enhancing OER catalysis on MnO_2 polymorphs. Qualitatively, Mn^{3+} is well known to promote oxygen evolution [203, 243, 244, 245, 246], but has been difficult to isolate in neutral and acidic conditions[247]. Based on the Mn Pourbaix diagram[173], Mn_2O_3 and MnOOH may only be stable under alkaline conditions, while under acidic conditions, the only stable oxidation states of manganese are Mn^{2+} and Mn^{4+}. Correspondingly, Mn^{3+}, if formed within an oxide lattice, typically disproportionates to form Mn^{2+} and Mn^{4+} bellow pH 9 [247, 173, 248, 165]. One unique feature of our catalyst is that Mn in tetrahedral sites is kinetically trapped, and in a fully oxidized structure, the tetrahedral Mn is forced to remain as $Mn^{3+}(T_d)$. Indeed, in the oxidized δ-MnO_2^{*3+} film, where all octahedral Mn is fully oxidized to $Mn^{4+}(O_h)$ and tetrahedral Mn is fully oxidized to $Mn^{3+}(T_d)$, no disproportionation reaction is possible nor is it observed. This result is supported by the experimental XAS studies of the activated material[242] that show a persistent average Mn oxidation state of $Mn^{3.6+-3.8+}$, with only Mn^{3+} and Mn^{4+} in the fully oxidized film under anodic conditions.

The persistence of the metastable tetrahedral Mn species in the oxidized film is consistent with the migration behavior of Mn in rocksalt-derived oxides such as hausmannite and birnessite. Previous studies have found that Mn migration through the structure proceeds through hops between adjacent T_d and O_h sites. However, Mn^{2+} is the only species that is able to migrate between these T_d and O_h sites in the structure, while Mn^{3+} and Mn^{4+} are immobile[165, 249]. Thus, Mn^{3+} "migrates" only by disproportionating into Mn^{2+} and Mn^{4+}, after which the Mn^{2+} ion moves through the structure[250]. As no disproportionation reaction is possible in the fully oxidized δ-MnO_2^{*3+} film, we speculate that the Mn is kinetically locked in its metastable T_d site.

The role of the activation procedure described previously[203, 148] is to create kinetically stabilized, tetrahedral Mn^{3+} states. Each cathodic pulse results in a surface layer of Mn_3O_4, through the comproportionation of freshly-deposited $Mn(OH)_2$ with δ-MnO_2^{*3+} surface layers. Upon rapid, low-temperature oxidation through the electrochemical extraction of any protons or the partial redissolution of Mn, the film is unable to recrystallize into a typical, fully octahedral δ-MnO_2 structure, and maintains some Mn T_d character. These sites create $Mn^{3+}(T_d)$ states, immune to disproportionation, unlike other manganese oxides under acidic conditions.

The electronic structure of the activated film, shown in Figure 5-1c, suggests a mechanistic role for $Mn^{3+}(T_d)$ states in driving oxygen evolution through both the generation of reactive oxygen states, and a decreased HOMO-LUMO gap. The activated film has the general structure of a charge-transfer insulator, with the HOMO dominated by particularly weakly-bound O 2p states, while the LUMO consists of antibonding states within the $Mn^{3+}(T_d)$ environment. Such an electronic structure has been generally correlated to high oxygen evolution activity[251]. Mechanistically, in such a structure, electronic excitations create oxygen holes (Mn^{n}-O $\rightarrow$ Mn^{n-1}-O$\cdot$), forming highly reactive oxyl radicals, which are known to be critical intermediates in the PCET transformation of H_2O to O_2 [245, 252, 250, 253, 254, 255, 256], and in the proposal of reductive coupling [257, 258] and excess charging in Li batteries [259]. The generation of oxyl radicals resulting from a high lying O 2p valence band, with the population of oxygen radicals inversely proportional to the size of the HOMO-LUMO energy gap, is an emerging precept for the origin of enhanced OER activity in oxidic metal catalysts [260]. While pristine birnessite δ-MnO_2 has similar charge-transfer character to the activated film, the oxygen in δ-MnO_2 is significantly more bound than in the activated catalyst, as evidenced by the lower absolute energy of the oxygen band. Furthermore, the HOMO-LUMO gap is calculated to be between 2.8 and 3.4 eV, which results in a very small population of reactive oxygen radicals. In contrast, the metastable $Mn^{3+}(T_d)$ states of δ-MnO_2^{*3+} create low-lying metal states, with a calculated HOMO-LUMO gap of 1.9 eV, which can be further decreased by local tensile strains likely present around these tetrahedral sites.

The redox behavior of the activated δ-MnO_2^{*3+} material is similar to that observed in disordered Li-excess materials which have recently received significant attention as high-capacity cathodes for Li-ion batteries. The competition between $Mn^{3+/4+}$ and oxygen oxidation found in the δ-MnO_2^{*3+} catalyst is analogous to the activation of oxygen redox preferentially to transition metal oxidation in Li-excess cathodes[261, 257]. In both cases the redox behavior is controlled by unique local bonding environments, with strained metal-oxygen bonds in this material, and poorly hybridized Li-O-Li environments in Li-excess cathodes leading to the formation of reactive oxygen states[259, 262]. Similarly, transition metal oxidation is suppressed in both cases by constraining metal-oxygen bond lengths to that of the reduced state[263]. The result of these mechanisms is a promotion of oxygen evolution from the disordered, metastable material, which, while detrimental to reversible performance in Li-ion batteries, is the functional objective of an oxygen evolution catalyst.

5.5 Conclusion

To summarize, I have argued that metastable tetrahedral Mn resists oxidation to Mn^{4+} and thus promotes the evolution of oxygen from an activated δ-MnO_2^{*3+} catalyst. My collaborators and I have shown that the incorporation of Mn^{3+}, which typically disproportionates in oxide lattices, is enabled by the comproportionation of

Mn^{4+} in the form of MnO_2, and Mn^{2+} in the form of $Mn(OH)_2$. The kinetic trapping of Mn^{3+} is thus only possible via this comproportionation effect which requires the generation of OH^- and the presence of Mn^{2+}. Furthermore, we have shown that Mn^{3+} is stabilized in a T_d ligand field, introducing a local strain into the oxide lattice that produces a HOMO level primarily dominated by O 2p valence states and an unoccupied metal-based LUMO state with an attenuated HOMO-LUMO gap. These factors together contribute to enhanced OER activity by facilitating oxyl radical formation for reductive coupling to produce oxygen. More generally, the identification of a highly–strained, electrochemically active metastable local environment motivates a further exploration of similar metastable materials for catalysis applications.

Chapter 6

Concluding remarks

In this thesis, I have proposed, implemented, and validated a first–principles framework for evaluating the synthesizability of inorganic materials. I have sought to analyze synthesis from a quasi–thermodynamic perspective, with the hypothesis that phase selection in the formation of a solid is guided by local equilibrium. I have shown that it is possible to obtain the set of possible synthesis products, as well as the conditions required for the formation of each of them, from the ground states of a thermodynamic potential appropriately chosen to represent the synthesis reaction.

In chapter 2, I discussed the first–principles methods necessary to implement this quasi–thermodynamic scheme with sufficient accuracy. I identified and benchmarked the new strongly–constrained and appropriately–normed (SCAN) meta–GGA exchange–correlation functional as uniquely well suited for the computation of structure–sensitive thermodynamics. Furthermore, I developed a thermodynamic referencing scheme for SCAN in order to alleviate errors in transition metal electron transfer inherent to a non–empirical semi–local functional, establishing a general method providing sufficiently accurate thermochemistry for the analysis of synthesis.

In chapters 3 and 4, I proceeded to validate the quasi–thermodynamic picture of synthesis by rationalizing known synthesis recipes for the polymorphs of FeS_2 and MnO_2, obtained through hydrothermal growth. I demonstrated that phase selection in these two systems can be rationalized by considering the quasi–thermodynamic effect of finite–size stability, controlled by adsorption of spectator–ions from solution, and bulk off–stoichiometry. Finally, I confirmed that the joint effect of finite–size stability and bulk off–stoichiometry yields an accurate prediction of synthesis pathways and outcomes in two new manganese oxide syntheses.

Finally, in chapter 5, I provided an example of unique materials functionality enabled by metastability. Analyzing a recently reported manganese oxide oxygen evolution catalyst, I showed that the high catalytic activity observed originates from metastable tetrahedral Mn^{3+} ions retained in the structure from a reduced spinel–type precursor phase. The unique electronic structure provided by these metastable local environments suggest both a new direction in the development of oxygen evolution catalysts, and motivates the further development of metastable materials as unique functional materials.

A remaining issue in this analysis of synthesis is the question of kinetic phase retention once the system evolves outside of a given phase' region of stability. A closely related question is that of kinetic obstacles to the formation of locally stable phases, as observed in chapter 4. Taking the view of a reaction system evolving from precursor to product along some reaction coordinate, and a local minimization of its free energy, an equivalent formulation of these questions is how do kinetic obstacles to phase transformation map to the the energy along the reaction coordinate and affect the accessible degrees of freedom for local relaxation. While this question may be addressed directly through molecular dynamics or constrained migration simulations, these methods can only provide case-by-case insight at a significantly lower throughput than the quasi–thermodynamic analysis developed here. Thus, an alternative, more robust approach to the question of kinetic limitations is necessary. For example, diffusion–limited growth may potentially be modeled as a modification in the local chemical potential of the diffusion–limited specie, or may correspond to a constraint on local structure and composition as in the example discussed in chapter

5. Resolving these truly kinetic features in a scalable quasi–thermodynamic manner would complete the broad analysis of synthesizeability described in this thesis, and allow for quantitatively–accurate computational synthesis prediction.

Appendix A

Reference data for benchmaking the SCAN functional

Table S1: Formation enthalpy (eV/atom) of main group compounds

System	Experiment[95]	PBE	SCAN	PBE error	SCAN error
AlAs	-0.61	-0.487	-0.595	-0.12	-0.01
$AlCl_3$	-1.82	-1.51	-1.783	-0.31	-0.04
AlF_3	-3.90	-3.552	-4.113	-0.35	0.21
AlN	-1.61	-1.409	-1.728	-0.20	0.12
Al_2O_3	-3.47	-3.017	-3.504	-0.45	0.03
Al_2S_3	-1.50	-1.061	-1.233	-0.44	-0.27
Al_2Se_3	-1.18	-0.846	-0.981	-0.33	-0.20
Al_2Te_3	-0.68	-0.451	-0.496	-0.23	-0.18
BaO	-2.86	-2.481	-2.829	-0.38	-0.03
BaO_2	-2.19	-1.853	-2.124	-0.34	-0.07
BaS	-2.38	-2.081	-2.352	-0.30	-0.03
BeO	-3.14	-2.762	-3.215	-0.38	0.08
BeS	-1.21	-1.061	-1.338	-0.15	0.13
Be_3N_2	-1.22	-1.078	-1.399	-0.14	0.18
$CaCl_2$	-2.75	-2.403	-2.725	-0.35	-0.03
CaF_2	-4.21	-3.900	-4.456	-0.31	0.25
CaO	-3.29	-2.968	-3.353	-0.32	0.06
CaS	-2.45	-2.155	-2.432	-0.30	-0.02
GaAs	-0.37	-0.352	-0.374	-0.02	0.00
$GaCl_3$	-1.36	-1.111	-1.272	-0.25	-0.09

GaF_3	-3.01	-2.609	-3.076	-0.40	0.07
GaN	-0.81	-0.480	-0.655	-0.33	-0.16
GaS	-1.09	-0.652	-0.699	-0.44	-0.39
GaSb	-0.22	-0.165	-0.153	-0.06	-0.07
GaSe	-0.83	-0.595	-0.606	-0.24	-0.22
Ga_2O_3	-2.26	-1.858	-2.187	-0.40	-0.07
Ga_2S_3	-1.07	-0.664	-0.746	-0.41	-0.32
Ga_2Se_3	-0.85	-0.589	-0.632	-0.26	-0.22
GeS	-0.39	-0.333	-0.222	-0.06	-0.17
GeSe	-0.48	-0.249	-0.171	-0.23	-0.31
InAs	-0.31	-0.249	-0.317	-0.06	0.01
InN	-0.10	0.082	-0.109	-0.18	0.01
InS	-0.70	-0.509	-0.646	-0.19	-0.05
InSb	-0.16	-0.131	-0.174	-0.03	0.01
InTe	-0.50	-0.298	-0.308	-0.20	-0.19
In_2O_3	-1.92	-1.600	-1.952	-0.32	0.03
In_2S_3	-0.74	-0.557	-0.692	-0.18	-0.05
KC	-2.26	-1.964	-2.236	-0.30	-0.02
KF	-2.94	-2.699	-3.097	-0.24	0.16
KSb	-0.43	-0.443	-0.53	0.01	0.10
KSb_2	-0.37	-0.304	-0.354	-0.07	-0.02
K_2O	-1.25	-1.031	-1.27	-0.22	0.02
K_2O_2	-1.28	-1.066	-1.259	-0.21	-0.02
K_2S	-1.31	-1.068	-1.253	-0.24	-0.06
K_2S_2	-1.12	-0.940	-1.103	-0.18	-0.02
K_2Se	-1.36	-1.110	-1.284	-0.25	-0.08
K_3As	-0.48	-0.335	-0.439	-0.15	-0.04
K_3Bi	-0.60	-0.382	-0.460	-0.22	-0.14
K_3Sb	-0.47	-0.418	-0.507	-0.05	0.04
K_5Sb_4	-0.44	-0.444	-0.53	0.00	0.09
LiCl	-2.12	-1.816	-2.095	-0.30	-0.03
LiF	-3.19	-2.923	-3.37	-0.27	0.18
Li_2O	-2.07	-1.837	-2.113	-0.23	0.04
Li_2O_2	-1.64	-1.416	-1.636	-0.22	0.00
Li_2S	-1.52	-1.341	-1.527	-0.18	0.01
Li_2Se	-1.45	-1.267	-1.436	-0.18	-0.01
Li_3Bi	-0.60	-0.535	-0.601	-0.06	0.00
Li_3N	-0.43	-0.369	-0.510	-0.06	0.08
Li_3Sb	-0.83	-0.637	-0.699	-0.19	-0.13
$MgCl_2$	-2.21	-1.864	-2.161	-0.35	-0.05
MgF_2	-3.88	-3.550	-4.053	-0.33	0.17
MgO	-3.11	-2.715	-3.121	-0.40	0.01
MgS	-1.79	-1.433	-1.658	-0.36	-0.13
MgSe	-1.52	-1.257	-1.440	-0.26	-0.08
MgTe	-1.08	-0.879	-0.991	-0.20	-0.09

Mg_3Bi_2	-0.32	-0.208	-0.266	-0.11	-0.05
Mg_3Sb_2	-0.49	-0.370	-0.415	-0.12	-0.08
NaCl	-2.13	-1.813	-2.098	-0.32	-0.03
NaF	-2.97	-2.700	-3.137	-0.27	0.17
NaSb	-0.33	-0.333	-0.404	0.00	0.07
$NaTe_3$	-0.35	-0.388	-0.473	0.04	0.12
Na_2O	-1.43	-1.219	-1.476	-0.21	0.05
Na_2O_2	-1.32	-1.077	-1.293	-0.24	-0.03
Na_2S	-1.26	-1.074	-1.271	-0.19	0.01
Na_2S_2	-1.03	-0.833	-1.003	-0.20	-0.03
Na_2Se	-1.18	-1.074	-1.257	-0.11	0.08
Na_2Se_2	-0.97	-0.834	-0.994	-0.14	0.02
Na_3As	-0.53	-0.423	-0.528	-0.11	0.00
Na_3Bi	-0.46	-0.384	-0.452	-0.08	-0.01
Na_3Sb	-0.53	-0.441	-0.523	-0.09	-0.01
RbCl	-2.26	-1.952	-2.217	-0.31	-0.04
RbF	-2.89	-2.639	-3.036	-0.25	0.15
RbSb	-0.52	-0.433	-0.523	-0.09	0.00
$RbSb_2$	-0.35	-0.304	-0.354	-0.05	0.00
Rb_2O	-1.17	-0.919	-1.164	-0.25	-0.01
Rb_2S	-1.25	-1.009	-1.198	-0.24	-0.05
Rb_3Sb	-0.45	-0.365	-0.459	-0.09	0.01
SiO_2	-3.13	-2.980	-3.195	-0.15	0.07
SiS_2	-0.88	-0.657	-0.748	-0.22	-0.13
$SiSe_2$	-0.61	-0.376	-0.493	-0.23	-0.12
SnO	-1.48	-1.290	-1.412	-0.19	-0.07
SnO_2	-1.97b	-1.652	-1.976	-0.32	0.01
SnS	-0.57	-0.443	-0.417	-0.13	-0.15
SnS_2	-0.53	-0.379	-0.419	-0.15	-0.11
SnSe	-0.47	-0.436	-0.365	-0.03	-0.10
$SnSe_2$	-0.43	-0.348	-0.353	-0.08	-0.08
SrO	-3.07	-2.739	-3.117	-0.33	0.05
SrO	-2.19	-1.892	-2.177	-0.30	-0.01
SrS	-2.45	-2.151	-2.439	-0.30	-0.01
Sr_2Bi	-1.08	-0.761	-0.867	-0.32	-0.21
Sr_2Sb	-1.11	-0.864	-0.970	-0.25	-0.14
MAE				0.217	0.084

Table S2: Formation enthalpy (eV/atom) of transition metal compounds

System	Experiment[95]	PBE	SCAN	PBE error	SCAN error
AgO	-0.06	-0.107	-0.265	0.05	0.20

Ag_2O	-0.11	-0.096	-0.189	-0.01	0.08
Ag_2S	-0.11	-0.062	-0.069	-0.05	-0.04
Ag_2Se	-0.15	-0.079	-0.079	-0.07	-0.07
$CdCl_2$	-1.35	-1.097	-1.322	-0.25	-0.03
CdF_2	-2.42	-2.159	-2.654	-0.26	0.23
CdO	-1.34	-1.031	-1.325	-0.31	-0.02
CdS	-0.78	-0.643	-0.736	-0.14	-0.04
CdSb	-0.07	-0.051	-0.062	-0.02	-0.01
CdSe	-0.75	-0.633	-0.692	-0.12	-0.06
CdTe	-0.48	-0.464	-0.477	-0.02	0.00
Cd_3As_2	-0.08	-0.103	-0.114	0.02	0.03
CoF_2	-2.39	-1.702	-2.137	-0.69	-0.25
CoF_3	-2.10	-1.712	-1.901	-0.39	-0.20
CoO	-1.23	-0.672	-0.909	-0.56	-0.32
CoS	-0.43	-0.273	-0.146	-0.16	-0.28
$CoSb_3$	-0.17	-0.192	-0.156	0.02	-0.01
CoSe	-0.32	-0.275	-0.176	-0.05	-0.14
Co_3O_4	-1.32	-0.987	-1.071	-0.33	-0.25
Co_3S_4	-0.53	-0.430	-0.350	-0.10	-0.18
CrN	-0.65	-0.343	-0.673	-0.31	0.02
CrO_2	-2.07	-1.900	-2.337	-0.17	0.27
CrS	-0.81	-0.468	-0.824	-0.34	0.01
Cr_2O_3	-2.36	-1.926	-2.392	-0.43	0.03
CuF_2	-1.88	-1.517	-1.891	-0.36	0.01
CuO	-0.82	-0.600	-0.791	-0.22	-0.03
CuS	-0.28	-0.199	-0.250	-0.08	-0.03
CuSe	-0.21	-0.137	-0.143	-0.07	-0.07
Cu_2O	-0.58	-0.414	-0.501	-0.17	-0.08
Cu_2Sb	-0.04	0.011	0.011	-0.05	-0.05
Cu_2Se	-0.21	0.013	0.030	-0.22	-0.24
Cu_2Te	0.07	0.086	0.098	-0.02	-0.03
Cu_3N	0.19	0.282	0.267	-0.09	-0.08
Cu_3Sb	-0.02	0.067	0.084	-0.09	-0.10
FeF_2	-2.46	-1.916	-2.443	-0.54	-0.02
FeO	-1.41	-0.877	-1.191	-0.53	-0.22
FeS	-0.52	-0.515	-0.365	-0.01	-0.15
FeSe	-0.39	-0.281	-0.100	-0.11	-0.29
Fe_2O_3	-1.71	-1.172	-1.155	-0.54	-0.56
Fe_3O_4	-1.66	-1.122	-1.706	-0.54	0.05
HfN	-1.91	-1.752	-1.982	-0.16	0.07
HfO_2	-3.95	-3.566	-4.026	-0.38	0.08
$HgCl_2$	-0.77	-0.605	-0.735	-0.17	-0.03
HgO	-0.47	-0.294	-0.427	-0.18	-0.04
HgS	-0.30	-0.135	-0.137	-0.17	-0.16
HgSe	-0.24	-0.215	-0.195	-0.03	-0.04

HgTe	-0.22	-0.171	-0.168	-0.05	-0.05
$LaCl_3$	-2.78	-2.414	-2.775	-0.37	0.00
LaN	-1.57	-1.33	-1.627	-0.24	0.06
LaS	-2.36	-2.17	-2.378	-0.19	0.02
La_2O_3	-3.72	-3.468	-3.876	-0.25	0.16
La_2S_3	-2.51	-2.201	-2.468	-0.31	-0.04
NbN	-1.22	-1.077	-1.249	-0.14	0.03
NbO_2	-2.75	-2.447	-2.785	-0.30	0.04
NiF_2	-2.25	-1.656	-1.98	-0.59	-0.27
NiO	-1.24	-0.472	-0.765	-0.77	-0.48
NiSb	-0.34	-0.273	-0.289	-0.07	-0.05
NiSe	-0.31	-0.287	-0.255	-0.02	-0.05
Ni_3S_2	-0.42	-0.374	-0.393	-0.05	-0.03
$PdCl_2$	-0.69	-0.482	-0.68	-0.21	-0.01
PdO	-0.44	-0.445	-0.754	0.01	0.31
PdS_2	-0.28	-0.268	-0.369	-0.01	0.09
PtO	-0.37	-0.242	-0.485	-0.13	0.12
PtO_2	-0.57	-0.465	-0.757	-0.11	0.19
PtS	-0.42	-0.411	-0.613	-0.01	0.19
PtS_2	-0.38	-0.351	-0.494	-0.03	0.11
Pt_3O_4	-0.4	-0.440	-0.690	0.04	0.29
ScAs	-1.39	-1.375	-1.521	-0.01	0.13
$ScCl_3$	-2.40	-2.125	-2.427	-0.28	0.03
ScF_3	-4.22	-3.931	-4.469	-0.29	0.25
Sc_2O_3	-3.94	-3.559	-4.002	-0.38	0.06
TiAs	-0.78	-0.926	-1.017	0.15	0.24
$TiCl_4$	-1.7	-1.597	-1.812	-0.1	0.11
TiN	-1.58	-1.723	-1.996	0.14	0.42
TiO_2	-3.26	-3.048	-3.487	-0.21	0.23
TiS	-1.41	-1.427	-1.552	0.02	0.14
TiS_2	-1.41	-1.280	-1.459	-0.13	0.05
Ti_2O_3	-3.15	-2.896	-3.307	-0.25	0.16
VN	-1.13	-0.976	-1.149	-0.15	0.02
VO_2	-2.47	-2.346	-2.742	-0.12	0.27
YAs	-1.68	-1.553	-1.753	-0.13	0.07
YCl_3	-2.59	-2.290	-2.612	-0.30	0.02
YF_3	-4.45	-4.112	-4.726	-0.34	0.28
$ZnCl_2$	-1.43	-1.149	-1.339	-0.28	-0.09
ZnF_2	-2.64	-2.318	-2.751	-0.32	0.11
ZnO	-1.81	-1.445	-1.728	-0.37	-0.08
ZnS	-1.07	-0.811	-0.921	-0.26	-0.15
ZnSb	-0.08	-0.032	-0.015	-0.05	-0.06
ZnSe	-0.85	-0.716	-0.780	-0.13	-0.07
ZnTe	-0.61	-0.470	-0.475	-0.14	-0.14
Zn_3As_2	-0.28	-0.144	-0.123	-0.14	-0.16

Zn_3N_2	-0.05	0.114	-0.034	-0.16	-0.02
ZrN	-1.89	-1.683	-2.009	-0.21	0.12
ZrO_2	-3.80	-3.360	-3.939	-0.44	0.14
ZrS_2	-1.96	-1.519	-1.760	-0.44	-0.20
MAE				0.204	0.122

Table S3: Structure selection in ionic binary compounds

Legend

- PBE and SCAN energy values, where given, indicate the energy difference, in eV per atom, between the crystal structure preferred by the functional and that of the experimentally–reported ground state. In cases where no energy is given, the crystal structure chosen by the functional agrees with the experimentally–reported ground state.
- AB denotes an incorrect ground state in PBE only
- AB denotes an incorrect ground state in SCAN only
- AB denotes an incorrect ground state in PBE and SCAN
- Source: ICSD denotes only a single known structure in the ICSD

Chemistry	**PBE** (eV/at.)	**SCAN** (eV/at.)	**Spacegroup**	**ICSD ID**	**Source**
			Main group compounds		
Al_2O_3			R$\bar{3}$c	9770 (+80 others)	[121]
Al_2S_3	-0.002	-0.003	P6_1	300213	[264]
Al_2Se_3			Cc	14373	[265]
AlAs			F$\bar{4}$3m	67784 (+7 others)	[266]
AlF_3			R32	30274 (+4 others)	[267]
AlN			P6_3mc	31169 (+21 others)	[268]
AlP			F$\bar{4}$3m	24490 (+6 others)	[266]
AlSb			F$\bar{4}$3m	24804 (+9 others)	[266]
AsS			P2_1/c	15238 (+11 others)	[269]
AsSe			P2_1/c	2056 (+5 others)	ICSD
$BaCl_2$	-0.024		Pnma	15705 (+3 others)	[270]
BaF_2			Fm$\bar{3}$m	41649 (+5 others)	[271]
BaI_2			Pnma	15707 (+2 other)	[271]
BaO			Fm$\bar{3}$m	26961 (+7 others)	[272, 273]
BaO_2			I4/mmm	24248 (+4 others)	[274]

BaS			$Fm\bar{3}m$	30240 (+6 others)	ICSD
BaSe			$Fm\bar{3}m$	43655 (+6 others)	[275]
$BaSe_3$			$P\bar{4}2_1m$	16359	[276]
BaTe			$Fm\bar{3}m$	29152 (+4 others)	[277]
$BaTe_2$			I4/mcm	75555 (+2 other)	ICSD
$BaTe_3$			$P\bar{4}2_1m$	36366	ICSD
$BeBr_2$			Ibam	92584	ICSD
BeF_2			$P6_222$	9481 (+3 others)	[278]
BeO			$P6_3mc$	15620 (+31 others)	[272, 273]
BeS			$F\bar{4}3m$	44724 (+3 others)	[273]
BeTe			$F\bar{4}3m$	53945 (+2 other)	[273]
Bi_2O_3			$P2_1/c$	2374 (+7 others)	[279]
Bi_2Te_3			$R\bar{3}m$	15753 (+6 others)	[280]
$BiCl_3$	-0.056	-0.009	$Pna2_1$	2866 (+2 other)	[281]
BiSe			$P\bar{3}m1$	20458 (+2 other)	[282]
BiTe			$P\bar{3}m1$	30525 (+4 others)	[283]
Ca_2As_3			P2/c	43876	ICSD
Ca_3N_2			Ia3	34678 (+5 others)	[284, 285, 286]
$CaBr_2$	-0.021	-0.007	Pnnm	14220 (+11 others)	[287]
$CaCl_2$		-0.002	Pnnm	26158 (+6 others)	[287]
CaF_2			$Fm\bar{3}m$	28730 (+19 others)	[252]
CaI_2			$P\bar{3}m1$	52280	ICSD
CaO			$Fm\bar{3}m$	26959 (+13 others)	[288, 273]
CaS			$Fm\bar{3}m$	28902 (+16 others)	ICSD
CaSe			$Fm\bar{3}m$	41957 (+7 others)	[266]
CaTe			$Fm\bar{3}m$	41958 (+5 others)	[266]
Cs_2O			$R\bar{3}m$	27919	ICSD
Cs_3As			$P6_3cm$	409668	ICSD
CsBr	-0.040		$Pm\bar{3}m$	22174 (+4 others)	[289]
CsCl	-0.048		$Pm\bar{3}m$	22173 (+6 others)	[289]
CsF			$Fm\bar{3}m$	44288 (+2 other)	[289]
CsI	-0.032		$Pm\bar{3}m$	44291 (+8 others)	[289]
Ga_2O_3	-0.005	-0.017	C2/m	34243 (+4 others)	[290]
Ga_2S_3			Cc	488 (+3 others)	[291]
Ga_2Se_3			Cc	35028 (+3 others)	ICSD
GaAs			$F\bar{4}3m$	41674 (+24 others)	[266]
GaN			$P6_3mc$	25676 (+19 others)	[266]
GaP			$F\bar{4}3m$	41676 (+17 others)	[266]
GaSb			$F\bar{4}3m$	41675 (+14 others)	[266]
GaSe			$P\bar{6}m2$	71082 (+4 others)	[292, 293]
Ge_3N_4	-0.004		$P6_3/m$	23672	[294, 295, 296]
GeO_2			$P4_2/mnm$	9162 (+22 others)	[297]
GeSe	-0.011	-0.004	Pnma	17006 (+9 others)	[298]
$GeSe_2$			$P2_1/c$	614	[299]
GeTe			R3m	43202 (+25 others)	[300]

In_2S_3			$I4_1/amd$	23844 (+3 others)	[301]
In_2Te_3			$F\bar{4}3m$	180867 (+7 others)	[302]
In_3Te_4			$R\bar{3}m$	44655	ICSD
InAs			$F\bar{4}3m$	24518 (+22 others)	[266]
InN			$P6_3mc$	25677 (+9 others)	[266]
InP			$F\bar{4}3m$	24517 (+13 others)	[266]
InSb			$F\bar{4}3m$	24519 (+25 others)	[266]
InTe	-0.013	-0.020	I4/mcm	606 (+8 others)	[303, 304]
K_2O			$Fm\bar{3}m$	44674 (+4 others)	ICSD
K_2O_2			Cmce	25527 (+3 others)	ICSD
K_2S			$Fm\bar{3}m$	26735 (+3 others)	[305]
K_2Se			$Fm\bar{3}m$	60440 (+2 other)	ICSD
K_2Te			$Fm\bar{3}m$	60441 (+4 others)	ICSD
K_2Te_3			Pnma	2453 (+2 other)	ICSD
KBr			$Fm\bar{3}m$	18015 (+6 others)	[266]
KCl			$Fm\bar{3}m$	18014 (+37 others)	[266]
KF			$Fm\bar{3}m$	52241 (+3 others)	[266]
KI			$Fm\bar{3}m$	22158 (+5 others)	[266]
KSe			$P\bar{6}2m$	73172	ICSD
Li_2In			Cmcm	51961	ICSD
Li_2O			$Fm\bar{3}m$	22402 (+11 others)	[306]
Li_2O_2			$P6_3/mmc$	25530 (+3 others)	[307]
Li_2S			$Fm\bar{3}m$	54396 (+7 others)	[308]
Li_2Sb			$P\bar{6}2c$	100020	ICSD
Li_2Se			$Fm\bar{3}m$	60433 (+5 others)	ICSD
Li_2Te			$Fm\bar{3}m$	60434 (+3 others)	ICSD
Li_3As			$P6_3/mmc$	26878 (+3 others)	[309]
Li_3Bi			$Fm\bar{3}m$	58797 (+2 other)	[310]
Li_3N	-0.008		P6/mmm	34280 (+20 others)	[311]
Li_3Sb		-0.007	$Fm\bar{3}m$	44900 (+2 other)	[310]
LiBr			$P6_3mc$		[312]
LiCl	-0.025		$Fm\bar{3}m$	26909 (+5 others)	ICSD
LiF	-0.006		$Fm\bar{3}m$	18012 (+8 others)	ICSD
LiI			$P6_3mc$	414242	[313]
LiO_2			Pnnm	180561	ICSD
LiPb			$Pm\bar{3}m$	104762 (+4 others)	ICSD
LiSi			$I4_1/a$	78364 (+4 others)	[309]
LiTl			$Pm\bar{3}m$	104789 (+4 others)	[314]
$MgBr_2$			$P\bar{3}m1$	52366 (+3 others)	ICSD
$MgCl_2$			$R\bar{3}m$	26157 (+3 others)	[315]
MgF_2			$P4_2/mnm$	394 (+22 others)	[316]
MgI_2			$P\bar{3}m1$	52279 (+2 other)	ICSD
MgO			$Fm\bar{3}m$	9863 (+51 others)	[266, 273]
MgS			$Fm\bar{3}m$	28903 (+10 others)	[317, 273]
MgSe	-0.020	-0.017	$Fm\bar{3}m$	53946	[273]

MgTe			$P6_3mc$	52363 (+4 others)	[266, 273]
Na_2In			$C222_1$	106857	ICSD
Na_2O			$Fm\bar{3}m$	60435 (+3 others)	ICSD
Na_2O_2			$P\bar{6}2m$	25526 (+4 others)	ICSD
Na_2S			$Fm\bar{3}m$	56024 (+5 others)	[318]
Na_2S_5			Pnma	38349	ICSD
Na_2Se			$Fm\bar{3}m$	54281 (+5 others)	ICSD
Na_2Te			$Fm\bar{3}m$	60437 (+4 others)	ICSD
Na_3As			$P6_3cm$	79586 (+6 others)	[319]
Na_3Bi	-0.002	-0.002	$P6_3/mmc$	26881	[320]
Na_3P			$P6_3/mmc$	26884 (+3 others)	[321]
Na_3Sb			$P6_3/mmc$	26882	[320]
NaBi			P4/mmm	58816 (+2 other)	ICSD
NaBr			$Fm\bar{3}m$	18013 (+7 others)	[266]
NaCl			$Fm\bar{3}m$	18189 (+25 others)	[266]
NaF			$Fm\bar{3}m$	29128 (+8 others)	ICSD
NaGe			$P2_1/c$	43275	ICSD
NaI			$Fm\bar{3}m$	44279 (+6 others)	[266]
NaO_2	-0.001	-0.001	Pnnm	26583 (+5 others)	[322]
NaO_3			Imm2	85587 (+3 others)	ICSD
NaP		-0.005	$P2_12_12_1$	14009	[323]
NaPb			$I4_1/acd$	105156	ICSD
NaS			$P6_3/mmc$	43407 (+3 others)	[324]
NaS_2			$I\bar{4}2d$	2586	ICSD
NaSb			$P2_1/c$	26473	ICSD
NaSe			$P6_3/mmc$	43408	ICSD
$NaSe_2$			$I\bar{4}2d$	402584	ICSD
NaTe			Pbcn	61382	ICSD
NaTl			$Fd\bar{3}m$	105169 (+12 others)	[325]
P_2O_5	-0.005		Pnma	16611 (+4 others)	[326]
P_2S_5			$P\bar{1}$	23843 (+3 others)	ICSD
P_2Se_5			$P2_1/c$	74546	ICSD
P_4S_7			$P2_1/c$	23842 (+3 others)	ICSD
P_4Se_5			$Pna2_1$	16140	ICSD
PSe			$P2_1/c$	74878	ICSD
$PbBr_2$	-0.029		Pnma	36170	ICSD
PbO			P4/nmm	15466 (+20 others)	[327]
PbSe			$Fm\bar{3}m$	38294 (+24 others)	[328]
Rb_2O	-0.003		$Fm\bar{3}m$	77676 (+3 others)	ICSD
Rb_2S	-0.159		$Fm\bar{3}m$	29208	[329]
RbBr			$Fm\bar{3}m$	18017 (+5 others)	[266]
RbCl			$Fm\bar{3}m$	18016 (+8 others)	[328]
RbF			$Fm\bar{3}m$	53828	[266]
RbI			$Fm\bar{3}m$	22168 (+5 others)	[266]
Sb_2O_5			C2/c	1422 (+2 other)	[330]

Sb_2S_3			Pnma	22176 (+25 others)	[331]
Sb_2Te_3			$R\bar{3}m$	2084 (+3 others)	[332]
SbO_2		-0.002	Pnna	919 (+6 others)	[333, 334]
SeCl			$P2_1/c$	37018	ICSD
SeO_2			$P4_2/mbc$	24022 (+7 others)	[335]
SeO_3			$P\bar{4}2_1c$	18180	[336]
SiC			$F\bar{4}3m$	24217 (+9 others)	[337, 338]
SiO_2	-0.011		$P3_221$	174 (+138 others)	[339]
Sn_3N_4			$Fd\bar{3}m$	89525	ICSD
$SnBr_2$	-0.003		Pnma	411177	ICSD
$SnCl_2$			Pnma	15452 (+2 other)	[340]
SnF_2	-0.002		C2/c	308 (+3 others)	[341]
SnF_3			$Fm\bar{3}m$	33786	ICSD
SnI_2	-0.034	-0.013	C2/m	2831	ICSD
SnO			P4/nmm	15516 (+5 others)	[327]
SnO_2			$P4_2/mnm$	9163 (+29 others)	[342]
SnS			Pnma	24376 (+18 others)	[343]
SnSe			Pnma	16997 (+32 others)	[343]
$SnSe_2$			$P\bar{3}m1$	43594 (+6 others)	[344]
SnTe			$Fm\bar{3}m$	52489 (+23 others)	[345]
$SrBr_2$	-0.014		P4/n	26092 (+2 other)	[346, 347]
$SrCl_2$			$Fm\bar{3}m$	18011 (+3 others)	ICSD
SrF_2			$Fm\bar{3}m$	40414 (+5 others)	[348]
SrI_2	-0.027	-0.008	Pbca	15101 (+4 others)	[347]
SrO			$Fm\bar{3}m$	26960 (+10 others)	[266, 273]
SrO_2	-0.029	-0.011	I4/mmm	24249 (+2 other)	[349]
SrS			$Fm\bar{3}m$	28900 (+16 others)	[266]
SrSe			$Fm\bar{3}m$	28901 (+4 others)	[266]
SrTe			$Fm\bar{3}m$	53950 (+3 others)	[266]
Te_2O_5			$P2_1$	2523	ICSD
Te_3As_2			C2/m	18208 (+3 others)	[350]
TeF_6			Pnma	67609 (+2 other)	ICSD
TeO_2	-0.011		$P4_12_12$	25706 (+10 others)	[351]
TeO_3	-0.022		$R\bar{3}c$	27019 (+4 others)	[352]
TePb			$Fm\bar{3}m$	38295 (+44 others)	[353]
TlBr	-0.043	-0.004	$Pm\bar{3}m$	44936 (+4 others)	[354]
TlCl	-0.043		$Pm\bar{3}m$	29107 (+5 others)	[354]
TlF	-0.007		Pbcm	16112 (+9 others)	[355]
TlI	-0.023		Cmcm	26761 (+8 others)	[354]
TlTe			I4/mcm	69027 (+7 others)	[356]

Compounds containing transition metals

AgBr	-0.041		$Fm\bar{3}m$	52246 (+8 others)	[266, 357]
AgCl	-0.028		$Fm\bar{3}m$	56538 (+5 others)	[266, 357]

AgF	-0.009	-0.012	$Fm\bar{3}m$	18008	[266]
AgI		-0.005	$F\bar{4}3m$	52361 (+11 others)	[357]
AgO	-0.036		$P2_1/c$	69095	[358]
AgSe	-0.092	-0.164	$F\bar{4}3m$	52601 (+2 other)	ICSD
AsRh			Pnma	42572 (+3 others)	ICSD
AsRu			Pnma	42577 (+2 other)	ICSD
$CdCl_2$			$R\bar{3}m$	30255 (+3 others)	ICSD
CdF_2			$Fm\bar{3}m$	28731 (+4 others)	ICSD
CdO			$Fm\bar{3}m$	24802 (+14 others)	[266, 273]
CdS			$P6_3mc$	31074 (+22 others)	[266, 359, 360, 273]
CdSe			$F\bar{4}3m$	41528 (+6 others)	[266, 360, 361, 273]
CdTe			$F\bar{4}3m$	31844 (+39 others)	[266, 360, 273]
CoAs			$Pna2_1$	15065 (+9 others)	[362]
CoN			$F\bar{4}3m$	79936 (+2 other)	ICSD
CoO	-0.206	-0.056	$Fm\bar{3}m$	9865 (+22 others)	[363]
CoP			Pnma	43249 (+4 others)	ICSD
CoS	-0.142	-0.073	$P6_3/mmc$	29305 (+6 others)	[364]
CoSb			$P6_3/mmc$	76118 (+11 others)	ICSD
CoSe	-0.129		$P6_3/mmc$	42541 (+8 others)	[365]
CrAs	-1.303		$P6_3/mmc$	1261	[366]
CrN	-0.030		$Fm\bar{3}m$	37412 (+9 others)	[367]
CrO	-0.279	-0.328	$Fm\bar{3}m$	61633 (+2 other)	ICSD
CrP			Pnma	42079 (+12 others)	ICSD
CrS		-0.027	P1	16718	[368]
CrSb			$P6_3/mmc$	53210 (+9 others)	ICSD
Cu_2Se	-0.093	-0.097	$Fm\bar{3}m$	56025	[369]
Cu_3N			$Pm\bar{3}m$	25675 (+14 others)	[370]
CuBr	-0.004		$F\bar{4}3m$	23989 (+5 others)	[371, 357]
CuCl	-0.016		$F\bar{4}3m$	23988 (+4 others)	[357]
CuI		-0.002	$F\bar{4}3m$	9098 (+12 others)	[371, 357, 372]
CuO			C2/c	69095	[358]
CuS			$P6_3/mmc$	26968 (+13 others)	[373]
CuSe	-0.005	-0.008	Cmcm	240 (+20 others)	[374]
CuTe			Pmmn	42591 (+5 others)	[375]
FeAs			Pnma	15009 (+16 others)	ICSD
FeN			$F\bar{4}3m$	41258	ICSD
FeO	-0.093	-0.077	$Fm\bar{3}m$	27856 (+14 others)	ICSD
FeP			$Pna2_1$	15057 (+7 others)	ICSD
FeS	-0.274	-0.077	$P6_3/mmc$	29302 (+5 others)	[364]
FeSb			$P6_3/mmc$	53535 (+3 others)	ICSD
FeSe			P4/nmm	26889 (+47 others)	[376]
FeTe			P4/nmm	44753 (+4 others)	[377]
HfN			$Fm\bar{3}m$	53025 (+16 others)	[378]
HgO			Pnma	14124 (+3 others)	[379]
HgS			$P3_121$	31129 (+8 others)	[380]

HgSe			$F\bar{4}3m$	24175 (+11 others)	[360, 273]
HgTe			$F\bar{4}3m$	31845 (+28 others)	[360, 273]
LaN	-0.012	-0.003	$Fm\bar{3}m$	44684 (+16 others)	[381, 382]
LaS			$Fm\bar{3}m$	29394 (+10 others)	[383]
MnAs	-0.035		$P6_3/mmc$	9497 (+9 others)	[384]
MnN	-0.052		$I4/mmm$	106932	[385]
MnO	-0.122	-0.039	$Fm\bar{3}m$	9864 (+14 others)	ICSD
MnP			Pnma	30412 (+12 others)	ICSD
MnS	-0.122	-0.052	$Fm\bar{3}m$	18007 (+24 others)	[386]
MnSb			$P6_3/mmc$	53970 (+22 others)	ICSD
MnSe	-0.144	-0.048	$Fm\bar{3}m$	24251 (+16 others)	[387]
MnTe	-0.107	-0.078	$P6_3/mmc$	43541 (+17 others)	[388]
MoAs	-0.001	-0.006	Pnma	43188 (+2 other)	ICSD
MoP			$P\bar{6}m2$	76367 (+4 others)	ICSD
NbAs			$I4_1md$	16585 (+3 others)	ICSD
NbN	-0.038	-0.043	$P6_3/mmc$	76384 (+3 others)	[389, 390, 391, 392]
NbP			$I4_1md$	76027 (+2 other)	ICSD
NiAs			$P6_3/mmc$	29303 (+6 others)	[393]
NiO			$Fm\bar{3}m$	9866 (+29 others)	ICSD
NiS		-0.085	R3m	29312 (+11 others)	[364]
NiSb			$P6_3/mmc$	29304 (+11 others)	ICSD
NiSe			$P6_3/mmc$	29310 (+10 others)	[394]
NiTe			$P6_3/mmc$	42557 (+8 others)	[395]
PRu			Pnma	109139 (+2 other)	ICSD
PdO			$P4_2/mmc$	24692 (+3 others)	[327]
PtO	-0.093	-0.188	$P4_2/mmc$	26599 (+2 other)	[327]
PtS			$P4_2/mmc$	31131 (+4 others)	ICSD
PtS_2			$P\bar{3}m1$	41375 (+6 others)	ICSD
SbRh			Pnma	991 (+4 others)	ICSD
SbRu			Pnma	990	ICSD
ScAs			$Fm\bar{3}m$	1331 (+4 others)	[396]
ScF_3			R32	36011 (+31 others)	[397]
ScN			$Fm\bar{3}m$	26948 (+7 others)	[398]
ScP			$Fm\bar{3}m$	77798 (+4 others)	[399]
ScSb			$Fm\bar{3}m$	1335 (+5 others)	[396, 400]
TaAs			$I4_1md$	44068 (+3 others)	[401]
TaN		-0.005	$P\bar{6}2m$	1396 (+5 others)	[402, 403]
TaP			$I4_1/amd$	108656	ICSD
TiAs			$P6_3/mmc$	16773 (+2 other)	[396]
TiN			$Fm\bar{3}m$	26947 (+26 others)	ICSD
TiO	-0.181	-0.202	$Fm\bar{3}m$	40125 (+10 others)	[404, 405]
TiP			$P6_3/mmc$	24337 (+2 other)	ICSD
TiS	-0.137	-0.155	$R\bar{3}m$	25561	[406, 407]
TiS_2			$P\bar{3}m1$	26861 (+16 others)	[408]
TiSb			$P6_3/mmc$	76406 (+2 other)	[409]

TiTe	-0.058	-0.018	$P6_3/mmc$	653080	[409]
VAs		-0.007	$Pna2_1$	42445 (+5 others)	[410]
VN	-0.191	-0.126	$Fm\bar{3}m$	22321 (+22 others)	[411]
VO	-0.075	-0.010	$Fm\bar{3}m$	28681 (+10 others)	[404, 412]
VP	-0.007		$P6_3/mmc$	42444 (+2 other)	[410]
VSb	-0.005		$P6_3/mmc$	23910	[413]
YAs			$Fm\bar{3}m$	44087 (+6 others)	[414]
YN			$Fm\bar{3}m$	37413 (+5 others)	[398]
YP			$Fm\bar{3}m$	77857 (+4 others)	[399]
YSb			$Fm\bar{3}m$	43632 (+6 others)	[400]
ZnO			$P6_3mc$	26170 (+56 others)	[266, 273]
ZnS			$F\bar{4}3m$	41985 (+19 others)	[266, 273]
ZnSe			$F\bar{4}3m$	41527 (+26 others)	[266, 273]
ZnTe			$F\bar{4}3m$	31843 (+19 others)	[266, 273]

Appendix B

Derivation of the reference entropy of ions in solution

First, consider H_3O^+ in a solution at a set pH. By the definition of pH, the chemical potential of H_3O^+ can be written as

$$\mu_{\mathrm{H_3O^+}} = \mu^0_{\mathrm{H_3O^+}} + k_{\mathrm{B}}T \log a_{\mathrm{H_3O^+}} = \mu^0_{\mathrm{H_3O^+}} - 2.3 k_{\mathrm{B}}T \text{ pH}$$

where the reference state chemical potential $\mu^0_{\mathrm{H_3O^+}}$ corresponds to a 1M solution of H_3O^+ at standard state conditions (temperature T_0). By the ideal solution model, this reference chemical potential can be written as

$$\mu^0_{\mathrm{H_3O^+}} = h_{\mathrm{H_3O^+}} + k_{\mathrm{B}}T_0 \ln \frac{1}{M_{\mathrm{w}}} = h_{\mathrm{H_3O^+}} - k_{\mathrm{B}}T_0 \ln M_{\mathrm{w}}$$

Thus, the chemical potential of H_3O^+ at any pH is given by

$$\mu_{\mathrm{H_3O^+}} = h_{\mathrm{H_3O^+}} - k_{\mathrm{B}}T_0 \ln M_{\mathrm{w}} - 2.3 k_{\mathrm{B}}T \text{ pH}$$

giving an entropy of

$$s_{\mathrm{H_3O^+}} = -\frac{\mu_{\mathrm{H_3O^+}} - h_{\mathrm{H_3O^+}}}{T} = k_{\mathrm{B}}\frac{T_0}{T}\ln M_{\mathrm{w}} + 2.3k_{\mathrm{B}}\ \mathrm{pH}$$

The chemical potential of OH^- is set by the equilibrium of H_3O^+, OH^- and H_2O:

$$\mu_{\mathrm{OH-}} = 2\mu_{\mathrm{H_2O}} - \mu_{\mathrm{H_3O^+}} = 2h_{\mathrm{H_2O}} - h_{\mathrm{H_3O^+}} + k_{\mathrm{B}}T_0\ln M_{\mathrm{w}} + 2.3k_{\mathrm{B}}T\ \mathrm{pH}$$

Once again, we can solve for the entropy of OH^- to yield:

$$s_{\mathrm{OH^-}} = -\frac{\mu_{\mathrm{OH^-}} - h_{\mathrm{OH^-}}}{T} = \frac{h_{\mathrm{OH^-}} + h_{\mathrm{H_3O^+}} - 2h_{\mathrm{H_2O}}}{T} - k_{\mathrm{B}}\frac{T_0}{T}\ln M_{\mathrm{w}} - 2.3k_{\mathrm{B}}\ \mathrm{pH} =$$

$$= \frac{\Delta h_{\mathrm{w}}^0}{T} - k_{\mathrm{B}}\frac{T_0}{T}\ln M_{\mathrm{w}} - 2.3k_{\mathrm{B}}\ \mathrm{pH}$$

Appendix C

Example calculation of surface energy accounting for adsorption

To illustrate the interplay between the terms introduced in the thermodynamic model and their relative importance, we derive the adsorbed surface energies for two example surfaces at pH 5.5.

In pyrite, under these conditions, we find that the dominant surface is (210), adsorbed with OH^- ions. The energy of the clean (210) surface is $E_{\mathrm{slab}}^{\mathrm{vac}}/2A = 1.82$ J m^{-2}, but this energy is significantly reduced by hydration and adsorption. The number and geometry of OH^- adsorption sites can be estimated from the “missing” S atoms which would have coordinated the Fe on the surface. These sites occur at a density of $N_{\mathrm{slab}}^{\mathrm{sites}} = 0.0787$ Å^{-2}. For each of these sites, the energy of mean–field H_2O adsorption is calculated to be $\Delta E_{\mathrm{slab}}^{\mathrm{solv}} = -0.596$ eV per site. The energy of the competing OH^- adsorption (at pH 5.5) is calculated to be $\Delta E_{\mathrm{OH^-}}^{\mathrm{ads},\infty} = -0.813$ eV per OH^-, where $\Delta E_{\mathrm{OH^-}}^{\mathrm{ads},\infty}$ accounts for adsorbate–solid interactions referenced to the chemical potential of the OH^- ion in solution at pH = 5.5, but not adsorbate–adsorbate interactions or configurational entropy. To find the total energy of the adsorbed surface, we minimize the total energy of the interface with respect to OH^- coverage, combining the properly referenced adsorbate–solid interactions in the form of $\Delta E_{\mathrm{OH^-}}^{\mathrm{ads},\infty} - \Delta E_{\mathrm{slab}}^{\mathrm{solv}} =$ -0.217 eV, the adsorbate–adsorbate interactions in the form of the Debye–Huckel term V^{el}, and the configurational entropy. We find that the optimum occurs at 9% coverage, where the Debye-Huckel repulsion contributes 0.140 eV per OH^-, and the entropy contributes -0.138 eV per OH^- at the preset 473K temperature. Put together, the adsorption lowers the surface energy by 0.024 J m^{-2} with respect to the pure hydrated surface (1.069 J m^{-2}), giving a final surface energy of 1.045 J m^{-2}.

In marcasite, one important OH^-–stabilized facet is the (110) surface. The vacuum energy of this surface is 1.66 J m^{-2}, brought down to 1.19 J m^{-2} by hydration. Following the same broken–bond–counting metric as before, we estimate the density of OH^- adsorption sites to be 0.086 Å^{-2}, with $\Delta E_{\mathrm{OH^-}}^{\mathrm{ads},\infty} - \Delta E_{\mathrm{slab}}^{\mathrm{solv}} =$ -0.770 eV per OH^-. We find that the optimal coverage is 16%, with the Debye-Huckel repulsion term contributing 0.333 eV per OH^- and configurational entropy contributing -0.111 eV per OH^-. Thus, OH^- adsorption lowers the surface energy by 0.124 J m^{-2}, yielding a final surface energy of 1.061 J m^{-2}.

Appendix D

Relaxed adsorption geometries for FeS_2 pyrite and marcasite

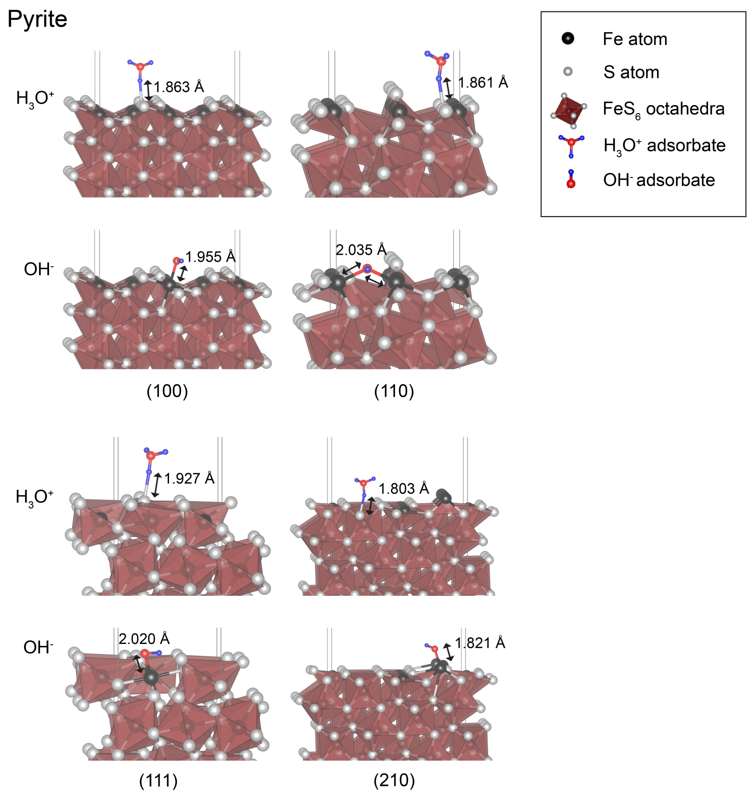

Figure D-1: **Relaxed dilute adsorption geometries on pyrite.** The relaxed geometries of H_3O^+ and OH^- adsorbed onto the major facets of FeS_2 pyrite. In all cases, the charge of the adsorbate is compensated by a countercharge in the vacuum, and replicated on the opposite side of the slab (not shown) to ensure that the calculation cell has no net dipole, following the calculation methodology described in the main text.

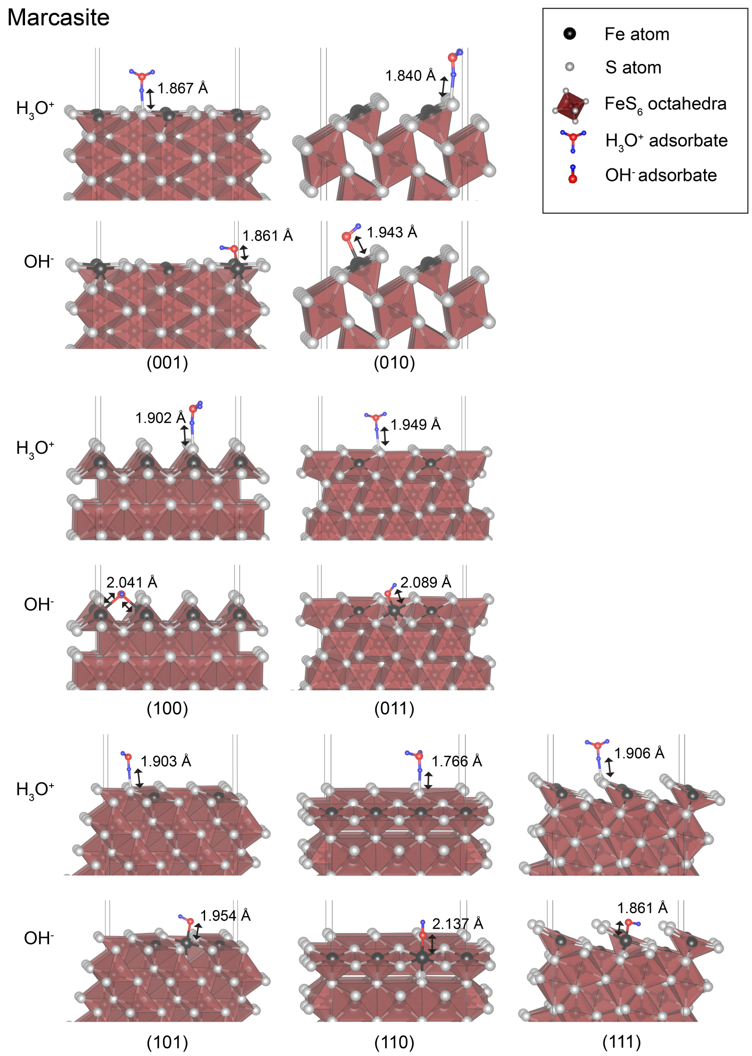

Figure D-2: **Relaxed dilute adsorption geometries on marcasite.** The relaxed geometries of H_3O^+ and OH^- adsorbed onto FeS_2 marcasite. In all cases, the charge of the adsorbate is compensated by a countercharge in the vacuum, and replicated on the opposite side of the slab (not shown) to ensure that the calculation cell has no net dipole, following the calculation methodology described in the main text.

Appendix E

Derivation of Mn-O aqueous chemical equilibria

We take the solution at a fixed pH, zero applied potential, and 298 K in equilibrium with the standard hydrogen electrode, which gives:

$$\mu_{\mathrm{H}^+} = -2.3 k_{\mathrm{B}} T \ \mathrm{pH}$$

$$\mu_{e^-} = 0$$

The stability maps in Figure 4 are then defined by the reactions:

$$(1)\ \mathrm{MnO_2} + x\mathrm{A}^+ + xe^- \rightarrow \mathrm{A}_x\mathrm{MnO_2}$$

$$(2)\ \mathrm{MnO_2} + x\mathrm{H}^+ + xe^- \rightarrow \mathrm{H}_x\mathrm{MnO_2}$$

$$(3)\ 3\mathrm{MnO_2} + 4\mathrm{H}^+ + 4e^- \rightarrow \mathrm{Mn_3O_4} + 2\mathrm{H_2O}$$

$$(4)\ \mathrm{MnO_2} + 4\mathrm{H}^+ + 2e^- \rightarrow \mathrm{Mn}^{2+}_{(aq)} + 2\mathrm{H_2O}$$

$$(5)\ \mathrm{MnO_2} + 2\mathrm{H_2O} \rightarrow \mathrm{MnO}^{-}_{4,(aq)} + 4\mathrm{H}^+ + 3e^-$$

The corresponding reaction energies, in terms of the Gibbs free energies of formation of the various components are:

$$\Delta G_1 = G^f_{\mathrm{A}_x\mathrm{MnO}_2} - G^f_{\mathrm{MnO}_2} - x\mu_{A^+}$$

$$\Delta G_2 = G^f_{\mathrm{H}_x\mathrm{MnO}_2} - G^f_{\mathrm{MnO}_2} + 2.3xk_{\mathrm{B}}T\ \mathrm{pH}$$

$$\Delta G_3 = G^f_{\mathrm{Mn}_3\mathrm{O}_4} - 3G^f_{\mathrm{MnO}_2} + 9.2k_{\mathrm{B}}T\ \mathrm{pH} + 2G^f_{\mathrm{H}_2\mathrm{O}}$$

$$\Delta G_4 = G^f_{\mathrm{Mn}^{2+}_{(aq)}} - G^f_{\mathrm{MnO}_2} + 9.2k_{\mathrm{B}}T\ \mathrm{pH} + 2G^f_{\mathrm{H}_2\mathrm{O}}$$

$$\Delta G_5 = G^f_{\mathrm{MnO}^-_{4,(aq)}} - G^f_{\mathrm{MnO}_2} - 9.2k_{\mathrm{B}}T\ \mathrm{pH} - 2G^f_{\mathrm{H}_2\mathrm{O}}$$

Appendix F

Thermal effects on MnO_2 and MnOOH polymorphism

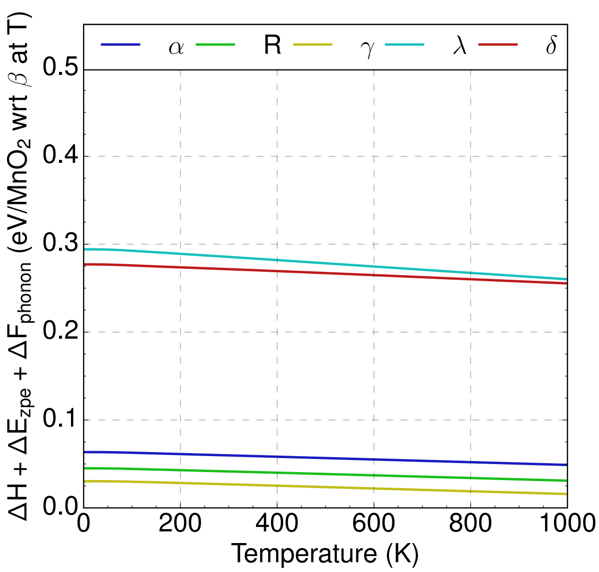

Figure F-1: The free energy of the R, γ, α, δ and λ – MnO_2 with respect to the β reference state, accounting for the DFT–derived enthalpy (ΔH), zero–point energy (ΔE_{zpe}), and phonon free energy (ΔF_{phonon}). Note that configurational entropy is not included as we assume zero defect concentration at the MnO_2 composition.

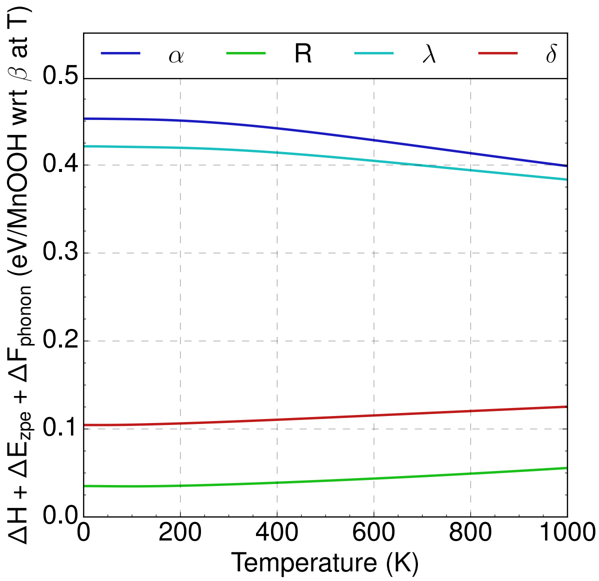

Figure F-2: The free energy of the ground state R, α, δ and λ –type MnOOH with respect to the β–type reference state, accounting for the DFT–derived enthalpy (ΔH), zero–point energy (ΔE_{zpe}), and phonon free energy (ΔF_{phonon}). Note that configurational entropy is not included as at the MnOOH composition, we assume the H–sublattice to be fully occupied.

Appendix G

Jahn-Teller distortions in Mn^{3+} compounds

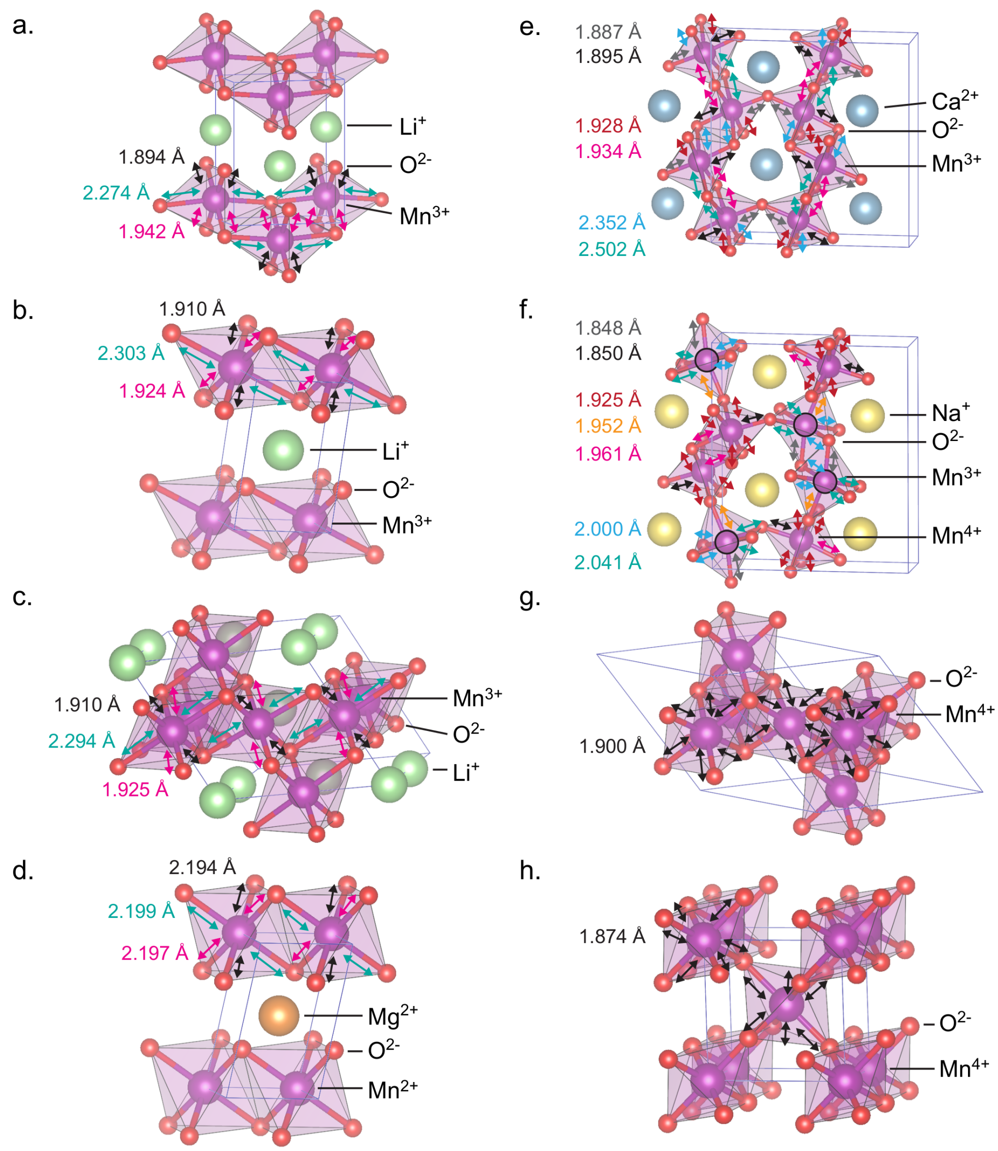

Figure G-1: Jahn-Teller distortions in several structures, illustrating bond length distortion in Mn^{3+} states in agreement with recent EXAFS results[188], and a relative lack of distortion in Mn^{2+} and Mn^{4+} states, as well as the relatively complex orderings that arise as a result of the distortion. **a.** Mn^{3+} distortions in the orthorhombic $LiMnO_2$ ground state structure as compared to the hypothetical metastable **b.** δ layered and **c.** λ spinel structures. **d.** Bond lengths in the δ $MgMnO_2$ phase illustrating a lack of distortions in Mn^{2+} states. **e.** Mn^{3+} Jahn-Teller induced ordering in marokite $CaMn_2O_4$. **f.** Charge and Jahn-Teller distortion ordering in the mixed valent Mn^{3+}-Mn^{4+} postspinel $NaMn_2O_4$ structure. Lack of asymmetric bonding in Jahn-Teller inactive Mn^{4+} phases: **g.** λ spinel and **h.** β pyrolusite.

Appendix H

Calibration of Hartree-Fock exchange fraction for MnO_2

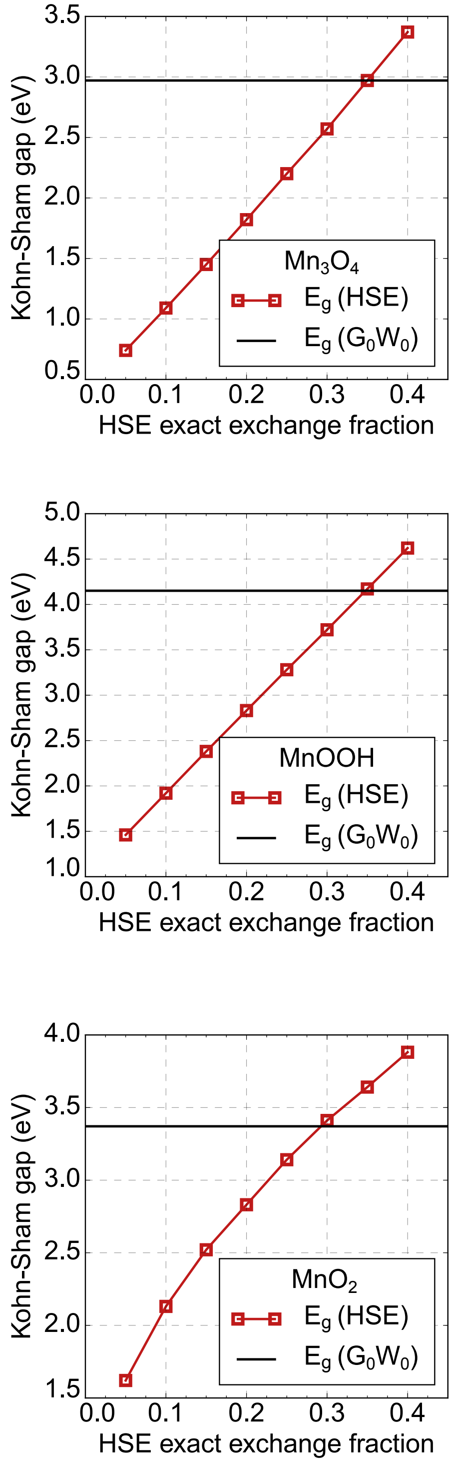

Figure H-1: Calibration of the fraction of Hartree–Fock exchange used in hybrid density functional theory calculations based on the band-gap obtained from a single shot G_0W_0 calculation.

Bibliography

[1] K. Capelle. A bird's-eye view of density-functional theory. *Brazilian Journal of Physics*, 36(4A):1318–1343, 2006.

[2] K. Burke. The ABC of DFT. *Department of Chemistry, University of California*, 2007.

[3] P. Hohenberg and W. Kohn. Inhomogeneous electron gas. *Physical review*, 136(3B):B864, 1964.

[4] W. Kohn and L. J. Sham. Self–consistent equations including exchange and correlation effects. *Phys. Rev.*, 140:A1133–A1138, 1965.

[5] G. Kresse and J. Furthmuller. Efficiency of ab-initio total energy calculations for metals and semiconductors using a plane-wave basis set. *Computational Materials Science*, 6(1):15 – 50, 1996.

[6] G. Kresse and J. Furthmuller. Efficient iterative schemes for *ab initio* total-energy calculations using a plane-wave basis set. *Phys. Rev. B*, 54:11169–11186, Oct 1996.

[7] D. Vanderbilt. Soft self-consistent pseudopotentials in a generalized eigenvalue formalism. *Physical Review B*, 41(11):7892, 1990.

[8] G. Kresse and D. Joubert. From ultrasoft pseudopotentials to the projector augmented-wave method. *Phys. Rev. B*, 59:1758–1775, 1999.

[9] J. P. Perdew, K. Burke, and M. Ernzerhof. Generalized Gradient Approximation Made Simple. *Physical review letters*, 77(18):3865–3868, 1996.

[10] C. Lee, W. Yang, and R. G. Parr. Development of the colle-salvetti correlation-energy formula into a functional of the electron density. *Physical review B*, 37(2):785, 1988.

[11] J. Sun, A. Ruzsinszky, and J. P. Perdew. Strongly Constrained and Appropriately Normed Semilocal Density Functional. *Phys. Rev. Lett.*, 115(3):036402, 2015.

[12] J. Sun, R. C. Remsing, Y. Zhang, Z. Sun, A. Ruzsinszky, H. Peng, Z. Yang, A. Paul, U. Waghmare, X. Wu, and J. P. Perdew. Accurate first-principles structures and energies of diversely bonded systems from an efficient density functional. *Nature chemistry*, 8(9):831–836, 2016.

[13] A. Jain, G. Hautier, C. J. Moore, S. P. Ong, C. C. Fischer, T. Mueller, K. A. Persson, and G. Ceder. A high-throughput infrastructure for density functional theory calculations. *Computational Materials Science*, 50(8):2295 – 2310, 2011.

[14] A. Jain, S. P. Ong, G. Hautier, W. Chen, W. D. Richards, S. T. Dacek, S. Cholia, D. Gunter, D. Skinner, G. Ceder, and K. A. Persson. The Materials Project: A materials genome approach to accelerating materials innovation. *APL Mater.*, 1(1):011002, 2013.

[15] S. Curtarolo, G. Hart, M. B. Nardelli, N. Mingo, S. Sanvito, and O. Levy. The high-throughput highway to computational materials design. *Nature Materials*, 12(3):191–201, 2013.

[16] A. Urban, D-H. Seo, and G. Ceder. Computational understanding of Li-ion batteries. *npj Computational Materials*, 2:16002, 2016.

[17] G. Hautier, C. C. Fischer, A. Jain, T. Mueller, and G. Ceder. Finding natureâĂŹs missing ternary oxide compounds using machine learning and density functional theory. *Chemistry of Materials*, 22(12):3762–3767, 2010.

[18] A. Jain, Y. Shin, and K. A. Persson. Computational predictions of energy materials using density functional theory. *Nature Reviews Materials*, 1:15004, 2016.

[19] A. Belsky, M. Hellenbrandt, V. L. Karen, and P. Luksch. New developments in the Inorganic Crystal Structure Database (ICSD): accessibility in support of materials research and design. *Acta Crystallographica Section B: Structural Science*, 58(3):364–369, 2002.

[20] C. C. Fischer, K. J. Tibbetts, D. Morgan, and G. Ceder. Predicting crystal structure by merging data mining with quantum mechanics. *Nature Materials*, 5(8):641–646, 2006.

[21] W. Sun, S. Jayaraman, W. Chen, K. A. Persson, and G. Ceder. Nucleation of metastable aragonite $CaCO_3$ in seawater. *Proceedings of the National Academy of Sciences*, 112(11):3199–3204, 2015.

[22] W. Sun, S. T. Dacek, S. P. Ong, G. Hautier, A. Jain, W. D. Richards, A. C. Gamst, K. A. Persson, and G. Ceder. The thermodynamic scale of inorganic crystalline metastability. *Science Advances*, 2(11):e1600225, 2016.

[23] M. R. Ranade, A. Navrotsky, H. Z. Zhang, J. F. Banfield, S. H. Elder, A. Zaban, P. H. Borse, S. K. Kulkarni, G. S. Doran, and H. J. Whitfield. Energetics of nanocrystalline TiO_2. *Proceedings of the National Academy of Sciences*, 99(suppl 2):6476–6481, 2002.

[24] A. Navrotsky. Nanoscale effects on thermodynamics and phase equilibria in oxide systems. *Chemphyschem : a European journal of chemical physics and physical chemistry*, 12(12):2207–15, 2011.

[25] J. Baumgartner, A. Dey, P. H. H. Bomans, C. Le Coadou, P. Fratzl, N. A. J. M. Sommerdijk, and D. Faivre. Nucleation and growth of magnetite from solution. *Nature Materials*, 12(4):310–314, 2013.

[26] A. R. Oganov and C. W. Glass. Crystal structure prediction using ab initio evolutionary techniques: Principles and applications. *The Journal of Chemical Physics*, 124(24), 2006.

[27] S. M. Woodley and R. Catlow. Crystal structure prediction from first principles. *Nature materials*, 7(12):937–946, 2008.

[28] D. Spagnoli, K. Refson, K. Wright, and J. D. Gale. Density functional theory study of the relative stability of the iron disulfide polymorphs pyrite and marcasite. *Physical Review B*, 81(9):094106, 2010.

[29] M. T. Curnan and J. R. Kitchin. Investigating the energetic ordering of stable and metastable tio2 polymorphs using dft+u and hybrid functionals. *The Journal of Physical Chemistry C*, 119(36):21060–21071, 2015.

[30] S. Curtarolo, D. Morgan, and G. Ceder. Accuracy of ab initio methods in predicting the crystal structures of metals: A review of 80 binary alloys. *Calphad*, 29(3):163 – 211, 2005.

[31] J. P. Perdew, A. Ruzsinszky, G. I. Csonka, O. A. Vydrov, G. E. Scuseria, L. A. Constantin, X. Zhou, and K. Burke. Restoring the density–gradient expansion for exchange in solids and surfaces. *Phys. Rev. Lett.*, 100:136406, 2008.

[32] V. I. Anisimov, F. Aryasetiawan, and A. Lichtenstein. First–principles calculations of the electronic structure and spectra of strongly correlated systems: the lda+ u method. *Journal of Physics: Condensed Matter*, 9(4):767, 1997.

[33] S. L. Dudarev, G. A. Botton, S. Y. Savrasov, C. J. Humphreys, and A. P. Sutton. Electron–energy–loss spectra and the structural stability of nickel oxide: An lsda+u study. *Phys. Rev. B*, 57:1505–1509, 1998.

[34] J. Heyd, G. E. Scuseria, and M. Ernzerhof. Hybrid functionals based on a screened coulomb potential. *The Journal of Chemical Physics*, 118(18):8207–8215, 2003.

[35] J. Heyd, G. E. Scuseria, and M. Ernzerhof. Erratum:âĂIJhybrid functionals based on a screened coulomb potentialâĂİ[j. chem. phys. 118, 8207 (2003)]. *The Journal of Chemical Physics*, 124(21):219906, 2006.

[36] R. Van Noorden, B. Maher, R. Nuzzo, et al. The top 100 papers. *Nature*, 514(7524):550–553, 2014.

[37] V. L. Chevrier, S. P. Ong, R. Armiento, M. K. Y. Chan, and G. Ceder. Hybrid density functional calculations of redox potentials and formation energies of transition metal compounds. *Phys. Rev. B*, 82:075122, 2010.

[38] G. Hautier, S. P. Ong, A. Jain, C. J. Moore, and G. Ceder. Accuracy of density functional theory in predicting formation energies of ternary oxides from binary oxides and its implication on phase stability. *Phys. Rev. B*, 85:155208, 2012.

[39] M. Cococcioni. Accurate and efficient calculations on strongly correlated minerals with the lda+ u method: review and perspectives. *Reviews in Mineralogy and Geochemistry*, 71(1):147–167, 2010.

[40] J. P. Perdew, A. Ruzsinszky, G. I. Csonka, O. A. Vydrov, G. E. Scuseria, L. A. Constantin, X. Zhou, and K. Burke. Reply to the comment by ann e. mattsson, rickard armiento, and thomas r. mattsson. *Phys. Rev. Lett.*, 101:239702, 2008.

[41] J. Tao, J. P. Perdew, V. N. Staroverov, and G. E. Scuseria. Climbing the density functional ladder: Nonempirical meta–generalized gradient approximation designed for molecules and solids. *Phys. Rev. Lett.*, 91:146401, 2003.

[42] Y. Zhao and D. G. Truhlar. A new local density functional for main–group thermochemistry, transition metal bonding, thermochemical kinetics, and noncovalent interactions. *The Journal of Chemical Physics*, 125(19), 2006.

[43] J. Sun, B. Xiao, and A. Ruzsinszky. Communication: Effect of the orbital–overlap dependence in the meta generalized gradient approximation. *The Journal of Chemical Physics*, 137(5), 2012.

[44] J. M. del Campo, J. L. Gazquez, S. B. Trickey, and A. Vela. A new meta–gga exchange functional based on an improved constraint–based {GGA}. *Chemical Physics Letters*, 543:179 – 183, 2012.

[45] J. Sun, B. Xiao, R. Fang, Y.and Haunschild, P. Hao, A. Ruzsinszky, G. I. Csonka, G. E. Scuseria, and J. P. Perdew. Density functionals that recognize covalent, metallic, and weak bonds. *Phys. Rev. Lett.*, 111:106401, 2013.

[46] J. E. Post. Manganese oxide minerals: Crystal structures and economic and environmental significance. *Proc. Natl. Acad. Sci.*, 96(7):3447–3454, 1999.

[47] S. Fritsch, J. E. Post, and A. Navrotsky. Energetics of low–temperature polymorphs of manganese dioxide and oxyhydroxide. *Geochimica et Cosmochimica Acta*, 61(13):2613 – 2616, 1997.

[48] S. Fritsch, J. E. Post, S. L. Suib, and A. Navrotsky. Thermochemistry of Framework and Layer Manganese Dioxide Related Phases. *Chem. Mater.*, 10(2):474–479, 1998.

[49] L. I. Hill and A. Verbaere. On the structural defects in synthetic γ-mno2s. *J. Solid State Chem.*, 177(12):4706 – 4723, 2004.

[50] J. C. Hunter. Preparation of a new crystal form of manganese dioxide: λ-MnO2. *J. Solid State Chem.*, 39(2):142–147, 1981.

[51] Y. D. Kondrashev and A. I. Zaslavskii. The structure of the modifications of manganese(IV) oxide. *Golden Book of Phase Transitions, Wroclaw*, 1:1–123, 2002.

[52] W. Wei, X. Cui, W. Chen, and D. G. Ivey. Manganese oxide–based materials as electrochemical supercapacitor electrodes. *Chemical Society Reviews*, 40(3):1697–1721, 2011.

[53] D. M. Robinson, Y. B. Go, M. Mui, G. Gardner, Z. Zhang, D. Mastrogiovanni, E. Garfunkel, J. Li, M. Greenblatt, and G. C. Dismukes. Photochemical water oxidation by crystalline polymorphs of manganese oxides: Structural requirements for catalysis. *J. Am. Chem. Soc.*, 135(9):3494–3501, 2013.

[54] B. Ammundsen and J. Paulsen. Novel lithium–ion cathode materials based on layered manganese oxides. *Advanced Materials*, 13(12–13):943–956, 2001.

[55] C. Franchini, R. Podloucky, J. Paier, M. Marsman, and G. Kresse. Ground–state properties of multivalent manganese oxides: Density functional and hybrid density functional calculations. *Phys. Rev. B*, 75:195128, 2007.

[56] D. Balachandran, D. Morgan, G. Ceder, and A. van de Walle. First-principles study of the structure of stoichiometric and Mn-deficient MnO_2 . *J. Solid State Chem.*, 173(2):462 – 475, 2003.

[57] T. X. T. Sayle, C. R. A. Catlow, R. R. Maphanga, P. E. Ngoepe, and D. C. Sayle. Generating mno2 nanoparticles using simulated amorphization and recrystallization. *Journal of the American Chemical Society*, 127(37):12828–12837, 2005.

[58] E. Cockayne and L. Li. First-principles {DFT} + U studies of the atomic, electronic, and magnetic structure of Îś-MnO2 (cryptomelane). *Chem. Phys. Lett.*, 544:53 – 58, 2012.

[59] L. Wang, T. Maxisch, and G. Ceder. Oxidation energies of transition metal oxides within the GGA + U framework. *Phys. Rev. B*, 73:195107, 2006.

[60] Y. Crespo and N. Seriani. Electronic and magnetic properties of α–MnO_2 from *ab initio* calculations. *Phys. Rev. B*, 88:144428, 2013.

[61] D. A. Tompsett, D. S. Middlemiss, and M. S. Islam. Importance of anisotropic Coulomb interactions and exchange to the band gap and antiferromagnetism of β–MnO_2 from DFT+U. *Phys. Rev. B*, 86:205126, 2012.

[62] N. Yamamoto, T. Endo, M. Shimada, and T. Takada. Single crystal growth of α–mno2. *Japanese Journal of Applied Physics*, 13(4):723, 1974.

[63] J. E Greedan, N. P. Raju, A. S. Wills, C. Morin, S. M. Shaw, and J. N. Reimers. Structure and magnetism in λ–mno_2. geometric frustration in a defect spinel. *Chem. Mater.*, 10(10):3058–3067, 1998.

[64] L. W. Guo, D. L. Peng, H. Makino, T. Hanada, S. K. Hong, K. Sumiyama, T. Yao, and K. Inaba. Structural characteristics and magnetic properties of λ–mno2 films grown by plasma–assisted molecular beam epitaxy. *Journal of Applied Physics*, 90(1):351–354, 2001.

[65] H. T. Zhu, J. Luo, H. X. Yang, J. K. Liang, G. H. Rao, J. B. Li, and Z. M. Du. Birnessite–type mno2 nanowalls and their magnetic properties. *J. Phys. Chem. C*, 112(44):17089–17094, 2008.

[66] W. Setyawan and S. Curtarolo. High–throughput electronic band structure calculations: Challenges and tools. *Computational Materials Science*, 49(2):299 – 312, 2010.

[67] S. Curtarolo, W. Setyawan, G. Hart, M. Jahnatek, R. V. Chepulskii, R. H. Taylor, S. Wang, J. Xue, K. Yang, O Levy, M. J. Mehl, H. T. Stokes, D. O. Demchenko, and D. Morgan. Aflow: An automatic framework for high–throughput materials discovery. *Computational Materials Science*, 58:218 – 226, 2012.

[68] A. P. Blaise, Z. Chen, D. N. Abram, and T. F. Jaramillo. Thin films of sodium birnessite–type mno2: Optical properties, electronic band structure, and solar photoelectrochemistry. *The Journal of Physical Chemistry C*, 115(23):11830–11838, 2011.

[69] N. Ohama and Y. Hamaguchi. Determination of the exchange integrals in β–mno2. *Journal of the Physical Society of Japan*, 30(5):1311–1318, 1971.

[70] W. H. Baur. Rutile–type compounds. v. refinement of mno2 and mgf2. *Acta Crystallographica Section B: Structural Crystallography and Crystal Chemistry*, 32(7):2200–2204, 1976.

[71] A. A. Bolzan, C. Fong, B. J. Kennedy, and C. J. Howard. Powder neutron diffraction study of pyrolusite, beta–mno2. *Australian Journal of Chemistry*, 46(6):939–944, 1993.

[72] H. Sato, T. Enoki, M. Isobe, and Y. Ueda. Transport properties and magnetism of a helically hund–coupled conductor: $\beta--mno_2$. *Phys. Rev. B*, 61:3563–3569, 2000.

[73] A. K. M. F. ul Islam, R. Islam, and K. A. Khan. Studies on the thermoelectric effect in semiconducting mno2 thin films. *Journal of Materials Science: Materials in Electronics*, 16(4):203–207, 2005.

[74] R. Druilhe and J. P. Suchet. Electron transport in cro2 and mn(x)cr(1–x)o2. *Czechoslovak Journal of Physics*, 17(4):337–346, 1967.

[75] A. M. Bystrom. The crystal structure of ramsdellite, an orthorhombic modification of mno2. *Acta Chemica Scandinavica*, 3:163–173, 1949.

[76] H. Miura, H. Kudou, J. H. Choi, and Y. Hariya. The crystal structure of ramsdellite from pirika mine. *Journal of the Faculty of Science, Hokkaido University. Series 4, Geology and mineralogy*, 22(4):611–617, 1990.

[77] J. E. Post and P. J. Heaney. Neutron and synchrotron X-ray diffraction study of the structures and dehydration behaviors of ramsdellite and "groutellite". *Am. Mineral.*, 89(7):969–975, 2004.

[78] M. H Rossouw, D. C Liles, M. M. Thackeray, W. I. F David, and S. Hull. Alpha manganese dioxide for lithium batteries: A structural and electrochemical study. *Mater. Res. Bull.*, 27(2):221–230, 1992.

[79] R. Ma, Y. Bando, L. Zhang, and T. Sasaki. Layered mno2 nanobelts: Hydrothermal synthesis and electrochemical measurements. *Advanced Materials*, 16(11):918–922, 2004.

[80] R. Chen, P. Zavalij, and S. M. Whittingham. Hydrothermal synthesis and characterization of kxmno2 yh2o. *Chemistry of Materials*, 8(6):1275–1280, 1996.

[81] J. Sun, J. P. Perdew, and A. Ruzsinszky. Semilocal density functional obeying a strongly tightened bound for exchange. *Proceedings of the National Academy of Sciences*, 112(3):685–689, 2015.

[82] J. P. Perdew and A. Zunger. Self–interaction correction to density–functional approximations for many–electron systems. *Phys. Rev. B*, 23:5048–5079, 1981.

[83] A. Yoshimori. A new type of antiferromagnetic structure in the rutile type crystal. *J. Phys. Soc. Jpn.*, 14(6):807–821, 1959.

[84] H. Sato, K. Wakiya, T. Enoki, T. Kiyama, Y. Wakabayashi, H. Nakao, and Y. Murakami. Magnetic structure of β–mno2: X–ray magnetic scattering study. *Journal of the Physical Society of Japan*, 70(1):37–40, 2001.

[85] M. Regulski, R. Przeniosło, I. Sosnowska, and J.-U. Hoffmann. Incommensurate magnetic structure of $\beta - -\mathrm{mno}_2$. *Phys. Rev. B*, 68:172401, 2003.

[86] D. Morgan, B. Wang, G. Ceder, and A. van de Walle. First–principles study of magnetism in spinel mno_2. *Phys. Rev. B*, 67:134404, 2003.

[87] P. Haas, F. Tran, and P. Blaha. Calculation of the lattice constant of solids with semilocal functionals. *Phys. Rev. B*, 79:085104, 2009.

[88] G. I. Csonka, J. P. Perdew, A. Ruzsinszky, P. H. T. Philipsen, S. Lebegue, J. Paier, O. A. Vydrov, and J. G. Angyan. Assessing the performance of recent density functionals for bulk solids. *Phys. Rev. B*, 79:155107, 2009.

[89] D. A. Kitchaev and G. Ceder. Evaluating structure selection in the hydrothermal growth of FeS2 pyrite and marcasite. *Nat. Commun.*, 7:13799, 2016.

[90] D. A. Kitchaev, S. T. Dacek, W. Sun, and G. Ceder. Thermodynamics of Phase Selection in MnO2 Framework Structures through Alkali Intercalation and Hydration. *Journal of the American Chemical Society*, 139(7):2672–2681, 2017.

[91] G. H. Booth, A. Grüneis, G. Kresse, and A. Alavi. Towards an exact description of electronic wavefunctions in real solids. *Nature*, 493(7432):365–370, 2013.

[92] K. Burke. Perspective on density functional theory. *The Journal of chemical physics*, 136(15):150901, 2012.

[93] A. D. Becke. Perspective: Fifty years of density-functional theory in chemical physics. *The Journal of chemical physics*, 140(18):18A301, 2014.

[94] H. S. Yu, S. L. Li, and D. G. Truhlar. Perspective: Kohn-sham density functional theory descending a staircase. *The Journal of chemical physics*, 145(13):130901, 2016.

[95] R. Sarmiento-Perez, S. Botti, and M. A. L. Marques. Optimized exchange and correlation semilocal functional for the calculation of energies of formation. *Journal of chemical theory and computation*, 11(8):3844–3850, 2015.

[96] S. P. Ong, W. D. Richards, A. Jain, G. Hautier, M. Kocher, S. Cholia, D. Gunter, V. L. Chevrier, K. A. Persson, and G. Ceder. Python Materials Genomics (pymatgen): A robust, open-source python library for materials analysis. *Comp. Mater. Sci.*, 68:314 – 319, 2013.

[97] M. G. Medvedev, I. S. Bushmarinov, J. Sun, J. P. Perdew, and K. A. Lyssenko. Response to comment on âĂIJdensity functional theory is straying from the path toward the exact functionalâĂİ. *Science*, 356(6337):496–496, 2017.

[98] R. A. Robie. Debye temperatures of selected silicate minerals. Technical report, US Geological Survey,, 1988.

[99] O. L. Anderson, E. Schreiber, R. C. Liebermann, and N. Soga. Some elastic constant data on minerals relevant to geophysics. *Reviews of Geophysics*, 6(4):491–524, 1968.

[100] K. J. Bachmann, F. S. L. Hsu, F. A. Thiel, and H. M. Kasper. Debye temperature and standard entropies and enthalpies of compound semiconductors of the type i-iii-vi2. *Journal of Electronic Materials*, 6(4):431–448, 1977.

[101] I. Tanaka. Impacts of first principles calculations in engineering ceramics. *Journal of the Ceramic Society of Japan*, 124(8):791–795, 2016.

[102] X.and Cohen A. J. Li, C.and Zheng, P. Mori-Sánchez, and W. Yang. Local scaling correction for reducing delocalization error in density functional approximations. *Physical review letters*, 114(5):053001, 2015.

[103] Ju. Jaramillo, G. E. Scuseria, and M. Ernzerhof. Local hybrid functionals. *The Journal of chemical physics*, 118(3):1068–1073, 2003.

[104] J. P. Perdew and A. Zunger. Self-interaction correction to density-functional approximations for many-electron systems. *Physical Review B*, 23(10):5048, 1981.

[105] V. Stevanović, S. Lany, X. Zhang, and A. Zunger. Correcting density functional theory for accurate predictions of compound enthalpies of formation: Fitted elemental-phase reference energies. *Physical Review B*, 85(11):115104, 2012.

[106] K. A. Persson, B. Waldwick, P. Lazic, and G. Ceder. Prediction of solid-aqueous equilibria: Scheme to combine first-principles calculations of solids with experimental aqueous states. *Phys. Rev. B*, 85:235438, 2012.

[107] S. P. Ong, V. L. Chevrier, G. Hautier, A. Jain, C. Moore, S. Kim, X. Ma, and G. Ceder. Voltage, stability and diffusion barrier differences between sodium-ion and lithium-ion intercalation materials. *Energy & Environmental Science*, 4(9):3680–3688, 2011.

[108] S. T. Dacek, W. D. Richards, D. A. Kitchaev, and G. Ceder. Structure and dynamics of fluorophosphate na-ion battery cathodes. *Chemistry of Materials*, 28(15):5450–5460, 2016.

[109] A. Rabenau. The role of hydrothermal synthesis in preparative chemistry. *Angewandte Chemie International Edition*, 24(12):1026–1040, 1985.

[110] A. Ennaoui, d S. Fiechter, C. Pettenkofer, N. Alonso-Vante, N. Buker, M. Bronold, C. Hopfner, and H. Tributsch. Iron disulfide for solar energy conversion. *Solar Energy Materials and Solar Cells*, 29(4):289 – 370, 1993.

[111] Z. Hu, Z. Zhu, F. Cheng, K. Zhang, J. Wang, C. Chen, and J. Chen. Pyrite FeS_2 for high-rate and long-life rechargeable sodium batteries. *Energy Environ. Sci.*, 8:1309–1316, 2015.

[112] H. L. Murowchick, J. B.and Barnes. Marcasite precipitation from hydrothermal solutions. *Geochimica et Cosmochimica Acta*, 50(12):2615–2629, 1986.

[113] D. Rickard and G. W. Luther. Chemistry of iron sulfides. *Chemical Reviews*, 107(2):514–62, 2007.

[114] R. Murphy and D. R. Strongin. Surface reactivity of pyrite and related sulfides. *Surface Science Reports*, 64(1):1 – 45, 2009.

[115] M. A. A. Schoonen and H. L. Barnes. Reactions forming pyrite and marcasite from solution: I. Nucleation of FeS_2 below 100 C. *Geochimica et Cosmochimica Acta*, 55(6):1495 – 1504, 1991.

[116] M. Drabek and M. Rieder. Synthesis and structure of single-crystal marcasite. In *Mineral Deposit Research: Meeting the Global Challenge*, pages 111–113. Springer, 2005.

[117] C. Wadia, Y. Wu, S. Gul, S. K. Volkman, J. Guo, and P. Alivisatos. Surfactant-assisted hydrothermal synthesis of single phase pyrite FeS_2 nanocrystals. *Chemistry of Materials*, 21(13):2568–2570, 2009.

[118] F. Gronvold and E. F. Westrum Jr. Heat capacities of iron disulfides: thermodynamics of marcasite from 5 to 700 K, pyrite from 300 to 780 K, and the transformation of marcasite to pyrite. *The Journal of Chemical Thermodynamics*, 8(11):1039 – 1048, 1976.

[119] R. Sun, M. K. Y. Chan, S-Y. Kang, and G. Ceder. Intrinsic stoichiometry and oxygen-induced *p*-type conductivity of pyrite FeS_2. *Phys. Rev. B*, 84:035212, 2011.

[120] A. Krishnamoorthy, F. W. Herbert, S. Yip, K. J. Van Vliet, and B. Yildiz. Electronic states of intrinsic surface and bulk vacancies in FeS_2. *Journal of Physics: Condensed Matter*, 25(4):045004, 2013.

[121] J. M. McHale, A. Auroux, A. J. Perrotta, and A. Navrotsky. Surface energies and thermodynamic phase stability in nanocrystalline aluminas. *Science*, 277(5327):788–791, 1997.

[122] A. Navrotsky. Energetics of nanoparticle oxides: interplay between surface energy and polymorphism. *Geochemical Transactions*, 4(1):1–4, 2003.

[123] D. Fornasiero, V. Eijt, and J. Ralston. An electrokinetic study of pyrite oxidation. *Colloids and Surfaces*, 62(1):63 – 73, 1992.

[124] J. Bebie, M. A. A. Schoonen, M. Fuhrmann, and D. R. Strongin. Surface charge development on transition metal sulfides: An electrokinetic study. *Geochimica et Cosmochimica Acta*, 62(4):633 – 642, 1998.

[125] A. S. Barnard and L. A. Curtiss. Prediction of TiO_2 nanoparticle phase and shape transitions controlled by surface chemistry. *Nano Letters*, 5(7):1261–1266, 2005.

[126] M. S. Schmokel, L. Bjerg, Si. Cenedese, M. R. V. Jorgensen, Y-S. Chen, and B. B. Overgaard, J.and Iversen. Atomic properties and chemical bonding in the pyrite and marcasite polymorphs of fes_2: a combined experimental and theoretical electron density study. *Chem. Sci.*, 5:1408–1421, 2014.

[127] B. C. Han and G. Ceder. Effect of coadsorption and ru alloying on the adsorption of CO on Pt. *Phys. Rev. B*, 74:205418, 2006.

[128] A. J. Bard and L. R. Faulkner. *Electrochemical Methods: Fundamentals and Applications*. Wiley, 2000.

[129] S. Parez, M. Predota, and M. Machesky. Dielectric properties of water at rutile and graphite surfaces: Effect of molecular structure. *The Journal of Physical Chemistry C*, 118(9):4818–4834, 2014.

[130] O. Teschke, G. Ceotto, and E. F. de Souza. Interfacial water dielectric-permittivity-profile measurements using atomic force microscopy. *Phys. Rev. E*, 64:011605, 2001.

[131] R. T. Lowson. Aqueous oxidation of pyrite by molecular oxygen. *Chemical Reviews*, 82(5):461–497, 1982.

[132] A. Hung, J. Muscat, I. Yarovsky, and S. P. Russo. Density-functional theory studies of pyrite FeS_2 (100) and (110) surfaces. *Surface Science*, 513(3):511 – 524, 2002.

[133] A. Hung, J. Muscat, I. Yarovsky, and S. P. Russo. Density-functional theory studies of pyrite FeS_2 (111) and (210) surfaces. *Surface Science*, 520(1-2):111 – 119, 2002.

[134] R. P. Richards, E. L. Clopton, and J. A. Jaszczak. Pyrite and marcasite intergrowths from northern illinois. *Mineralogical Record*, 26(2):129, 1995.

[135] P. E. Blöchl. Projector augmented-wave method. *Phys. Rev. B*, 50:17953–17979, 1994.

[136] R. Sun, M. K. Y. Chan, and G. Ceder. First-principles electronic structure and relative stability of pyrite and marcasite: Implications for photovoltaic performance. *Physical Review B*, 83(23):235311, 2011.

[137] P. W. Tasker. The stability of ionic crystal surfaces. *Journal of Physics C: Solid State Physics*, 12(22):4977, 1979.

[138] K. J. Andersson, H. Ogasawara, D. Nordlund, G. E. Brown, and A. Nilsson. Preparation, structure, and orientation of pyrite fes_2100 surfaces: Anisotropy, sulfur monomers, dimer vacancies, and a possible fes surface phase. *The Journal of Physical Chemistry C*, 118(38):21896–21903, 2014.

[139] Lan Wang, K. Vu, A. Navrotsky, R. Stevens, B. F. Woodfield, and J. Boerio-Goates. Calorimetric study:âĂŁ surface energetics and the magnetic transition in nanocrystalline CoO. *Chemistry of Materials*, 16(25):5394–5400, 2004.

[140] K. Mathew, R. Sundararaman, K. Letchworth-Weaver, T. A. Arias, and R. G. Hennig. Implicit solvation model for density-functional study of nanocrystal surfaces and reaction pathways. *The Journal of Chemical Physics*, 140(8), 2014.

[141] A. Verdaguer, G. M. Sacha, H. Bluhm, and M. Salmeron. Molecular structure of water at interfaces:âĂŁ wetting at the nanometer scale. *Chemical Reviews*, 106(4):1478–1510, 2006.

[142] W. Tan, E. Sanville, and G. Henkelman. A grid-based bader analysis algorithm without lattice bias. *Journal of Physics: Condensed Matter*, 21(8):084204, 2009.

[143] J. B. Murowchick and H. L. Barnes. Effects of temperature and degree of supersaturation on pyrite morphology. *American Mineralogist*, 72(11-12):1241–1250, 1987.

[144] M. Kosmulski. *Surface charging and points of zero charge*, volume 145. CRC Press, 2009.

[145] J. M. Tarascon. The Spinel Phase of $LiMn_2O_4$ as a Cathode in Secondary Lithium Cells. *J. Electrochem. Soc.*, 138(10):2859, 1991.

[146] M. M. Thackeray. Manganese oxides for lithium batteries. *Prog. Solid State Chem.*, 25(1):1 – 71, 1997.

[147] A. Bergmann, I. Zaharieva, H. Dau, and P. Strasser. Electrochemical water splitting by layered and 3d cross-linked manganese oxides: correlating structural motifs and catalytic activity. *Energy Environ. Sci.*, 6:2745–2755, 2013.

[148] M. Huynh, C. Shi, S. J. L. Billinge, and D. G. Nocera. Nature of Activated Manganese Oxide for Oxygen Evolution. *J. Am. Chem. Soc.*, 137(47):14887–904, 2015.

[149] S. L. Suib. Porous manganese oxide octahedral molecular sieves and octahedral layered materials. *Acc. Chem. Res.*, 41(4):479–487, 2008.

[150] W. Wei, X. Cui, W. Chen, and D. G. Ivey. Manganese oxide-based materials as electrochemical supercapacitor electrodes. *Chem. Soc. Rev.*, 40(3):1697–1721, 2011.

[151] D. A. Kitchaev, H. Peng, Y. Liu, J. Sun, J. P. Perdew, and G. Ceder. Energetics of MnO_2 polymorphs in density functional theory. *Phys. Rev. B*, 93:045132, 2016.

[152] C. Delmas, C. Fouassier, and P. Hagenmuller. Structural classification and properties of the layered oxides. *Physica B+C*, 99(1):81 – 85, 1980.

[153] Y. Chabre and J. Pannetier. Structural and electrochemical properties of the proton / γ-mno$_2$ system. *Prog. Solid State Chem.*, 23(1):1 – 130, 1995.

[154] A. Clearfield. Role of ion exchange in solid-state chemistry. *Chem. Rev.*, 88(1):125–148, 1988.

[155] M. M. Thackeray, M. H. Rossouw, R. J. Gummow, D. C. Liles, K. Pearce, A. De Kock, W.I.F. David, and S. Hull. Ramsdellite-MnO_2 for lithium batteries: the ramsdellite to spinel transformation. *Electrochim. Acta*, 38(9):1259 – 1267, 1993.

[156] R. N. DeGuzman, Y-F. Shen, E. J. Neth, S. L. Suib, C. L. O'Young, S. Levine, and J. M. Newsam. Synthesis and Characterization of Octahedral Molecular Sieves (OMS-2) Having the Hollandite Structure. *Chem. Mater.*, 6(6):815–821, 1994.

[157] D. Portehault, S. Cassaignon, E. Baudrin, and J-P. Jolivet. Structural and morphological control of manganese oxide nanoparticles upon soft aqueous precipitation through MnO_4/Mn^{2+} reaction. *J. Mater. Chem.*, 19(16):2407, 2009.

[158] S. Sarciaux, A. Le Gal La Salle, A. Verbaere, Y. Piffard, and D. Guyomard. γ-mno$_2$ for li batteries: Part i. γ-mno$_2$: Relationships between synthesis conditions, material characteristics and performances in lithium batteries. *J. Power Sources*, 81-82:656 – 660, 1999.

[159] D. Lv, X. Huang, H. Yue, and Y. Yang. Sodium-Ion-Assisted Hydrothermal Synthesis of γ-MnO_2 and Its Electrochemical Performance. *J. Electrochem. Soc.*, 156(11):A911–A916, 2009.

[160] X. Ma, H. Chen, and G. Ceder. Electrochemical Properties of Monoclinic NaMnO2. *J. Electrochem. Soc.*, 158(12):A1307–A1312, 2011.

[161] X. Sun, V. Duffort, N. D. Mehdi, B. L.and Browning, and L. F. Nazar. Investigation of the Mechanism of Mg Insertion in Birnessite in Nonaqueous and Aqueous Rechargeable Mg-Ion Batteries. *Chem. Mater.*, 28(2):534–542, 2016.

[162] X-F. Shen, Y-S. Ding, J. C. Hanson, M. Aindow, and S. L. Suib. In situ synthesis of mixed-valent manganese oxide nanocrystals:âĂĽ an in situ synchrotron x-ray diffraction study. *J. Am. Chem. Soc.*, 128(14):4570–4571, 2006.

[163] S. Birgisson, K. M. O. Jensen, T. L. Christiansen, J. F. von Bulow, and B. B. Iversen. In situ powder X-ray diffraction study of the hydro-thermal formation of LiMn2O4 nanocrystallites. *Dalton Trans.*, 43:15075–15084, 2014.

[164] Z-R. Tiana, G. Xia, J. Luo, S. L. Suib, and A. Navrotsky. Effects of water, cations, and structure on energetics of layer and framework phases, na$_x$mg$_y$mno$_2$ nh$_2$o. *J. Phys. Chem. B*, 104(20):5035–5039, 2000.

[165] J. Reed, G. Ceder, and A. Van Der Ven. Layered-to-Spinel Phase Transition in Li_xMnO_2. *Electrochem. Solid-State Lett.*, 4(6):A78–A81, 2001.

[166] Z-G. Wei, J-H. Yan, Y. Wu, and Y. Liu. Importance of Metal Cations and Water for Stability of MnO2 Crystals. *Chin. J. Chem. Phys.*, 28(6):711–715, 2015.

[167] D. A. Tompsett and M. S. Islam. Electrochemistry of hollandite α-mno_2: Li-ion and na-ion insertion and li_2o incorporation. *Chem. Mater.*, 25(12):2515–2526, 2013.

[168] D. Wang, L-M. Liu, S-J. Zhao, B-H. Li, H. Liu, and X-F. Lang. β-MnO2 as a cathode material for lithium ion batteries from first principles calculations. *Phys. Chem. Chem. Phys.*, 15(23):9075–83, 2013.

[169] C. Ling, R. Zhang, T. S. Arthur, and F. Mizuno. How General is the Conversion Reaction in Mg Battery Cathode: A Case Study of the Magnesiation of α-MnO2. *Chem. Mater.*, 27(16):5799–5807, 2015.

[170] J. J. De Yoreo, P. U. P. A. Gilbert, N. A. J. M. Sommerdijk, R. L. Penn, S. Whitelam, D. Joester, H. Zhang, J. D. Rimer, A. Navrotsky, J. F. Banfield, A. F. Wallace, F. M. Michel, F. C. Meldrum, H. Colfen, and P. M. Dove. Crystallization by particle attachment in synthetic, biogenic, and geologic environments. *Science*, 349(6247):aaa6760, 2015.

[171] X. Li, X. Ma, D. Su, L. Liu, R. Chisnell, S. P. Ong, H. Chen, A. Toumar, J-C. Idrobo, Y. Lei, J. Bai, F. Wang, J. W. Lynn, Y. S. Lee, and G. Ceder. Direct visualization of the Jahn–Teller effect coupled to Na ordering in Na5/8MnO2. *Nat. Mater.*, 13(6):586–592, 2014.

[172] A. Togo and I. Tanaka. First principles phonon calculations in materials science. *Scr. Mater.*, 108:1–5, Nov 2015.

[173] M. Pourbaix. *Atlas of electrochemical equilibria in aqueous solutions*. National Association of Corrosion Engineers; Houston, Texas, 1974.

[174] N. Birkner and A. Navrotsky. Thermodynamics of manganese oxides: Effects of particle size and hydration on oxidation-reduction equilibria among hausmannite, bixbyite, and pyrolusite. *Am. Mineral.*, 97(8-9):1291–1298, 2012.

[175] Z. Zeng, M. K. Y. Chan, Z-Z. Zhao, J. Kubal, D. Fan, and J. Greeley. Towards first principles-based prediction of highly accurate electrochemical pourbaix diagrams. *J. Phys. Chem. C*, 119(32):18177–18187, 2015.

[176] P. Ruetschi. Cation-Vacancy Model for MnO2. *J. Electrochem. Soc.*, 131(12):2737–2744, 1984.

[177] P. Ruetschi and R. Giovanoli. Cation Vacancies in MnO2 and Their Influence on Electrochemical Reactivity. *J. Electrochem. Soc.*, 135(11):2663–2669, 1988.

[178] J. J. Coleman. Dry Cell Dynamics: The Bobbin. *Trans. Electrochem. Soc.*, 90(1):545–583, 1946.

[179] S. W. Donne, F. H. Feddrix, R. Glockner, S. Marion, and T. Norby. Water and protons in electrodeposited MnO2 (EMD). *Solid State Ionics*, 152-153:695–701, 2002.

[180] P. L. Sharma and S. M. Whittingham. The role of tetraethyl ammonium hydroxide on the phase determination and electrical properties of γ-mnooh synthesized by hydrothermal. *Mater. Lett.*, 48(6):319 – 323, 2001.

[181] J. D. Hem. *Chemical equilibria and rates of manganese oxidation.* Geological Survey Water Supply Paper 1667-A, United States Government Printing Office, Washington, 1963.

[182] X. Huang, D. Lv, H. Yue, A. Attia, and Y. Yang. Controllable synthesis of α and β MnO_2: cationic effect on hydrothermal crystallization. *Nanotechnology*, 19(22):225606, 2008.

[183] X. Duan, J. Yang, H. Gao, J. Ma, L. Jiao, and W. Zheng. Controllable hydrothermal synthesis of manganese dioxide nanostructures: shape evolution, growth mechanism and electrochemical properties. *CrystEngComm*, 14:4196–4204, 2012.

[184] B. Yin, S. Zhang, He Jiang, F. Qu, and X. Wu. Phase-controlled synthesis of polymorphic MnO_2 structures for electrochemical energy storage. *J. Mater. Chem. A*, 3:5722–5729, 2015.

[185] Y-I. Jang, B. Huang, H. Wang, D. R. Sadoway, and Y-M. Chiang. Electrochemical Cycling-Induced Spinel Formation in High-Charge Capacity Orthorhombic LiMnO2. *J. Electrochem. Soc.*, 146(9):3217–3223, 1999.

[186] Y. Idemoto, T. Mochizuki, K. Ui, and N. Koura. Properties, Crystal Structure, and Performance of o-LiMnO2 as Cathode Material for Li Secondary Batteries. *J. Electrochem. Soc.*, 153(2):A418–A424, 2006.

[187] T. Kohler, T. Armbruster, and E. Libowitzky. Hydrogen bonding and jahn-teller distortion in groutite, α-mnooh, and manganite, γ-mnooh, and their relations to the manganese dioxides ramsdellite and pyrolusite. *J. Solid State Chem.*, 133(2):486 – 500, 1997.

[188] G. Mattioli, I. Zaharieva, H. Dau, and L. Guidoni. Atomistic texture of amorphous manganese oxides for electrochemical water splitting revealed by ab initio calculations combined with x-ray spectroscopy. *J. Am. Chem. Soc.*, 137(32):10254–10267, 2015.

[189] S. G. Gautam, P. Canepa, W. D. Richards, R. Malik, and G. Ceder. Role of structural h_2o in intercalation electrodes: The case of mg in nanocrystalline xerogel-v_2o_5. *Nano Lett.*, 16(4):2426–2431, 2016.

[190] D. C. Golden, C-C. Chen, and J. B. Dixon. Synthesis of Todorokite. *Science*, 231(4739):717–719, 1986.

[191] Q. Feng, T. Horiuchi, L. Liu, K. Yanagisawa, and T. Mitsushio. Hydrothermal Soft Chemical Synthesis of Tunnel Manganese Oxides with Na^+ as Template. *Chem. Lett.*, 29(3):284–285, 2000.

[192] G. G. Xia, W. Tong, E. N. Tolentino, N-G. Duan, S. L. Brock, J-Y. Wang, S. L. Suib, and T. Ressler. Synthesis and Characterization of Nanofibrous Sodium Manganese Oxide with a 2x4 Tunnel Structure. *Chem. Mater.*, 13(5):1585–1592, 2001.

[193] X.-F. Shen, Y.-S. Ding, J. Liu, J. Cai, K. Laubernds, R.âĂĽP. Zerger, A. Vasiliev, M. Aindow, and S.âĂĽL. Suib. Control of nanometer-scale tunnel sizes of porous manganese oxide octahedral molecular sieve nanomaterials. *Advanced Materials*, 17(7):805–809, 2005.

[194] J. Luo, Q. Zhang, A. Huang, O. Giraldo, and S. L. Suib. Double-aging method for preparation of stabilized naâĹŠbuserite and transformations to todorokites incorporated with various metals. *Inorg. Chem.*, 38(26):6106–6113, 1999.

[195] M. Wiechen, I. Zaharieva, H. Dau, and P. Kurz. Layered manganese oxides for water-oxidation: alkaline earth cations influence catalytic activity in a photosystem ii-like fashion. *Chem. Sci.*, 3:2330–2339, 2012.

[196] C. J. Clarke, G. J. Browning, and S. W. Donne. An rde and rrde study into the electrodeposition of manganese dioxide. *Electrochim. Acta*, 51(26):5773 – 5784, 2006.

[197] X. Hu, D. A. Kitchaev, L. Wu, Q. Meng, B. Zhang, A. Marschilok, E. S Takeuchi, G. Ceder, and Y. Zhu. Revealing rich polytypism in todorokite MnO2. *in preparation*, 2017.

[198] J. E. Post, P. J. Heaney, and J. Hanson. Synchrotron x-ray diffraction study of the structure and dehydration behavior of todorokite. *American Mineralogist*, 88(1):142–150, 2003.

[199] P. Selvarasu, D. A. Kitchaev, J. Mangum, L. T. Schelhas, J. Perkins, K. Shun-Gilmour, B. Gorman, M. Toney, G. Ceder, D. Ginley, and L. Garten. Phase selection in the aqueous growth of Mn3+ oxides. *in preparation*, 2017.

[200] B-R. Chen, W. Sun, D. A. Kitchaev, J. S. Mangum, V. Thampy, L. M. Garten, D. G. Ginley, B. P. Gorman, K. H. Stone, G. Ceder, M. F. Toney, and L. T. Schelhas. Understanding crystallization pathways leading to manganese oxide polymorph formation. *in preparation*, 2017.

[201] J. D. Hem and C. J. Lind. Nonequilibrium models for predicting forms of precipitated manganese oxides. *Geochimica et Cosmochimica Acta*, 47(11):2037–2046, 1983.

[202] O. Kubaschewski, C. B. Alcock, and P. J. Spencer. *Materials thermochemistry*. Pergamon press, 1993.

[203] M. Huynh, D.K. Bediako, and D. G. Nocera. A functionally stable manganese oxide oxygen evolution catalyst in acid. *Journal of the American Chemical Society*, 136(16):6002–6010, 2014.

[204] D. G. Nocera. On the future of global energy. *Daedalus*, 135(4):112–115, 2006.

[205] S. Chu and A. Majumdar. Opportunities and challenges for a sustainable energy future. *nature*, 488(7411):294–303, 2012.

[206] T. R. Cook, D. K. Dogutan, S. Y. Reece, Y. Surendranath, T. S. Teets, and D. G. Nocera. Solar energy supply and storage for the legacy and nonlegacy worlds. *Chemical reviews*, 110(11):6474–6502, 2010.

[207] N. S. Lewis and D. G. Nocera. Powering the planet: Chemical challenges in solar energy utilization. *Proceedings of the National Academy of Sciences*, 103(43):15729–15735, 2006.

[208] S. Hammes-Schiffer. Theory of proton-coupled electron transfer in energy conversion processes. *Accounts of chemical research*, 42(12):1881–1889, 2009.

[209] Y. Surendranath and D. G. Nocera. Oxygen evolution reaction chemistry of oxide-based electrodes. *Progress in Inorganic Chemistry, Volume 57*, pages 505–560, 2011.

[210] M. W. Kanan and D. G. Nocera. In situ formation of an oxygen-evolving catalyst in neutral water containing phosphate and co2+. *Science*, 321(5892):1072–1075, 2008.

[211] Y. Surendranath, M. Dinca, and D. G. Nocera. Electrolyte-dependent electrosynthesis and activity of cobalt-based water oxidation catalysts. *Journal of the American Chemical Society*, 131(7):2615–2620, 2009.

[212] Y. Surendranath, M. W. Kanan, and D. G. Nocera. Mechanistic studies of the oxygen evolution reaction by a cobalt-phosphate catalyst at neutral ph. *Journal of the American Chemical Society*, 132(46):16501–16509, 2010.

[213] J. B. Gerken, J. G. McAlpin, J. Y. C. Chen, W. H. Rigsby, M. L.and Casey, R. D. Britt, and S. S. Stahl. Electrochemical water oxidation with cobalt-based electrocatalysts from ph 0–14: the thermodynamic basis for catalyst structure, stability, and activity. *Journal of the American Chemical Society*, 133(36):14431–14442, 2011.

[214] K. Klingan, F. Ringleb, I. Zaharieva, J. Heidkamp, P. Chernev, D. Gonzalez-Flores, M. Risch, A. Fischer, and H. Dau. Water oxidation by amorphous cobalt-based oxides: volume activity and proton transfer to electrolyte bases. *ChemSusChem*, 7(5):1301–1310, 2014.

[215] D. A. Corrigan. The catalysis of the oxygen evolution reaction by iron impurities in thin film nickel oxide electrodes. *Journal of the Electrochemical Society*, 134(2):377–384, 1987.

[216] M. Dincă, Y. Surendranath, and D. G. Nocera. Nickel-borate oxygen-evolving catalyst that functions under benign conditions. *Proceedings of the National Academy of Sciences*, 107(23):10337–10341, 2010.

[217] D. K. Bediako, Y. Surendranath, and D. G. Nocera. Mechanistic studies of the oxygen evolution reaction mediated by a nickel–borate thin film electrocatalyst. *Journal of the American Chemical Society*, 135(9):3662–3674, 2013.

[218] L. Trotochaud, S. L. Young, J. K. Ranney, and S. W. Boettcher. Nickel–iron oxyhydroxide oxygen-evolution electrocatalysts: the role of intentional and incidental iron incorporation. *Journal of the American Chemical Society*, 136(18):6744–6753, 2014.

[219] M. GoÌĹrlin, J. Ferreira de Araujo, H. Schmies, D. Bernsmeier, S. Dresp, M. Gliech, Z. Jusys, P. Chernev, R. Kraehnert, and H. Dau. Tracking catalyst redox states and reaction dynamics in ni–fe oxyhydroxide oxygen evolution reaction electrocatalysts: The role of catalyst support and electrolyte ph. *Journal of the American Chemical Society*, 139(5):2070–2082, 2017.

[220] M. Huynh, D. K. Bediako, Y. Liu, and D. G. Nocera. Nucleation and growth mechanisms of an electrodeposited manganese oxide oxygen evolution catalyst. *The Journal of Physical Chemistry C*, 118(30):17142–17152, 2014.

[221] D. Kang, T. W. Kim, S. R. Kubota, A. C. Cardiel, H. Gil. Cha, and K-S. Choi. Electrochemical synthesis of photoelectrodes and catalysts for use in solar water splitting. *Chemical reviews*, 115(23):12839–12887, 2015.

[222] I. Roger and M. D. Symes. First row transition metal catalysts for solar-driven water oxidation produced by electrodeposition. *Journal of Materials Chemistry A*, 4(18):6724–6741, 2016.

[223] C. Costentin, D. G. Nocera, and C. N. Brodsky. Multielectron, multisubstrate molecular catalysis of electrochemical reactions: Formal kinetic analysis in the total catalysis regime. *Proceedings of the National Academy of Sciences*, page 201711129, 2017.

[224] L. G. Bloor, P. I. Molina, M. D. Symes, and L. Cronin. Low ph electrolytic water splitting using earth-abundant metastable catalysts that self-assemble in situ. *J. Am. Chem. Soc*, 136(8):3304–3311, 2014.

[225] R. Frydendal, E. A. Paoli, I. Chorkendorff, J. Rossmeisl, and I. E. L. Stephens. Toward an active and stable catalyst for oxygen evolution in acidic media: Ti-stabilized mno2. *Advanced Energy Materials*, 5(22), 2015.

[226] R. J. R. Jones, A. Shinde, D. Guevarra, C. Xiang, J. A. Haber, J. Jin, and J. M. Gregoire. Parallel electrochemical treatment system and application for identifying acid-stable oxygen evolution electrocatalysts. *ACS combinatorial science*, 17(2):71–75, 2015.

[227] Y. Meng, W. Song, H. Huang, Z. Ren, S-Y. Chen, and S. L. Suib. Structure–property relationship of bifunctional mno2 nanostructures: highly efficient, ultra-stable electrochemical water oxidation and oxygen reduction reaction catalysts identified in alkaline media. *Journal of the American Chemical Society*, 136(32):11452–11464, 2014.

[228] M. Morita, C. Iwakura, and H. Tamura. The anodic characteristics of massive manganese oxide electrode. *Electrochimica Acta*, 24(4):357–362, 1979.

[229] M. M. Najafpour, K. C. Leonard, F-R. Fan, M. A. Tabrizi, A. J. Bard, Cecil K. King'ondu, B. Suib, S. L .and Haghighi, and S. I. Allakhverdiev. Nano-size layered manganese–calcium oxide as an efficient and biomimetic catalyst for water oxidation under acidic conditions: comparable to platinum. *Dalton Transactions*, 42(14):5085–5091, 2013.

[230] T. Takashima, K. Hashimoto, and R. Nakamura. Inhibition of charge disproportionation of mno2 electrocatalysts for efficient water oxidation under neutral conditions. *Journal of the American Chemical Society*, 134(44):18153–18156, 2012.

[231] I. Zaharieva, P. Chernev, M. Risch, K. Klingan, M. Kohlhoff, A. Fischer, and H. Dau. Electrosynthesis, functional, and structural characterization of a water-oxidizing manganese oxide. *Energy & Environmental Science*, 5(5):7081–7089, 2012.

[232] Y. Gorlin, B. Lassalle-Kaiser, J. D. Benck, S. Gul, S. M. Webb, V. K. Yachandra, J. Yano, and T. F. Jaramillo. In situ x-ray absorption spectroscopy investigation of a bifunctional manganese oxide catalyst with high activity for electrochemical water oxidation and oxygen reduction. *Journal of the American Chemical Society*, 135(23):8525–8534, 2013.

[233] M. S. Hybertsen and S. G. Louie. Electron correlation in semiconductors and insulators: Band gaps and quasiparticle energies. *Phys. Rev. B*, 34:5390–5413, Oct 1986.

[234] D-H. Seo, A. Urban, and G. Ceder. Calibrating transition-metal energy levels and oxygen bands in first-principles calculations: Accurate prediction of redox potentials and charge transfer in lithium transition-metal oxides. *Phys. Rev. B*, 92:115118, Sep 2015.

[235] S. Lany. Band-structure calculations for the $3d$ transition metal oxides in gw. *Phys. Rev. B*, 87:085112, Feb 2013.

[236] H. Xu, S. Xu, H. Wang, and H. Yan. Characterization of hausmannite mn3o4 thin films by chemical bath deposition. *Journal of The Electrochemical Society*, 152(12):C803–C807, 2005.

[237] D.P. Dubal, D.S. Dhawale, R.R. Salunkhe, S.M. Pawar, V.J. Fulari, and C.D. Lokhande. A novel chemical synthesis of interlocked cubes of hausmannite mn3o4 thin films for supercapacitor application. *Journal of Alloys and Compounds*, 484(1-2):218 – 221, 2009.

[238] N. M. Hosny and A. Dahshan. Facile synthesis and optical band gap calculation of mn3o4 nanoparticles. *Materials Chemistry and Physics*, 137(2):637 – 643, 2012.

[239] C. Persson, Y-J. Zhao, S. Lany, and A. Zunger. n-type doping of cuinse2 and cugase2. *Phys. Rev. B*, 72:035211, Jul 2005.

[240] H. Raebiger, S. Lany, and A. Zunger. Charge self-regulation upon changing the oxidation state of transition metals in insulators. *Nature*, 453(7196):763–766, 2008.

[241] G. B. Jensen and O. V. Nielsen. The magnetic structure of mn 3 o 4 hausmannite between 4.7k and neel point, 41k. *Journal of Physics C: Solid State Physics*, 7(2):409, 1974.

[242] Z. M. Chan, D. A. Kitchaev, J. Nelson Weker, C. Schnedermann, K. Lim, G. Ceder, W. Tumas, M. F. Toney, and D. G. Nocera. Electrochemical Trapping of Metastable Mn3+ Ions for Activation of MnO2 Oxygen Evolution Catalysts. *in preparation*, 2017.

[243] M. M. Najafpour, M. A. Tabrizi, B. Haghighi, and Govindjee. A manganese oxide with phenol groups as a promising structural model for water oxidizing complex in photosystem ii: a âĂŸgolden fishâĂŹ. *Dalton Transactions*, 41(14):3906–3910, 2012.

[244] A. Indra, P. W. Menezes, I. Zaharieva, E. Baktash, J. Pfrommer, M. Schwarze, H. Dau, and M. Driess. Active mixed-valent mnox water oxidation catalysts through partial oxidation (corrosion) of nanostructured mno particles. *Angewandte Chemie International Edition*, 52(50):13206–13210, 2013.

[245] A. S. Ryabova, F. S. Napolskiy, T. Poux, S. Y. Istomin, A. Bonnefont, D. M. Antipin, A. Y. Baranchikov, E. E. Levin, A. M. Abakumov, G. Kerangueven, E. V. Antipov, G. A. Tsirlina, and E. R. Savinova. Rationalizing the influence of the mn(iv)/mn(iii) red-ox transition on the electrocatalytic activity of manganese oxides in the oxygen reduction reaction. *Electrochimica Acta*, 187:161 – 172, 2016.

[246] K. Jin, H. Seo, T. Hayashi, M. Balamurugan, D. Jeong, Y. K. Go, J. S. Hong, K. H. Cho, H. Kakizaki, N. Bonnet-Mercier, et al. Mechanistic investigation of

water oxidation catalyzed by uniform, assembled mno nanoparticles. *Journal of the American Chemical Society*, 139(6):2277–2285, 2017.

[247] T. Takashima, K. Hashimoto, and R. Nakamura. Mechanisms of ph-dependent activity for water oxidation to molecular oxygen by mno2 electrocatalysts. *Journal of the American Chemical Society*, 134(3):1519–1527, 2012.

[248] H. Seo, K. H. Cho, H. Ha, S. Park, J. S. Hong, K. Jin, and K. T. Nam. Water oxidation mechanism for 3d transition metal oxide catalysts under neutral condition. *J. Korean Ceram. Soc*, 54(1):1–8, 2017.

[249] S. Kim, S. Lee, K. W. Nam, J. Shin, S. Y. Lim, W. Cho, K. Suzuki, Y. Oshima, M. Hirayama, R. Kanno, and J. W. Choi. On the mechanism of crystal water insertion during anomalous spinel-to-birnessite phase transition. *Chemistry of Materials*, 28(15):5488–5494, 2016.

[250] X. Yang and M-H. Baik. cis, cis-[(bpy) 2ruvo] 2o4+ catalyzes water oxidation formally via in situ generation of radicaloid ruiv-oâĂć. *Journal of the American Chemical Society*, 128(23):7476–7485, 2006.

[251] A. Grimaud, O. Diaz-Morales, B. Han, W. T. Hong, Y-L. Lee, L. Giordano, K. A. Stoerzinger, M. T. M. Koper, and Y. Shao-Horn. Activating lattice oxygen redox reactions in metal oxides to catalyse oxygen evolution. *Nature Chemistry*, 9(5):457–465, 2017.

[252] L-P. Wang and T. Van Voorhis. Direct-coupling o2 bond forming a pathway in cobalt oxide water oxidation catalysts. *The Journal of Physical Chemistry Letters*, 2(17):2200–2204, 2011.

[253] Y. Jiang, F. Li, B. Zhang, X. Li, X. Wang, F. Huang, and L. Sun. Promoting the activity of catalysts for the oxidation of water with bridged dinuclear ruthenium complexes. *Angewandte Chemie International Edition*, 52(12):3398–3401, 2013.

[254] M. Zhang, M. De Respinis, and H. Frei. Time-resolved observations of water oxidation intermediates on a cobalt oxide nanoparticle catalyst. *Nature chemistry*, 6(4):362–367, 2014.

[255] M. H. V. Huynh and T. J. Meyer. Proton-coupled electron transfer. *Chemical Reviews*, 107(11):5004–5064, 2007.

[256] C. N. Brodsky, R. G. Hadt, D. Hayes, N. Reinhart, B. J.and Li, L. X. Chen, and D. G. Nocera. In situ characterization of cofacial co (iv) centers in co4o4 cubane: Modeling the high-valent active site in oxygen-evolving catalysts. *Proceedings of the National Academy of Sciences*, 114(15):3855–3860, 2017.

[257] M. Sathiya, G. Rousse, K. Ramesha, C.P. Laisa, H. Vezin, M. T. Sougrati, M.-L. Doublet, D. Foix, D. Gonbeau, W. Walker, A. Prakash, M. Ben Hassine, L. Dupont, and J. M. Tarascon. Reversible anionic redox chemistry in high-capacity layered-oxide electrodes. *Nature materials*, 12(9):827–835, 2013.

[258] M. Saubanere, E. McCalla, J.-M. Tarascon, and M.-L. Doublet. The intriguing question of anionic redox in high-energy density cathodes for li-ion batteries. *Energy Environ. Sci.*, 9:984–991, 2016.

[259] D-H. Seo, J. Lee, A. Urban, R. Malik, S-Y. Kang, and G. Ceder. The structural and chemical origin of the oxygen redox activity in layered and cation-disordered li-excess cathode materials. *Nature chemistry*, 8(7):692–697, 2016.

[260] N. Li, D. K. Bediako, R. G. Hadt, D. Hayes, T. J. Kempa, F. von Cube, D. C. Bell, L. X. Chen, and D. G. Nocera. Influence of iron doping on tetravalent nickel content in catalytic oxygen evolving films. *Proceedings of the National Academy of Sciences*, 114(7):1486–1491, 2017.

[261] J. Lee, D-H. Seo, M. Balasubramanian, N. Twu, X. Li, and G. Ceder. A new class of high capacity cation-disordered oxides for rechargeable lithium batteries: Li–Ni–Ti–Mo oxides. *Energy & Environmental Science*, 8(11):3255–3265, 2015.

[262] K. Luo, M. R. Roberts, R. Hao, N. Guerrini, D. M. Pickup, Y-S. Liu, K. Edström, J. Guo, A. V. Chadwick, L. C. Duda, et al. Charge-compensation in 3d-transition-metal-oxide intercalation cathodes through the generation of localized electron holes on oxygen. *Nature chemistry*, 8(7):684–691, 2016.

[263] J. Lee, D. A. Kitchaev, D-H. Kwon, C. Lee, J. K. Papp, Y-S. Liu, T. Shi, Z. Lun, B. D. McCloskey, J. Guo, M. Balasubramanian, and G. Ceder. Reversible Mn2+/Mn4+ double redox in high capacity Li-excess cathode materials. *submitted*, 2017.

[264] B. Krebs, A. Schiemann, and M. Lage. Synthese und kristallstruktur einer neuen hexagonalen modifikation von al2s3 mit funffach koordiniertem aluminium. *Zeitschrift fur anorganische und allgemeine Chemie*, 619(6):983–988, 1993.

[265] G. A. Steigmann and J. Goodyear. The crystal structure of al2se3. *Acta Crystallographica*, 20(5):617–619, 1966.

[266] J. C. Phillips. Ionicity of the chemical bond in crystals. *Rev. Mod. Phys.*, 42:317–356, Jul 1970.

[267] A. Le Bail, C. Jacoboni, M. Leblanc, R. De Pape, H. Duroy, and J. L. Fourquet. Crystal structure of the metastable form of aluminum trifluoride b-alf3 and the gallium and indium homologs. *Journal of Solid State Chemistry*, 77(1):96 – 101, 1988.

[268] H. Vollstadt, E. Ito, M. Akaishi, S. Akimoto, and O Fukunaga. High pressure synthesis of rocksalt type of aln. *Proceedings of the Japan Academy, Series B*, 66(1):7–9, 1990.

[269] M. A. Tuktabiev, S. V. Popova, V. V. Brazhkin, A. G. Lyapin, and Y. Katayama. Compressibility and polymorphism of a - as4s4 realgar under high pressure. *Journal of Physics: Condensed Matter*, 21(38):385401, 2009.

[270] E. B. Brackett, T. E. Brackett, and R. L. Sass. The crystal structures of barium chloride, barium bromide, and barium iodide. *The Journal of Physical Chemistry*, 67(10):2132–2135, 1963.

[271] H. E. Swanson, E. Tatge, and R. K. Fuyat. *Standard X-ray diffraction powder patterns*. US Government Printing Office, 1953.

[272] R. D. Hazen and L. W. Finger. HighâĂŘpressure and high-temperature crystal chemistry of beryllium oxide. *Journal of Applied Physics*, 59(11):3728–3733, 1986.

[273] O. Madelung. *II-VI compounds*, pages 173–244. Springer Berlin Heidelberg, Berlin, Heidelberg, 2004.

[274] W. Wong-Ng and R. S. Roth. Single-crystal structural investigation of bao2. *Physica C: Superconductivity*, 233(1):97 – 101, 1994.

[275] T. A. Grzybowski and A. L. Ruoff. High-pressure phase transition in base. *Phys. Rev. B*, 27:6502–6503, May 1983.

[276] H. Okamoto. The ba-se (barium-selenium) system. *Journal of Phase Equilibria*, 12(4):467–469, 1991.

[277] T. A. Grzybowski and A. L. Ruoff. Band-overlap metallization of bate. *Phys. Rev. Lett.*, 53:489–492, Jul 1984.

[278] P. Ghalsasi and P. S. Ghalsasi. Single crystal x-ray structure of bef2: a-quartz. *Inorganic Chemistry*, 50(1):86–89, 2011.

[279] H. A. Harwig and A. G. Gerards. The polymorphism of bismuth sesquioxide. *Thermochimica Acta*, 28(1):121 – 131, 1979.

[280] S. Nakajima. The crystal structure of bi2te3âĹŠxsex. *Journal of Physics and Chemistry of Solids*, 24(3):479 – 485, 1963.

[281] S. C. Nyburg, G. A. Ozin, and S. T. Szymański. The crystal and molecular structure of bismuth trichloride. *Acta Crystallographica Section B*, 27(12):2298–2304, Dec 1971.

[282] M. M. Stasova. Crystal structure of bismuth selenides and bismuth and antimony tellurides. *Journal of Structural Chemistry*, 8(4):584–589, 1967.

[283] K. Yamana, K. Kihara, and T. Matsumoto. Bismuth tellurides: BiTe and Bi_4Te_3. *Acta Crystallographica Section B*, 35(1):147–149, Jan 1979.

[284] O. Reckeweg and F. J. DiSalvo. About binary and ternary alkaline earth metal nitrides. *Zeitschrift fur anorganische und allgemeine Chemie*, 627(3):371–377, 2001.

[285] P. Hohn, S. Hoffmann, J. Hunger, S. Leoni, F. Nitsche, W. Schnelle, and R. Kniep. β-ca3n2, a metastable nitride in the system ca-n. *Chemistry - A European Journal*, 15(14):3419–3425, 2009.

[286] J. Hao, Y. W. Li, J. S. Wang, C. L. Ma, L. Y. Huang, R. Liu, Q. L. Cui, G. T. Zou, J. Liu, and X. D. Li. Experimental determinations of the high-pressure crystal structures of ca3n2. *The Journal of Physical Chemistry C*, 114(39):16750–16755, 2010.

[287] C. J. Howard, B. J. Kennedy, and C. Curfs. Temperature-induced structural changes in $\mathrm{cacl}_2, \mathrm{cabr}_2$, and crcl_2: A synchrotron x-ray powder diffraction study. *Phys. Rev. B*, 72:214114, Dec 2005.

[288] D. K. Smith and H. R. Leider. Low-temperature thermal expansion of LiH, MgO and CaO. *Journal of Applied Crystallography*, 1(4):246–249, Nov 1968.

[289] F. Zhang, J. D. Gale, B. P. Uberuaga, C. R. Stanek, and N. A. Marks. Importance of dispersion in density functional calculations of cesium chloride and its related halides. *Phys. Rev. B*, 88:054112, Aug 2013.

[290] S. Yoshioka, H. Hayashi, A. Kuwabara, F. Oba, K. Matsunaga, and I. Tanaka. Structures and energetics of ga 2 o 3 polymorphs. *Journal of Physics: Condensed Matter*, 19(34):346211, 2007.

[291] C. Y. Jones, J. C. Bryan, K. Kirschbaum, and J. G. Edwards. Refinement of the crystal structure of digallium trisulfide, ga2s3. *Zeitschrift für Kristallographie-New Crystal Structures*, 216(1-4):349–350, 2001.

[292] A. Kuhn, A. Chevy, and R. Chevalier. Crystal structure and interatomic distances in gase. *physica status solidi (a)*, 31(2):469–475, 1975.

[293] N. C. Fernelius. Properties of gallium selenide single crystal. *Progress in Crystal Growth and Characterization of Materials*, 28(4):275 – 353, 1994.

[294] O. N. Carlson. The ge-n (germanium-nitrogen) system. *Bulletin of Alloy Phase Diagrams*, 11(6):567–568, 1990.

[295] E. Soignard, P. F. McMillan, C. Hejny, and K. Leinenweber. Pressure-induced transformations in a- and b-ge3n4: in situ studies by synchrotron x-ray diffraction. *Journal of Solid State Chemistry*, 177(1):299 – 311, 2004.

[296] K. Leinenweber, M. O'keeffe, M. Somayazulu, H. Hubert, P. F. McMillan, and G. H. Wolf. Synthesis and structure refinement of the spinel, ge3n4. *Chemistry - A European Journal*, 5:3076–3078, 1999.

[297] M. Micoulaut, L. Cormier, and G. S. Henderson. The structure of amorphous, crystalline and liquid geo 2. *Journal of Physics: Condensed Matter*, 18(45):R753, 2006.

[298] H. Wiedemeier and P. A. Siemers. The thermal expansion and high temperature transformation of gese. *Zeitschrift fur anorganische und allgemeine Chemie*, 411(1):90–96, 1975.

[299] A. Grzechnik, S. Stolen, E. Bakken, T. Grande, and M. Mezouar. Structural transformations in three-dimensional crystalline gese2 at high pressures and high temperatures. *Journal of Solid State Chemistry*, 150(1):121 – 127, 2000.

[300] J. Goldak, C. S. Barrett, D. Innes, and W. Youdelis. Structure of alpha gete. *The Journal of Chemical Physics*, 44(9):3323–3325, 1966.

[301] N. S. NRampersadha, A. M. Ventera, and D. G. Billing. Rietveld refinement of in2s3 using neutron and x-ray powder diffraction data. *Physica B: Condensed Matter*, 350:e383–e385, 2004.

[302] H. Inuzuka and S Sugaike. On in2te3 its preparation and lattice constant. *Proceedings of the Japan Academy*, 30:383–386, 1954.

[303] M. D. Banus, R. E. Hanneman, M. Stroncin, and K. Gooen. High-pressure transitions in a(iii)b(vi) compounds: Indium telluride. *Science*, 142(3593):662–663, 1963.

[304] T. Chattopadhyay, R. P. Santandrea, and H. G. von Schnering. A new high pressure phase of inte. *Physica B+C*, 139:353 – 355, 1986.

[305] A. Vegas, A. Grzechnik, M. Hanfland, C. Muhle, and M. Jansen. Antifluorite to ni2in-type phase transition in {K2S} at high pressures. *Solid State Sciences*, 4(8):1077 – 1081, 2002.

[306] T. W. D. Farley, W. Hayes, S. Hull, M. T. Hutchings, and M. Vrtis. Investigation of thermally induced li + ion disorder in li 2 o using neutron diffraction. *Journal of Physics: Condensed Matter*, 3(26):4761, 1991.

[307] H. Foppl. Die kristallstrukturen der alkaliperoxyde. *Z. Anorg. Allg. Chem.*, 291:12–50, 1957.

[308] W. Buehrer, F. Altorfer, J. Mesot, H. Bill, P. Carron, and H.G. Smith. Lattice dynamics and the diffuse phase transition of lithium sulphide investigated by coherent neutron scattering. *Journal of Physics: Condensed Matter 3*, 3:1055–1064, 1991.

[309] G. Brauer and E. Zintl. Constitution of phosphides, arsenides, antimonides, and bismuthides of li, na and k. *Z. Physical Chemistry B*, 37:323–352, 1937.

[310] R. A. Weppner, W.and Huggins. Electrochemical investigation of the chemical diffusion, partial ionic conductivities, and other kinetic parameters in li3sb and li3bi. *Journal of Solid State Chemistry*, 22(3):297 – 308, 1977.

[311] A. Huq, J. W. Richardson, E. R. Maxey, D. Chandra, and W-M. Chien. Structural studies of li3n using neutron powder diffraction. *Journal of Alloys and Compounds*, 436(1-2):256 – 260, 2007.

[312] Y. Liebold-Ribeiro, D. Fischer, and M. Jansen. Experimental substantiation of the âĂIJenergy landscape conceptâĂİ for solids: Synthesis of a new modification of libr. *Angewandte Chemie*, 120(23):4500–4503, 2008.

[313] D. Fischer, M. Jansen, Ž.P. Čančarević, and J.C. Schön. *Theoretical and Experimental Exploration of the Energy Landscape of LiI*, volume 494 of *Materials Science Forum*, pages 61–66. Trans Tech Publications, 5 2005.

[314] W. Baden, P.C. Schmidt, and A Weiss. The intermetallic system licd(1-x)tl(x). *Phys. Stat. Sol.*, 51, 1979.

[315] J. Dorrepaal. Revised crystal data for magnesium dichloride, mgcl2. *Journal of Applied Crystallography*, 17, 1984.

[316] V. W. H. Baur. Uber die verfeinerung der kristallstrukturbestimmung einiger vertreter des rutiltyps: Tio2, sno2, geo2, und mgf2. *Acta. Crysta.*, 9, 1956.

[317] C. Bocchi, A. Catellani, F. Germini, L. Nasi, J. K. Morrod, K. A. Prior, and G. Calestani. Metastable zinc-blende mgs structure: Combined experimental and theoretical study. *Phys. Rev. B*, 79:235310, Jun 2009.

[318] B. Bertheville, D. Low, H. Bill, and F. Kubel. Ionic conductivity of na2s single crystals between 295 and 1350 k experimental setup and first results. *Journal of Physics and Chemistry of Solids*, 58(10):1569 – 1577, 1997.

[319] K-J. Range, R Ehrl, and P Hafner. Na3as revisited ii. space group confirmation and structure refinement at 150, 210 and 240 k. *Journal of Alloys and Compounds*, 240(1):19 – 24, 1996.

[320] M. E. Leonova, I. K. Bdikin, S. A. Kulinich, O. K. Gulish, L. G. Sevast'yanova, and K. P. Burdina. High-pressure phase transition of hexagonal alkali pnictides. *Inorganic Materials*, 39(3):266–270, 2003.

[321] Y. Dong and F. J. DiSalvo. Reinvestigation of Na_3P based on single-crystal data. *Acta Crystallographica Section E*, 61(11):i223–i224, Nov 2005.

[322] G. F. Carter and D. H. Templeton. Polymorphism of sodium superoxide. *Journal of the American Chemical Society*, 75(21):5247–5249, 1953.

[323] H. Georg, V. Schnering, and W. HÃűnle. Zur chemie und strukturchemie der phosphide und polyphosphide. 20. darstellung, struktur und eigenschaften der alkalimetallmonophosphide nap und kp. *Zeitschrift fur anorganische und allgemeine Chemie*, 456(1):194–206, 1979.

[324] H Foppl, E Busmann, and F-K Frorath. Die kristallstrukturen von α-na2s2 und k2s2, β-na2s2 und na2se2. *Zeitschrift für anorganische und allgemeine Chemie*, 314(1-2):12–20, 1962.

[325] E Zintl and W Dullenkopf. Über den gitterbau von natl und seine beziehung zu den structuren vom typus des β-messings. *Z. Phys. Chem*, pages 195–205, 1932.

[326] D. Stachel, I. Svoboda, and H. Fuess. Phosphorus Pentoxide at 233 K. *Acta Crystallographica Section C*, 51(6):1049–1050, Jun 1995.

[327] W. J. Moore and L. Pauling. The crystal structures of the tetragonal monoxides of lead, tin, palladium, and platinum. *Journal of the American Chemical Society*, 63(5):1392–1394, 1941.

[328] P.W. Bridgman. The compression of 46 substances to 50,000 kg/cm. *Proceedings of the American Academy of Arts and Sciences*, 74, 1940.

[329] D. Santamaria-Perez, A. Vegas, C. Muehle, and M. Jansen. High-pressure experimental study on Rb_2S: antifluorite to Ni_2In-type phase transitions. *Acta Crystallographica Section B*, 67(2):109–115, Apr 2011.

[330] M. Jansen. Kristallstruktur von sb2o5. *Angewandte Chemie*, 90(2):141–142, 1978.

[331] P. Bayliss and W. Nowacki. Refinement of the crystal structure of stibnite, sb2s3. *Zeitschrift für Kristallographie-Crystalline Materials*, 135(1-6):308–315, 1972.

[332] J. Zhao, H. Liu, L. Ehm, Z. Chen, S. Sinogeikin, Y. Zhao, and G. Gu. Pressure-induced disordered substitution alloy in sb2te3. *Inorganic chemistry*, 50(22):11291–11293, 2011.

[333] J. Amador, E. Gutierrez Puebla, M. A. Monge, I. Rasines, and C. Ruiz Valero. Diantimony tetraoxides revisited. *Inorganic Chemistry*, 27(8):1367–1370, 1988.

[334] D. Orosel, P. Balog, H. Liu, J. Qian, and M. Jansen. Sb2o4 at high pressures and high temperatures. *Journal of Solid State Chemistry*, 178(9):2602 – 2607, 2005.

[335] J. D. McCullough. The crystal structure of selenium dioxide. *Journal of the American Chemical Society*, 59(5):789–794, 1937.

[336] F. C. Mijlhoff. The crystal structure of tetragonal selenium trioxide. *Acta Crystallographica*, 18(4):795–798, Apr 1965.

[337] P. Krishna and R. C. Marshall. The structure, perfection and annealing behaviour of sic needles grown by a vls mechanism. *Journal of Crystal Growth*, 9:319 – 325, 1971.

[338] R. W. Olesinski and G. J. Abbaschian. The câĹŠsi (carbon-silicon) system. *Bulletin of Alloy Phase Diagrams*, 5(5):486–489, 1984.

[339] P. Richet, Y. Bottinga, L. Denielou, J. P. Petitet, and C. Tequi. Thermodynamic properties of quartz, cristobalite and amorphous sio2: drop calorimetry measurements between 1000 and 1800 k and a review from 0 to 2000 k. *Geochimica et Cosmochimica Acta*, 46(12):2639 – 2658, 1982.

[340] J. M. Leger, J. Haines, and A. Atouf. The high pressure behaviour of the cotunnite and post-cotunnite phases of pbcl2 and sncl2. *Journal of Physics and Chemistry of Solids*, 57(1):7 – 16, 1996.

[341] G. Denes, J. Pannetier, and J. Lucas. About snf2 stannous fluoride. ii. crystal structure of Îš- and Îş-snf2. *Journal of Solid State Chemistry*, 33(1):1 – 11, 1980.

[342] J. Haines and J. M. Léger. X-ray diffraction study of the phase transitions and structural evolution of tin dioxide at high pressure:ffrelationships between structure types and implications for other rutile-type dioxides. *Phys. Rev. B*, 55:11144–11154, May 1997.

[343] T. Chattopadhyay, J. Pannetier, and H. G. Von Schnering. Neutron diffraction study of the structural phase transition in sns and snse. *Journal of Physics and Chemistry of Solids*, 47(9):879 – 885, 1986.

[344] B. Pałosz and E. Salje. Lattice parameters and spontaneous strain in AX_2 polytypes: CdI_2, PbI_2 SnS_2 and $SnSe_2$. *Journal of Applied Crystallography*, 22(6):622–623, Dec 1989.

[345] I. V. Dubrovin, L. D. Budennaya, I. B. Mizetskaya, and E. V. Sharkina. Phase diagram of the snte-cdse section of the ternary reciprocal system snte+ cdse (reversible reaction) snse+ cdte. *Inorg. Mater.(Engl. Transl.);(United States)*, 22(4), 1986.

[346] R. L. Sass, T. Brackett, and E. Brackett. The crystal structure of strontium bromide. *The Journal of Physical Chemistry*, 67(12):2862–2863, 1963.

[347] S. A. Hodorowicz and H. A. Eick. An x-ray diffraction study of the srbrxi2âĹŠx system. *Journal of Solid State Chemistry*, 46(3):313 – 320, 1983.

[348] J. B. Forsyth, C. C. Wilson, and T. M. Sabine. A time-of-flight neutron diffraction study of anharmonic thermal vibrations in srf2, at the spallation neutron source isis. *Acta Crystallographica Section A: Foundations of Crystallography*, 45(3):244–247, 1989.

[349] K-J. Range, F. Rau, U. SchieÃ§l, and U. Klement. Verfeinerung der kristallstruktur von sro2. *Zeitschrift fur anorganische und allgemeine Chemie*, 620(5):879–881, 1994.

[350] G. J. Carron. The crystal structure and powder data for arsenic telluride. *Acta Crystallographica*, 16(5):338–343, 1963.

[351] T. G. Worlton and R. A. Beyerlein. Structure and order parameters in the pressure-induced continuous transition in teo_2. *Phys. Rev. B*, 12:1899–1907, Sep 1975.

[352] M. Dusek and J. Loub. X-ray powder diffraction data and structure refinement of teo3. *Powder Diffraction*, 3(3):175–176, 1988.

[353] S. Kastbjerg, N. Bindzus, M. SÃÿndergaard, S. Johnsen, N. Lock, M. Christensen, M. Takata, M. A. Spackman, and B. B. Iversen. Direct evidence of cation disorder in thermoelectric lead chalcogenides pbte and pbs. *Advanced Functional Materials*, 23(44):5477–5483, 2013.

[354] C. W. F. T. Pistorius and J. B. Clark. Effect of pressure on the polymorphism and melting points of the thallous halides. *Phys. Rev.*, 173:692–699, Sep 1968.

[355] P. Berastegui and S. Hull. The crystal structures of thallium(i) fluoride. *Journal of Solid State Chemistry*, 150(2):266 – 275, 2000.

[356] The phase transition of tlte: Crystal structure. *Journal of Solid State Chemistry*, 149(1):123 – 132, 2000.

[357] S. Hull and D. A. Keen. High-pressure polymorphism of the copper(i) halides: A neutron-diffraction study to ∼10 gpa. *Phys. Rev. B*, 50:5868–5885, Sep 1994.

[358] N. E. Brese, M. O'Keeffe, B. L. Ramakrishna, and R. B. Von Dreele. Low-temperature structures of cuo and ago and their relationships to those of mgo and pdo. *Journal of Solid State Chemistry*, 89(1):184 – 190, 1990.

[359] W. R. Cook. The cds-mns and cdse-mnse phase diagrams. *Journal of the American Ceramic Society*, 51(9):518–520, 1968.

[360] C. Yeh, Z. W. Lu, S. Froyen, and A. Zunger. Zinc-blende–wurtzite polytypism in semiconductors. *Phys. Rev. B*, 46:10086–10097, Oct 1992.

[361] V. A. Fedorov, V. A. Ganshin, and Y. N. Korkishko. Determination of the point of the zincblende to wurtzite structural phase transition in cadmium selenide crystals. *physica status solidi (a)*, 126(1):K5–K7, 1991.

[362] R. D. Heyding and L. D. Calvert. Arsenides of transition metals: The arsenides of iron and cobalt. *Canadian Journal of Chemistry*, 35(5):449–457, 1957.

[363] A. S. Risbud, L. P. Snedeker, M. M. Elcombe, A. K. Cheetham, and R. Seshadri. Wurtzite coo. *Chemistry of Materials*, 17(4):834–838, 2005.

[364] M. E. Fleet. Phase equilibria at high temperatures. *Reviews in Mineralogy and Geochemistry*, 61(1):365–419, 2006.

[365] K. L. Komarek and K. Wessely. Übergangsmetall-chalkogensysteme, 1. mitt.: Das system kobalt-selen. *Monatshefte für Chemie / Chemical Monthly*, 103(3):896–906, 1972.

[366] H. Boller and A. Kallel. First order crystallographic and magnetic phase transition in cras. *Solid State Communications*, 9(19):1699 – 1706, 1971.

[367] M. Nasr-Eddine and E. F. Bertaut. Etude de la transition de premier ordre dans crn. *Solid State Communications*, 9(10):717 – 723, 1971.

[368] F. Jellinek. The structures of the chromium sulphides. *Acta Crystallographica*, 10(10):620–628, 1957.

[369] K. Yamamoto and S. Kashida. X-ray study of the average structures of cu2se and cu1.8s in the room temperature and the high temperature phases. *Journal of Solid State Chemistry*, 93(1):202 – 211, 1991.

[370] J. G. Zhao, S. J. You, L. X. Yang, and C. Q. Jin. Structural phase transition of cu 3 n under high pressure. *Solid State Communications*, 150(33):1521–1524, 2010.

[371] W. Buhrer and W. Halg. Crystal structure of high-temperature cuprous iodide and cuprous bromide. *Electrochimica Acta*, 22(7):701 – 704, 1977.

[372] D. A. Keen and S. Hull. The high-temperature structural behaviour of copper(i) iodide. *Journal of Physics: Condensed Matter*, 7(29):5793, 1995.

[373] H. T. Evans and J. A. Konnert. Crystal structure refinement of covellite. *Am. Mineral*, 61(9-10):996–1000, 1976.

[374] S. Stolen, H. Fjellvag, F. Gronvold, J. T. Sipowska, and E. F. Westrum. Heat capacity, structural and thermodynamic properties of synthetic klockmannite cuse at temperatures from 5 k to 652.7 k. enthalpy of decomposition. *The Journal of Chemical Thermodynamics*, 28(7):753 – 766, 1996.

[375] F. Pertlik. Vulcanite, cute: hydrothermal synthesis and crystal structure refinement. *Mineralogy and Petrology*, 71(3):149–154, 2001.

[376] R. S. Kumar, Y. Zhang, S. Sinogeikin, Y. Xiao, S. Kumar, P. Chow, A. L. Cornelius, and C. Chen. Crystal and electronic structure of fese at high pressure and low temperature. *The Journal of Physical Chemistry B*, 114(39):12597–12606, 2010.

[377] Y. Kawasaki, K. Deguchi, S. Demura, T. Watanabe, H. Okazaki, T. Ozaki, T. Yamaguchi, H. Takeya, and Y. Takano. Phase diagram and oxygen annealing effect of fete 1- x se x iron-based superconductor. *Solid State Communications*, 152(13):1135–1138, 2012.

[378] J. C. Fitzmaurice, A. Hector, and I. P. Parkin. Rapid synthesis of tin, hfn and zrn from solid-state precursors. *Polyhedron*, 12(11):1295–1300, 1993.

[379] K. Aurivillius. The crystal structure of mercury (ii) oxide studied by x-ray and neutron diffraction methods. *Acta Chem. Scand.*, 10:852–866, 1956.

[380] T. Ohmiya. Thermal expansion and the phase transformation in mercury sulphide. *Journal of Applied Crystallography*, 7(3):396–397, 1974.

[381] R. A. Young and W. T. Ziegler. Crystal structure of lanthanum nitride1,2. *Journal of the American Chemical Society*, 74(21):5251–5253, 1952.

[382] J. C. Fitzmaurice, A. Hector, A. T. Rowley, and I. P. Parkin. Rapid, low energy synthesis of lanthanide nitrides. *Polyhedron*, 13(2):235 – 240, 1994.

[383] I. A. Smirnov, A. V. Golubkov, V. M. Sergeeva, V. M. Buttaev, T. B. Zhukova, L. D. Finkelstein, and N. N. Efremova. Variation of tm valence in tm1âĹŠxlaxs. *Journal of Magnetism and Magnetic Materials*, 47:485 – 486, 1985.

[384] A. Zieba, K. Seite, A. Kjekshus, and A. F. Andresen. Phase transitions in mnas. *Acta Chem. Scand. A*, 32(2), 1978.

[385] K. Suzuki, T. Kaneko, H. Yoshida, Y. Obi, H. Fujimori, and H. Morita. Crystal structure and magnetic properties of the compound mnn. *Journal of Alloys and Compounds*, 306(1-2):66 – 71, 2000.

[386] S. Furuseth and A. Kjekshus. On the properties of a-mns and mns2. *Acta Chem. Scand*, 19(6), 1965.

[387] A. J. Jacobson and B. Fender. Covalency parameters in mnse and mnse2. *The Journal of Chemical Physics*, 52(9):4563–4566, 1970.

[388] W. D. Johnston and D. E. Sestrich. The mnte-gete phase diagram. *Journal of Inorganic and Nuclear Chemistry*, 19(3-4):229–236, 1961.

[389] N. Schönberg. Some features of the nb-n and nb-no systems. *Acta Chem. Scand*, 8(2), 1954.

[390] G. Brauer and R. Esselborn. Nitridphasen des niobs. *Zeitschrift fur anorganische und allgemeine Chemie*, 309(3-4):151–170, 1961.

[391] G. Oya and Y. Onodera. Phase transformations in nearly stoichiometric nbnx. *Journal of Applied Physics*, 47(7):2833–2840, 1976.

[392] V. N. Zhitomirsky, I. Grimberg, L. Rapoport, N. A. Travitzky, R. L. Boxman, S. Goldsmith, A. Raihel, I. Lapsker, and B. Z. Weiss. Structure and mechanical properties of vacuum arc-deposited nbn coatings. *Thin Solid Films*, 326(1-2):134 – 142, 1998.

[393] J. G. Thompson, A. D. Rae, R. L. Withers, T. R. Welberry, and A. C. Willis. The crystal structure of nickel arsenide. *Journal of Physics C: Solid State Physics*, 21(22):4007, 1988.

[394] F. Gronvold. X-ray and magnetic study of nickel selenides in the range nise to nise2. *Acta Chem. Scand.*, 10(9):1440–1454, 1956.

[395] J. Barstad. Onvthe tellurides of nickel. *Acta Chem. Scand.*, 20(10):2865–2879, 1966.

[396] R. Berger. Crystallographic data on new arsenides and antimonides of titanium and scandium. *Acta Chem. Sound. A*, 31(6), 1977.

[397] W. Nowacki. Die kristallstruktur von scf3. *Zeitschrift für Kristallographie-Crystalline Materials*, 101(1-6):273–283, 1939.

[398] C. P. Kempter, N. H. Krikorian, and J. C. McGuire. The crystal structure of yttrium nitride. *The Journal of Physical Chemistry*, 61(9):1237–1238, 1957.

[399] E. Parthé. Note on the structure of scp and yp. *Acta Crystallographica*, 16(1):71–71, 1963.

[400] H. Hayashi, I. Shirotani, K. Hirano, N. Ishimatsu, O. Shimomura, and T. Kikegawa. Structural phase transition of scsb and {YSb} with a nacl-type structure at high pressures. *Solid State Communications*, 125(10):543 – 546, 2003.

[401] J. J. Murray, J. B. Taylor, L. D. Calvert, Y. Wang, E. J. Gabe, and J. G. Despault. Phase relationships and thermodynamics of refractory metal pnictides: The metal-rich tantalum arsenides. *Journal of the Less Common Metals*, 46(2):311 – 320, 1976.

[402] N. Terao. Structure of tantalum nitrides. *Japanese Journal of Applied Physics*, 10(2):248, 1971.

[403] A. N. Christensen and B. Lebech. A reinvestigation of the structure of ϵ-tantalum nitride. *Acta Crystallographica Section B*, 34(1):261–263, Jan 1978.

[404] F. J. Morin. Oxides which show a metal-to-insulator transition at the neel temperature. *Phys. Rev. Lett.*, 3:34–36, Jul 1959.

[405] S. Andersson, B. Collén, U. Kuylenstierna, and A. Magnéli. Phase analysis studies on the titanium-oxygen system. *Acta Chem. Scand.*, 11(10):1641–1652, 1957.

[406] H. Hahn and B. Harder. Zur kristallstruktur der titansulfide. *Zeitschrift fur anorganische und allgemeine Chemie*, 288(5-6):241–256, 1957.

[407] F. K. McTaggart and A. D. Wadsley. The sulphides, selenides, and tellurides of titanium, zirconium, hafnium, and thorium. i. preparation and characterization. *Australian Journal of Chemistry*, 11(4):445–457, 1958.

[408] R. R Chianelli, J. C. Scanlon, and A. H. Thompson. Structure refinement of stoichiometric tis2. *Materials Research Bulletin*, 10(12):1379 – 1382, 1975.

[409] H. Nowotny and J. Pesl. Untersuchungen im system titan—antimon. *Monatshefte für Chemie und verwandte Teile anderer Wissenschaften*, 82(2):336–343, 1951.

[410] S. Kari. Structural and magnetic properties of vp and vas. *Acta Chem. Scand.*, 26(10):4057–4062, 1972.

[411] F. I. Ajami and R. K. MacCrone. Magnetic susceptibility and superconductivity of cubic vanadium nitrides. *Journal of Physics and Chemistry of Solids*, 36(1):7 – 15, 1975.

[412] J. Stringer. The vanadium-oxygen system - a review. *Journal of the Less Common Metals*, 8(1):1 – 14, 1965.

[413] B. Grison and P. A. Beck. The crystal structure of VSb. *Acta Crystallographica*, 15(8):807–808, Aug 1962.

[414] L. H. Brixner. Structure and electrical properties of some new rare earth arsenides, antimonides and tellurides. *Journal of Inorganic and Nuclear Chemistry*, 15(1-2):199–201, 1960.